FRACTAL INTERFACES FOR STIMULATING AND RECORDING NEURAL IMPLANTS

by

WILLIAM JAMES WATTERSON

A DISSERTATION

Presented to the Department of Physics
and the Graduate School of the University of Oregon
in partial fulfillment of the requirements
for the degree of
Doctor of Philosophy

December 2017

DISSERTATION APPROVAL PAGE

Student: William James Watterson

Title: Fractal Interfaces for Stimulating and Recording Neural Implants

This dissertation has been accepted and approved in partial fulfillment of the requirements for the Doctor of Philosophy degree in the Department of Physics by:

Dr. Benjamín Alemán	Chair
Dr. Richard Taylor	Advisor
Dr. John Toner	Core Member
Dr. Darren Johnson	Core Member
Dr. Cris Niell	Institutional Representative

and

Sara D. Hodges	Interim Vice Provost and Dean of the Graduate School

Original approval signatures are on file with the University of Oregon Graduate School.

Degree awarded December 2017

DISSERTATION ABSTRACT

William James Watterson

Doctor of Philosophy

Department of Physics

December 2017

Title: Fractal Interfaces for Stimulating and Recording Neural Implants

From investigating movement in an insect to deciphering cognition in a human brain to treating Parkinson's disease, hearing loss, or even blindness, electronic implants are an essential tool for understanding the brain and treating neural diseases. Currently, the stimulating and recording resolution of these implants remains low. For instance, they can record all the neuron activity associated with movement in an insect, but are quite far from recording, at an individual neuron resolution, the large volumes of brain tissue associated with cognition. Likewise, there is remarkable success in the cochlear implant restoring hearing due to the relatively simple anatomy of the auditory nerves, but are failing to restore vision to the blind due to poor signal fidelity and transmission in stimulating the more complex anatomy of the visual nerves. The critically important research needed to improve the resolution of these implants is to optimize the neuron-electrode interface. This thesis explores geometrical and material modifications to both stimulating and recording electrodes which can improve the neuron-electrode interface. First, we introduce a fractal electrode geometry which radically improves the restored visual acuity achieved by retinal implants and leads to safe, long-term operation of the

implant. Next, we demonstrate excellent neuron survival and neurite outgrowth on carbon nanotube electrodes, thus providing a safe biomaterial which forms a strong connection between the electrode and neurons. Additional preliminary evidence suggests carbon nanotubes patterned into a fractal geometry will provide further benefits in improving the electrode-neuron interface. Finally, we propose a novel implant based off field effect transistor technology which utilizes an interconnecting fractal network of semiconducting carbon nanotubes to record from thousands of neurons simutaneously at an individual neuron resolution. Taken together, these improvements have the potential to radically improve our understanding of the brain and our ability to restore function to patients of neural diseases.

This dissertation includes previously published and unpublished co-authored material.

CURRICULUM VITAE

NAME OF AUTHOR: William James Watterson

GRADUATE AND UNDERGRADUATE SCHOOLS ATTENDED:

University of Oregon, Eugene

Purdue University, West Lafayette

DEGREES AWARDED:

Doctor of Philosophy, Physics, 2017, University of Oregon

Bachelor of Science, Physics and Mathematics, 2011, Purdue University

PROFESSIONAL EXPERIENCE:

Graduate Research Assistant, University of Oregon, 2013-2017

Graduate Teaching Assistant, University of Oregon, 2011-2013

GRANTS, AWARDS AND HONORS:

Techology Entrepreneurship Program Award, University of Oregon, 2015

Pufendorf Institute of Advanced Studies Fellowship, Pufendorf Institutet, 2014

Materials Science Institute Incoming Student Award, University of Oregon, 2011

Kenneth S. and Paula D. Krane Physics Scholarship, Purdue University, 2010

Gianni Ascarelli Student Award, Purdue University, 2008

PUBLICATIONS:

Watterson, W.J., et al. "Improved visual acuity using photodiode implants featuring fractal electrodes." (2017) In publication.

Watterson, W.J., et al. "Biocompatibility of vertically aligned carbon nanotubes with retinal neurons." (2017) In publication.

Watterson, W.J., et al. "Fractal Electrodes as a Generic Interface for Stimulating Neurons." *Scientific Reports* 7.1 (2017):6717

Watterson, W. J., et al. "Fractal Electronics as a Generic Interface to Neurons." The Fractal Geometry of the Brain. Springer. 2016.

de Lagemaat, J. "Effect of fractal silver electrodes on charge collection and light distribution in semiconducting organic polymer films." *Journal of Materials Chemistry A*, 2.39 (2014): 16608-16616.

ACKNOWLEDGEMENTS

First and foremost, I would like to thank my parents, Amy and Eric Watterson, my brother, Kevin, and my sisters, Erin and Jennifer. Your support and guidance over the many years has helped me to navigate the world. I wouldn't be here today without you and I love and respect you all more than I could ever say.

I'd like to thank my advisor, Richard Taylor, who has helped me to grow as a scientist. Like all PhD students, I was given a project which had not been answered yet, had no definitive path to obtaining the answer, and required at least a bit of fortitude to reach the end. You provided the framework and assistance to me for defining our research, creating solutions, obtaining help when needed from outside physics, and presenting our results. I'd also like to thank Maithe Perez, who helped me become an interdisciplinary scientist. Your patience and rigor truly helped get the ball rolling on my ability to understand biology and neuroscience. I'd also like to thank each of my committee members, Benjamín Alemán, John Toner, Darren Johnson, and Cris Niell. You have all helped develop the ideas laid out in this thesis and have taught me quite a lot across a variety of disciplines.

I'd like to thank my labmates and friends. Rick Montgomery and Ian Pilgrim, my mentors when I joined the lab. You guys helped teach me, brainstormed with me, and helped me solved problems. There may have been some jokes and laughing along the way too. Saba Moslehi and Julian Smith, for the last few years we have shared an office and worked closely on developing an implant. Part of my excitement in our project is truly working collaboratively with you two. I'd also like to thank the newer lab members, Kara Zappitelli and Conor Rowland. You both are incredibly enthusiastic and I'm super excited to see where the project ends up because of your

bright ideas and dedication. I'd also really like to thank my non-lab member friends, Richard Wagner, Tyler Harvey, Andrea Goering, Chris Newby, George De Coster, Carly Wright, Jared Koessler, Andrew Jonelis, and David La Mantia. You all help me grow as a person and I really enjoy the time we spend hiking, playing games, watching TV, playing sports, eating lunch, or just drinking a beer.

Finally, I'd like to thank Robyn Steuber. You teach me about the world, inspire me in my interests, and help me when I'm stressed. I love you and am excited to explore the world with you and live the life of our dreams.

TABLE OF CONTENTS

Chapter Page

I. INTRODUCTION 1

Retinal Implants 3
Neural Stimulation 11
Glia 21
Retina 23
Electrochemistry for Extracellular Neuronal Stimulation 26
Stimulation of Tissue 43
Neuron Adhesion and Cell Cultures 46
Interfacing Neurons with Carbon Nanotubes 59
Carbon Nanotube Electrodes 66
Fractals 72

II. FRACTAL ELECTRODES FOR SUBRETINAL IMPLANTS 75

Voltage Controlled Subretinal Implant Electrodes 76
Photovoltaic Subretinal Implants 98
Tissue Heating from Subretinal Implant Electrodes 123

Chapter Page

III. BIOCOMPATIBILITY OF CARBON NANOTUBES FOR RETINAL IMPLANT ELECTRODES 127

Retinal Cell Cultures on Unfunctionalized Vertically Aligned Carbon Nanotubes 128

Retinal Cell Cultures on Functionalized Vertically Aligned Carbon Nanotubes 142

Retinal Cultures on Carbon Nanotube Rows and Fractals 147

IV. BIOPHILIC FRACTAL SENSORS FOR THE SIMULTANEOUS MEASUREMENT OF MULTIPLE NEURONAL SIGNALS 153

Multi-Terminal In Vivo Transistor Sensors 153

Carbon Nanotube Multi-Terminal Transistor 160

V. CONCLUSIONS 163

REFERENCES CITED 166

LIST OF FIGURES

Figure Page

1. Fundamental architecture underlying retinal implants. 4

2. Cell membrane. 12

3. Passive cell membrane circuit model. 14

4. Cable model for axons and dendrites. 15

5. Action potential. 16

6. Hodgkin-Huxley equivalent circuit. 17

7. Action potential propogation 18

8. Sequence of events outlining extracellular neuron stimulation. 20

9. The retina. 24

10. Debye screening for a biased electrode in an electrolyte. 27

11. Faradaic reaction at an electrode surface in an electrolyte. 31

12. Electrochemical cell equivalent circuit model 33

13. Simple model for electric field in an electrolytic capacitor. 35

14. Poisson-Nernst-Planck solution to electric field in an electrolytic capacitor. 36

15. Equivalent circuit for an electrolytic capacitor with no Faradaic reactions. 37

16. Spherical current source in an electrolyte. 38

17. Cylcic voltammetry applied waveform. 40

18. Cyclic voltammogram. 41

19. Determination of charge injection limit. 42

Figure Page

20. Electrochemical cell impedance plot. 43

21. Protein adsorption at an interface. 48

22. Protein covalent conjugation at an interface. 50

23. Neurite outgrowth on micro-contact printed patterns. 51

24. Neurites turn to grow perpendicular to narrow shallow grooves. 53

25. Axons prefer topographical over chemical surface cues. 57

26. Quasi-flat CNT mats and vertically aligned CNT forests 59

27. Model for growth cone on carbon nanotubes. 64

28. Mathematical and natural branching fractals. 72

29. H-tree fractal electrodes. 73

30. The subretinal implant design. 77

31. Example circuit used to illustrate modified nodal analysis algorithm. . . 79

32. Electrode and neuron equivalent circuits. 81

33. Square, grid, and fractal extracellular voltages under equivalent bias. . . 85

34. Square, grid, and fractal impedance versus frequency 86

35. Square, grid, and fractal extracellular E-fields under equivalent bias. . . 88

36. Varying fractal electrode height. 89

37. Neuron depolarization magnitudes above square and fractal electrodes. . . 90

38. Membrane potential changes during one voltage cycle. 91

39. Neuron depolarizations versus electrode geometry. 92

40. Threshold electrode voltages. 93

41. Electrical crosstalk for subretinal electrodes. 95

42. Photodiode implant equivalent circuit models. 105

43. Load impedance for square and fractal electrodes. 109

Figure Page

44. IV curves and voltage-intensity curves for square and fractal electrodes. 110

45. Extracellular voltages due to 10 mW/mm^2 incident irradiation. 112

46. Membrane depolarizations due to 10 mW/mm^2 incident irradiation. . . . 114

47. Threshold voltages and irradiances required for stimulation. 115

48. Extracellular voltages at 250 Hz. 116

49. Threshold irradiations for varying dark current densities. 121

50. Equivalent circuit model for tissue heating. 123

51. Temperature increases during one stimulation pulse. 126

52. Temperature increase versus applied voltage. 126

53. VACNT forests and pillars. 136

54. Wetting contact angles of VACNT forests. 136

55. XPS VACNT forests. 137

56. Neurons and glia on VACNT forests. 138

57. Neurite lengths on two different VACNT preparations. 139

58. XPS plasma functionalized VACNT forests. 143

59. XPS peak deconvolution of VACNT forests. 144

60. Neurons and glia on functionalized VACNT forests. 145

61. Neurite length box plot between four different VACNT preparations. . . 146

62. Fractal VACNT electrode. 148

63. Neurons and glia on VACNT row geometries. 149

64. Neurons on fractal VACNT electrode. 150

65. Neurites can extend from VACNT top surface to silicon oxide substrate. 151

66. Glia on VACNT fractal H-tree 151

Figure Page

67. Novel transistor probes for in vivo neural recordings. 157

68. Multi-terminal transistor example neuron localization. 158

69. Sensor calibration library. 159

70. Validation testing of CNT transistor sensor. 162

LIST OF TABLES

Table Page

1. Charge injection limits and double layer capacitances of different electrode materials. 45

2. Summary of in vitro experiments investigating neuron growth on CNT films. 69

3. Summary of in vitro experiments investigating neuron growth on VACNTs. 70

4. Summary of CNT electrodes interfacing with neural tissue. 71

5. List of model parameters and their associated values. 104

CHAPTER I

INTRODUCTION

Cyborg, someone who is part human and part machine, may seem like science fiction, but it's not. Worldwide, 3 million people's hearts are regulated with a pacemaker [1], 320,000 deaf people can hear again due to the cochlear implant [2], and over 135,000 Parkinson's patients' tremors are alleviated with a deep brain stimulating electrode [3]. More modern research aims to develop electronic implants which cure depression [4], enable fully functioning bionic arms [5], or even restore sight to the blind [6]. These ambitious goals are within reach and can be achieved by a unified effort from scientists, engineers, physicians, and entrepreneurs.

Teams of researchers in this field have been working together to better develop neural electronic implants and to think of new, innovative technologies, but they have come up against many hurdles. These implants must have a high density of stimulating sites to effectively modulate neural activity at the single neuron level. They should be capable of recording from thousands of neurons. Placing an implant into the body creates scar tissue, which in turn, pushes the very neurons you were trying to stimulate too far away. The implant must also be biocompatible, ideally indefinitely. Additionally, little is known about how electrically modulating neural tissue affects the spatiotemporal dynamics of neuron network activity. Or how plastic the brain is when understanding electrical stimulation.

Central to all of these challenges is the science behind the neural-electrical interface. This thesis takes a bioinspired approach to optimizing the neural-electrical interface by designing and testing novel electrode geometries and materials. We focus on restoring vision to blind patients using a retinal implant. However, many of the

improvements are generic to other neural prosthetic implants. Chapter 2 outlines how fractal electrodes can theoretically restore vision to a visual acuity of 20/80, compared to ∼20/1000 in typical retinal implants. The societal benefits of such an improvement would be staggering, allowing a previously blind patient with our electrodes to read text and recognize faces, whereas a patient seeing at a visual acuity 20/1000 has difficulty walking through a door unassisted. Chapter 3 explores a material system, carbon nanotubes, for our retinal implants and shows excellent neuron survival, neurite outgrowth, and neurite guidance when compared to materials used in implants today. Additionally, preliminary evidence suggests the body's scar formation mechanism in neural tissue may be mitigated by adopting specific carbon nanotube geometries. This is critically important for maintaining a close neuron-electrode interface. Chapter 4 switches from the neuron stimulation for the retinal implant, and instead presents a novel field effect transistor (FET) capable of recording from hundreds of neurons in vivo.

Before presenting the results, the remainder of this introduction provides an overview of the current state of retinal implants and the science behind the neuron-electrode interface. We begin by outlining which types of blindness retinal implants are designed to treat, the basic technology of the implant, and the clinical outcomes the implants achieve. Next, we cover the biology of healthy brain tissue, including: the structure of neurons, neuron signalling, and glia - the cells which support neuron health and neural signalling. Additionally, the architecture of the retina is discussed and the basics of visual processing in the retina are covered. We then switch to discussing how a voltage applied to a metal electrode extracellularly (i.e., outside of a cell) stimulates a neuron. Because there is a high concentration of salt ions in the extracellular space, applying a voltage to an electrode can lead to electrical charge

screening and chemical reactions at the electrode surface, both of which influence how the voltage extends into the extracellular space around a neuron. Next, we overview neuron adhesion on implant materials with varying surface chemistry and geometry; stronger adhesion can lead to more efficient neural stimulation. Finally, having established the materials and methods which can best stimulate neurons, we discuss a material system, carbon nanotubes, and an electrode geometry, fractals, which we propose will create the best electrode-neuron interface.

This thesis contains work previously published, work currently in publication, and unpublished work. Chapter 2 Section *Voltage controlled subretinal implant electrodes* contains co-authored work previously published in 2017 in the journal *Scientific Reports* [7]. Chapter 2 Section *Photovoltaic subretinal implants* contains co-authored work currently in publication [8]. Rick D. Montgomery and Richard P. Taylor are co-authors on the previously mentioned sections of Chapter 2. Chapter 3 Section *Retinal cell cultures on unfunctionalized vertically aligned carbon nanotubes* contains co-authored work currently in publication [9]. The co-authors listed in order are Saba Moslehi, Kara M. Zappitelli, Julian H. Smith, David J. Miller, Julie E. Chouinard, Stephen L. Golledge, Richard P. Taylor, Maria-Thereza Perez, and Benjamín Alemán.

Retinal Implants

The overarching goal behind retinal implants is to restore vision to blind patients who have lost photoreceptors (i.e., rods and cones) due to retinitis pigmentosa (RP) and age-related macular degeneragion (AMD). Each implant features the same fundamental architecture; the visual surroundings are transmitted to an electronic implant in the back of the eye which recreates a pixelized version of the image by

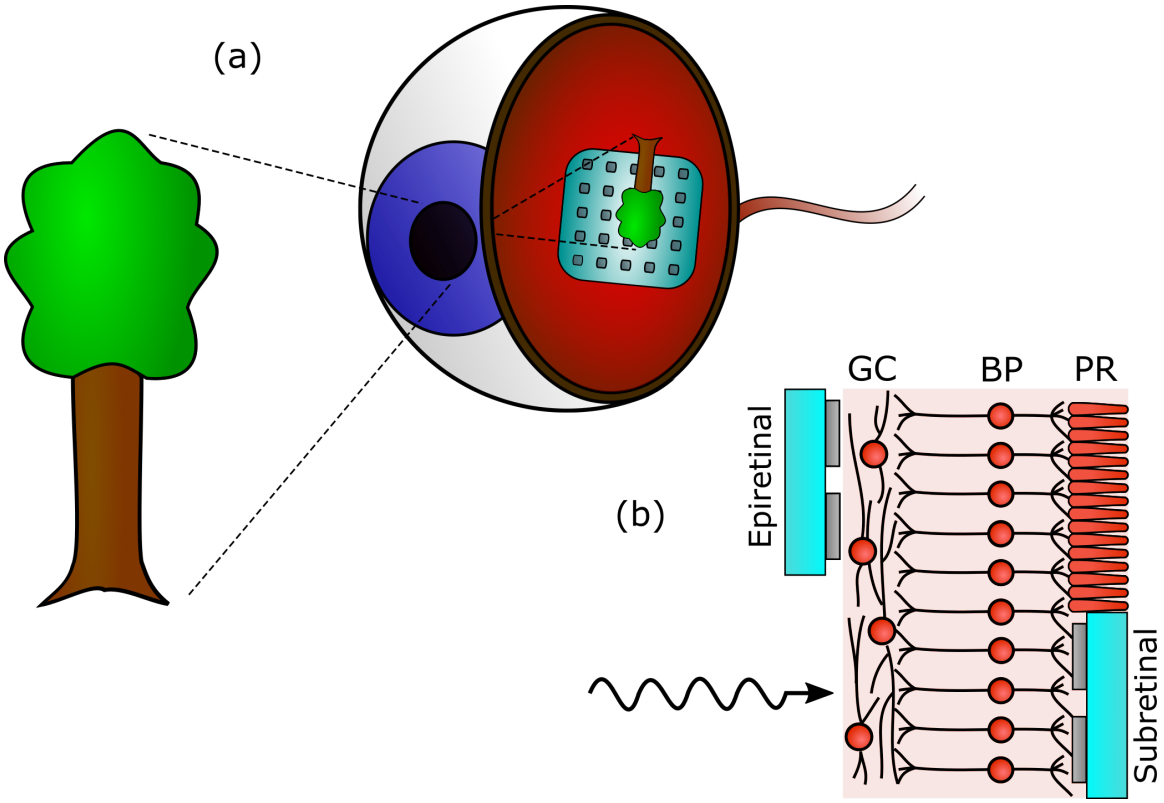

FIGURE 1. Fundamental architecture underlying retinal implants. (a) Electrodes in the back of the eye recreate the visual surroundings by applying charge to a set of pixels which then stimulate nearby neurons. Different implant placements on the retina as well as external power sources required to deliver enough charge to the pixels have been omitted in this simplistic picture. (b) Electrodes are placed either epiretinally (at the front of the eye) or subretinally (at the back of the eye). Epiretinal implants aim to stimulate ganglion cells (GC), while subretinal implants aim to stimulate bipolar cells (BP). Subretinal implants are placed where the photoreceptors (PR) were before retinal degeneration.

charging up electrodes which then stimulate nearby neurons (Fig. 1a). In a healthy retina, there are different layers of neurons (see Fig. 1b and Section 1.4) are organized in two-dimensional sheets stacked on top of each other. Each layer is necessary for visual processing. In RP and AMD however, the photoreceptor layer deteriorates, but the remaining layers of the retina remain intact [10] [11]. This allows for the remaining layers of the retina to be electrically stimulated with a pattern of the visual

field. Each pixel therefore acts as an 'electronic photoreceptor'. The exact design of retinal implants varies based off their placement on the retina, epiretinal (positioned at the front of the retina) or subretinal (positioned at the back of the retina) (Fig. 1b), the method of transmitting images of the visual surroundings to the implant, and the external powering required to deliver enough charge to the electrodes to stimulate the retinal neurons.

Retinitis pigmentosa and age-related macular degeneration

RP is a heridatary eye disease which causes progressive photoreceptor loss and affects ∼1/4000 people [12]. Photoreceptor loss begins in the peripherary of the retina, typically around young adulthood, and progresses towards the center resulting in tunnel vision by adulthood and no vision usually by 60 years. In the United States alone, ∼20,000 people are blind (visual acuity $< 20/200$ in the better seeing eye) due to RP [13].

AMD is an age-related disease which leads to a loss of functionality in the macula – the area of high photoreceptor density responsible for central vision. High blood pressure, smoking, alcohol consumption, ethnicity, or family predisposition can all increase the likelihood of acquiring AMD. In the United States, ∼11 million people have AMD with as many as 30% of those aged 75 or older acquiring the disease [14]. Furthermore, this number is expected to double by 2050 due to the rising aging population. There exist two forms of AMD; one is caused by accumulation of extracellular material into hard deposits, "dry form", while the other is caused by abnormal blood vessel growth beneath the macula, "wet form". The dry form accounts for 90% of AMD patients, but of those, only ∼1/200 go blind (∼50,000 people in U.S.) [14] [15]. No treatment currently exists for RP or dry AMD – providing

a significant driver for retinal implant development. Wet AMD, on the other hand, can be slowed considerably with intraocular injections or laser therapy [16] and thus the use of retinal implants as a restorative therapy is unlikely. Combined, the global cost of RP and AMD is in excess of $343 billion. [14].

Epiretinal implant

Three important steps guide epiretinal design: an external camera records the visual field, that information is then encoded into a set of electrical signals, and an electrode array stimulates the ganglion cell layer (Fig. 1b) with the encoded image pattern. In the first generation clinical trials of epiretinal implants, Humayun et al. (1999) used an external camera and image-processing chip set into a pair of goggles [17]. The signal was transferred wirelessly from the goggles to the implant using an implanted inductively coupled radio frequency (RF) coil. The signal then stimulated as many as 25 platinum disk electrodes with a diameter of 400 μm and a center-to-center spacing of 600 μm (i.e., 4 electrodes per mm^2). For comparison, the average density of ganglion cells in the human macula is $\sim$300/mm^2 and goes as high as $\sim$14,000/mm^2 [18]. All 10 patients in this study (9 with RP, 1 with AMD) reported seeing flashes of light and two patients could distinguish between vertical and horizontal lines. This epiretinal implant formed the basis for the formation of Second Sight Medical Inc and the ARGUS implant. ARGUS I was a 16 electrode platinum disk array which allowed patients to detect grating orientations with a spatial resolution set by the electrode spacing distance [19] [20] [21]. An additional study on ARGUS I demonstrated improved vision for patients partially blinded by RP through an increased ability to locate objects, discriminate the orientation of a capital letter L, and to detect an object's direction of movement [22]. Recently,

Second Sight's ARGUS II implant (60 platinum disk electrodes with diameter of 200 μm) has allowed patients to correctly identify letters with a visual acuity of up to 20/1000. A person with a visual acuity of 20/1000 can resolve an object from 20 feet away which a normal person could resolve at 1000 feet. A small subset of the tested patients could also read three and four letter words [23]. Pixium Vision is developing a similar epiretinal implant with 150 electrodes and has achieved an estimated restored acuity of $\sim$20/6000 in humans [24].

Subretinal implant

The guiding principile behind subretinal implants is straightforward; damaged rod and cone photoreceptors are replaced with microphotodiodes which directly stimulate bipolar neurons (Fig. 1b). Ideally, each photoreceptor would be replaced by a single microphotodiode. However, the current generated by a photodiode of this size would be insufficient for stimulating surrounding retinal neurons. The development of subretinal implants has been led, to a large extent, by three different groups. Each is covered separately in the following paragraphs.

The Chow brothers began their development of subretinal implants with stimulation of rabbit retinae [25]. Metallic strip electrodes were implanted into the subretinal space and attached to photodiodes outside of the body. Cortical recordings showed that light flashes on the photodiode induced enough current in the metallic strip electodes to induce neural activity. This design formed the basis for their development of a commercial company, Optobionics, and their implant, the Artificial Silicon Retina (ASR). The ASR implant was a microphotodiode array (MPDA) 2 mm in diameter and 25 μm thick, contained 5000 photodiodes each of size 20 μm x 20 μm, and used iridium oxide top-contact electrodes [26]. The implant was

designed to be powered solely off incident light. The implant was also well tolerated and showed no infection, prolonged inflammation, or erosion in both cat [27] and human eyes [26]. During their 2004 experiment, 6 patients with RP were enrolled. Electroretinograms (the eye-version of an EKG) were used to verify that the ASR induced neural activity in response to IR stimulation. All 6 patients demonstrated improved text recognition and task performance. In the best of cases, one patient had an improvement in visual acuity from worse than 20/1600 to 20/400 5 months after implantation. Despite the progress, the authors reported that improvement was unlikely to be due to direct electrial stimulation. Instead they hypothesized that the electrical stimulation indirectly supported regrowth of retinal neurons. These results could not be repeated and led to Optobionics going bankrupt shortly thereafter.

The mechanism by which vision improvement occured for the 6 patients in the 2004 Chow et al. study created a large source of controversy within the retinal implant community. Optobionics lead competitor of the time, Eberhart Zrenner claims, "Only with the aid of an external energy source will the light from the normal environment be sufficient to modulate the stimulating current at each individual electrode" [6]. A quick, back of the envelope calculation indicates that power beyond that supplied by normal lighting conditions is likely needed for a photodiode to directly stimulate surrounding neurons. First, what current, I_{fire}, is needed to stimulate a neuron? The photodiode area, A, is about $20\,\mu$m x $20\,\mu$m. Retinal tissue resistivity, ρ, is $\sim 3500\,\Omega$cm [28]. And, a neuron typically fires if the extracellular potential, ΔV_e, drops by 15 mV across the distance of its soma, $\Delta x = 10\ \mu$m. Then from Ohm's law, $I_{fire} = \frac{1}{\rho} A \frac{\Delta V_e}{\Delta x} = \frac{1}{3500\,\Omega\text{cm}} (20\,\mu\text{m})^2 \frac{15\,\text{mV}}{10\,\mu\text{m}} = 1.7\,\mu$A. Next, what current can a microphotodiode generate? A typical photodiode responsivity, R, is 0.3 A/W and direct sunglight (i.e. looking straight at the sun) has an irradiance, I_{rad}, of $1000\,\text{W/m}^2$. The generated

current is then $I_{photodiode} = RAI_{rad} = 0.3\,\mathrm{A/W} \times (20\,\mu\mathrm{m})^2 \times 1000\,\mathrm{W/m^2} = 0.14\,\mu\mathrm{A}$. Even if you are looking directly into the sun, I_{fire} is an order of magnitude larger than $I_{photodiode}$. For normal home or office lighting, the situation becomes even worse.

In the early years of subretinal implant development, the Chow brothers were competing with Zrenner's group, Retinal Implants AG, to develop the first subretinal implant. Zrenner et al. (1999) used a similar pixelized microphotodiode array (MPDA) with $25\,\mu$m resolution and gold or titanium nitride (TiN) stimulation sites [29]. Extracted retinas were placed between an MPDA touching a multielectrode array. By shining light of ∼70% direct sunlight (70 kLux) onto the MPDA, ganglion cell activity could be recorded from the multielectrode array. Thus indicating the MPDA was capable of stimulating the surrounding neurons (the bipolar neurons), which then transmitted their signal signal through the various retinal layers (to the ganglion cell layer). To reduce the intensity requirements for stimulation, Zrenner's group added in electronic amplifiers which receive power from an external battery attached to the MPDA through a transocular cable [30] [31] [32]. In the electronically amplified MPDA implants, the photodiode top-contact no longer served as the stimulating electrode. Instead, the photodiode acted as a light detector which activated a nearby stimulating electrode. The photovoltage was multiplied through internal electronics and sent to the stimulating electrode. These implants formed the basis for clinical trials beginning in 2010 [32]. The implant used had 1500 pixels each with a size of $72\,\mu\mathrm{m} \times 72\,\mu\mathrm{m}$ and containing a $50\,\mu\mathrm{m} \times 50\,\mu\mathrm{m}$ TiN electrode. Six patients underwent a variety of vision tests including: detecting grating orientations, Landolt 'C' test, reading letters, and identifying shapes. In all tests, a statistically significant visual improvement occurred with the implant on versus implant off. A maximum visual acuity of 20/1000 was restored. More recent experiments have shown

a visual acuity of up to 20/546 [33] [34], although only four out of twenty-nine patients passed the Landolt 'C' test for any visual acuity.

During the mid-2000s the Palanker group began presenting ideas for a subretinal implant which combined some of Optobionic's ideas with some of Retinal Implants AG's ideas. Their group recognized that external power was needed to create a sufficient current to induce neural stimulation. However, they wanted to avoid the transocular cable required in the Retinal Implants AG's design. Instead, they proposed external goggles which the patient would wear, that send an amplified infrared image of the visual surroundings onto the multi-photodiode array [35] [36] [37]. IR radiation is used because: (1) the cornea and lens are transparent to IR, (2) maximum irradiance is higher for IR than visible, and (3) silicon photodiode efficiency is best in the near IR [38] [39]. Their implant features several theoretical advantages over their competitors. First, they link three photodiodes serially together into pixels sized $70\,\mu$m to $280\,\mu$m to increase the generated voltage up to 1.5 V, allowing for greater stimulation of nearby neurons [36]. Next, they employ a local ground electrode which minimizes stimulation cross-talk for neurons above neighboring pixels [38]. Finally, they have etched holes in their device allowing for nutrient flow through the implant [36]. In addition to these advantages, they have also explored integrating three-dimensional pillars into their chips to obtain better retinal adhesion [35] [40], although this three-dimensional architecture is not employed in current devices. While no clinical trials have been peformed yet, they have demonstrated a restored acuity in rats with RP to half the acuity of a standard rat [41].

Retinal implants are promising for restoring vision to patients blinded by RP, and potentially AMD. In one sense, the current research is astounding; prevously blind patients have had their vision restored up to 20/546. On the other hand, if the

pixels were transmitting their signals in a one-to-one ratio with the neurons, these patients could have a visual acuity of 20/80. At 20/80 acuity, patients would be able to read large font sized text and recognize faces. Until these two goals are achieved, retinal implant research must continue to progress.

Neural Stimulation

The primary purpose of a neuron is to process and transmit information through electrochemical signalling between neurons [42]. As a first understanding, the neuron consists of: input terminals, the dendrites; a processing center, the cell body; a cable which transports the information, the axon; and export terminals, synaptic buttons. Chemical signalling is accomplished through neurotransmitters which are released from synaptic vesicles in the presynaptic button to the postsynaptic receptor. Electrical signalling can be accomplished by changing the electrical potential near the neuron so that charged ions flow into or out of the neuron.

The intracellular part of the neuron is separated from the extracellular space by a lipid bilayer membrane and ion channels (Fig. 2). The lipid bilayer membrane is largely impermeable to the flow of cations and anions. As a result, there is an imbalance of ions across the membrane resulting in an electrochemical potential. Ions attempt to reduce this electrochemical potential by flowing through ion channels. These ion channels, in general, only allow the flow of cations and anions when influenced by these electrochemical gradients. The primary ions which flow into and out of the neuron consist of Na^+, K^+, Cl^-, and Ca^{2+}. The electrochemical separation of ions gives rise to an intracellular potential, V_{in} and extracellular potential, V_{out}. The difference of these potentials is referred to as the membrane potential, V_m.

$$V_m \equiv V_{in} - V_{out} \tag{1.1}$$

Neurons are *depolarized* if $V_m > 0$ or *hyperpolarized* if $V_m < 0$.

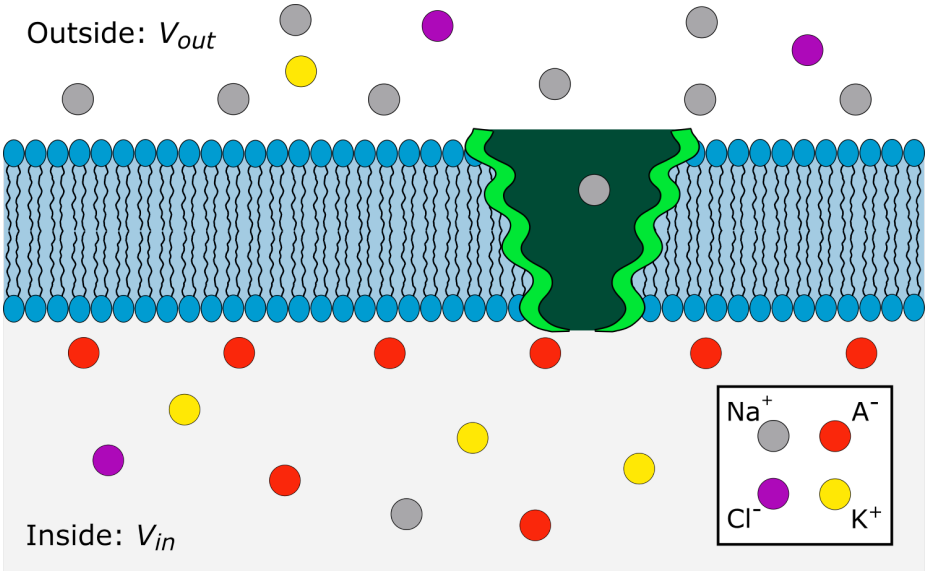

FIGURE 2. Cell membrane.
The inside of the neuron is separated from the extracellular space by a lipid bilayer membrane (blue) and ion channels (green). Charged proteins, cations, and anions are separated resulting in electrochemical potential across the membrane.

Each ionic species experiences a net electric field as well as a diffusive driving force. The potential difference which prevents diffusion of that ion across the membrane is known as the resting potential or Nernst potential. For ion type, i, with valence charge, z, and an internal concentration, $[C_i]_{in}$, and an outside concentration, $[C_i]_{out}$, the resting potential, E_i, is

$$E_i \equiv V_m(I = 0) = \frac{kT}{zq} \ln \frac{[C_i]_{out}}{[C_i]_{in}} \tag{1.2}$$

where k is the Boltzman constant, T the temperature, and q the electron charge. The net current across the membrane, I_m, is zero at rest. Typical equilibrium potentials in a mammalian cell are $E_{Na^+} = +90$ mV, $E_{K^+} =$ -90 mV, $E_{Cl^-} = -90$ mV, and $E_{Ca^{2+}} = 140$ mV. The neuron's membrane potential at rest, E_m, is given by the weighted average over each ionic species

$$E_m = \frac{\sum_i g_i E_i}{\sum_i g_i} \tag{1.3}$$

where g_i is the conductance of ion, i, across the membrane at the resting potential. The resting potential for a typical mammilian neuron is -70 mV.

Passive neuron model

Passive neuron models are relevant for neurons below the threshold depolarization which initiates an action potential or for neurons which feature no voltage-gated ion channels. In particular, bipolar neurons (the neurons targeted by subretinal extracellular stimulation) can adequately be modelled by passive neuron models [43] [44]. A passive neuron's membrane can be modeled as a resistor and capacitor in parallel (Fig. 3). The lipid bilayer creates an impermeable separation between charged ions, i.e. a capacitor, while ion channels establish a narrow pore for ions to flow through, i.e. a resistor.

The current across the membrane, I_m is that of a standard parallel RC circuit.

$$I_m = C_m \frac{dV_m}{dt} + \frac{V_m - E_m}{R_m} \tag{1.4}$$

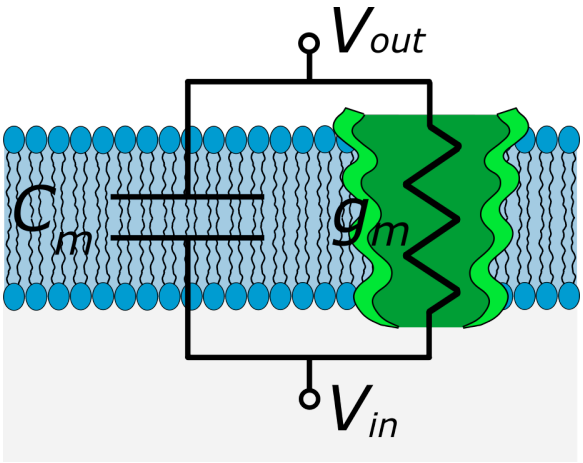

FIGURE 3. Passive cell membrane circuit model.
The cellular membrane behaves as a resistor (ion channels) and capacitor (lipid bilayer membrane) in parallel. The membrane capacitance is C_m and the membrane conductance is g_m. The membrane potential, V_m, results from an imbalance in anions, cations, and charged proteins between the intracellular and extracellular medium.

Where R_m is the membrane resistance. The sign convention for currents is negative for positive ions flowing from the outside to the inside. The membrane capacitance and resistance of a typical neuron are $R_m \sim 1 \times 10^4\,\Omega\text{cm}^2$ and $C_m \sim 1\mu\text{F/cm}^2$ giving a membrane time constant of $\tau_m \sim 10$ ms.

To complete the picture of the passive response of a neuron, we must also investigate the membrane potential of axons and dendrites. In contrast to the soma, the membrane potential of the axons and dendrites varies depending on position along the axon or dendrite. An appropriate model can be constructed by taking an infinite cable which allows current to leave the cable through a parallel RC branch (Fig. 4). From Fig. 4, we can tell the membrane potential will decrease along the axon since current can leave through the membrane. Exactly how the membrane potential decays with distance is determined by the cable equation.

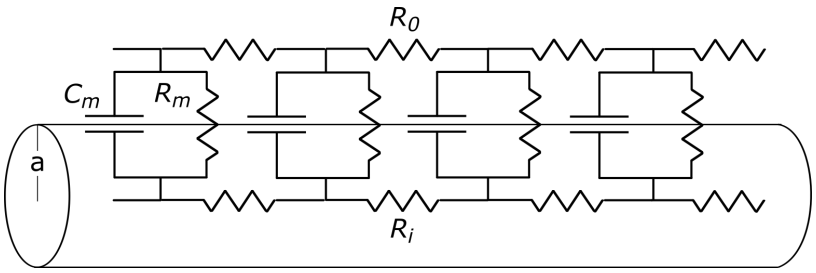

FIGURE 4. Cable model for axons and dendrites.
Cable model assumes (i) membrane resistance, R_m and membrane capacitance, C_m are constant, (ii) no azimuthal current flow, and (iii) $R_0 = 0$, where R_0 is the extracellular resistance. The axon radius is a and the intracellular resistance is R_i.

$$\lambda^2 \frac{\partial^2 V_m(x,t)}{\partial x^2} = \tau_m \frac{\partial V_m}{\partial t} + V_m \tag{1.5}$$

where the space constant,λ, and the time constant, τ_m, can be written in terms of the typically used geometry independent parameters

$$\lambda = \sqrt{\frac{aR_m}{2R_i}}, \tau_m = R_m C_m \tag{1.6}$$

The cable equation has the familiar term of $\tau_m \partial V_m/\partial t$ which describes the response rate of the membrane potential to an applied stimulus. However, due to the current escaping the membrane along the axon, the membrane potential decays with distance away from the source. The distance at which the membrane potential decays by $1/e$ gives the length constant. For a typical neuron, $a \sim 0.5\,\mu$m, $R_m \sim 1 \times 10^4\,\Omega$cm^2, and $R_i \sim 100\,\Omega$cm, giving $\lambda = 50\,\mu$m.

Active Membrane

Active neurons, as compared to passive neurons, feature voltage-gated ion channels and undergo action potentials (Fig. 5). The action potential is a spiking

event caused by positive feedback of inward Na^+ ions. It was correctly described first in 1949 by Hodgkin and Huxley [45] who made the important discovery that ion channels are selective. I.e., a sodium ion channel only conducts Na^+ and is impermeable to other ions, such as K^+. The full sequence of the action potential is as follows. (1) The neuron begins at a resting potential (Fig.5) determined by the differences in ion concentrations inside and outside of the cell. (2) The firing event, i.e. the action potential, begins when V_m depolarizes to the threshold level (typically about 15 mV). This results in a positive feedback of Na^+ channels opening and a rapid influx of Na^+ ions into the neuron. (3) As the potential reaches the peak, K^+ begins flowing out of the neuron and the potential decreases. (4) Finally, there is a resting period where the ions are actively pumped out of the neuron and the resting membrane potential is re-established.

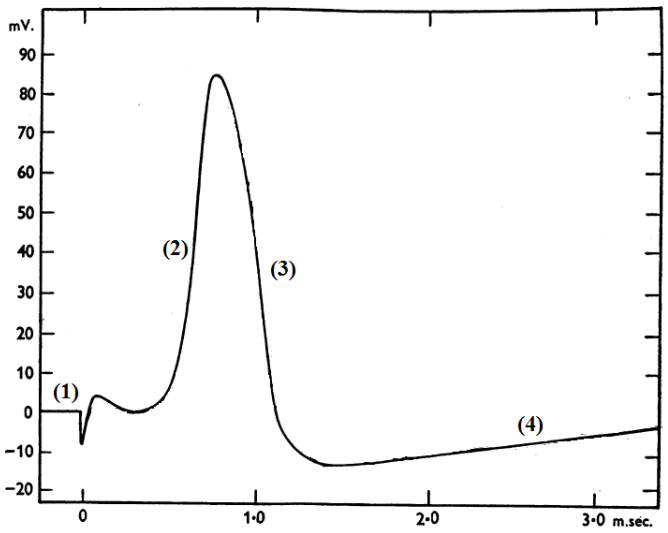

FIGURE 5. Action potential.
An example of an action potential in the squid giant axon. The vertical axis is the membrane potential, V_m, and the horizontal axis is time. Image from Hodgkin and Huxley (1949) [45].

The full dynamics of this action potential is captured in the equivalent circuit model with selective voltage-gated channels for each ion as shown in Figure 6. The membrane current is

$$I_m = C_m \frac{dV_m}{dt} + \bar{g}_K n^4 (V_m - E_K) + \bar{g}_{Na} m^3 h (V_m - E_{Na}) + \bar{g}_L (V_m - E_L) \qquad (1.7)$$

where $\bar{g}_K$ and $\bar{g}_{Na}$ are constant conductances in response to large membrane depolarizations and hyperpolarizations. Typical values for the conductances are $\bar{g}_K \sim$ 30 mS/cm^2 and $\bar{g}_{Na} \sim 100$ mS/cm^2. The gating probabilities given by n, m, and h are complicated solutions to differential equations.

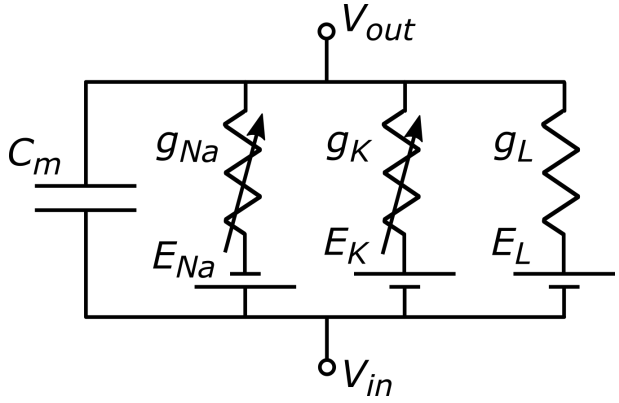

FIGURE 6. Hodgkin-Huxley equivalent circuit.
Na and K ion channels selectively conduct Na^+ and K^+ ions, respectively. Their resistivity is dependent on V_m. E_{Na} attempts to push Na^+ ions inwards while E_K attempts to push K^+ ions outwards. The leak channel models the neuron's natural permeability with total conductance g_L and Nernst potential E_L.

To wrap up the discussion of an active firing event, let us investigate how an action potential propagates along an axon or dendrite. The propagation can be illustrated through use of a picture, Fig. 7. An action potential usually begins in the

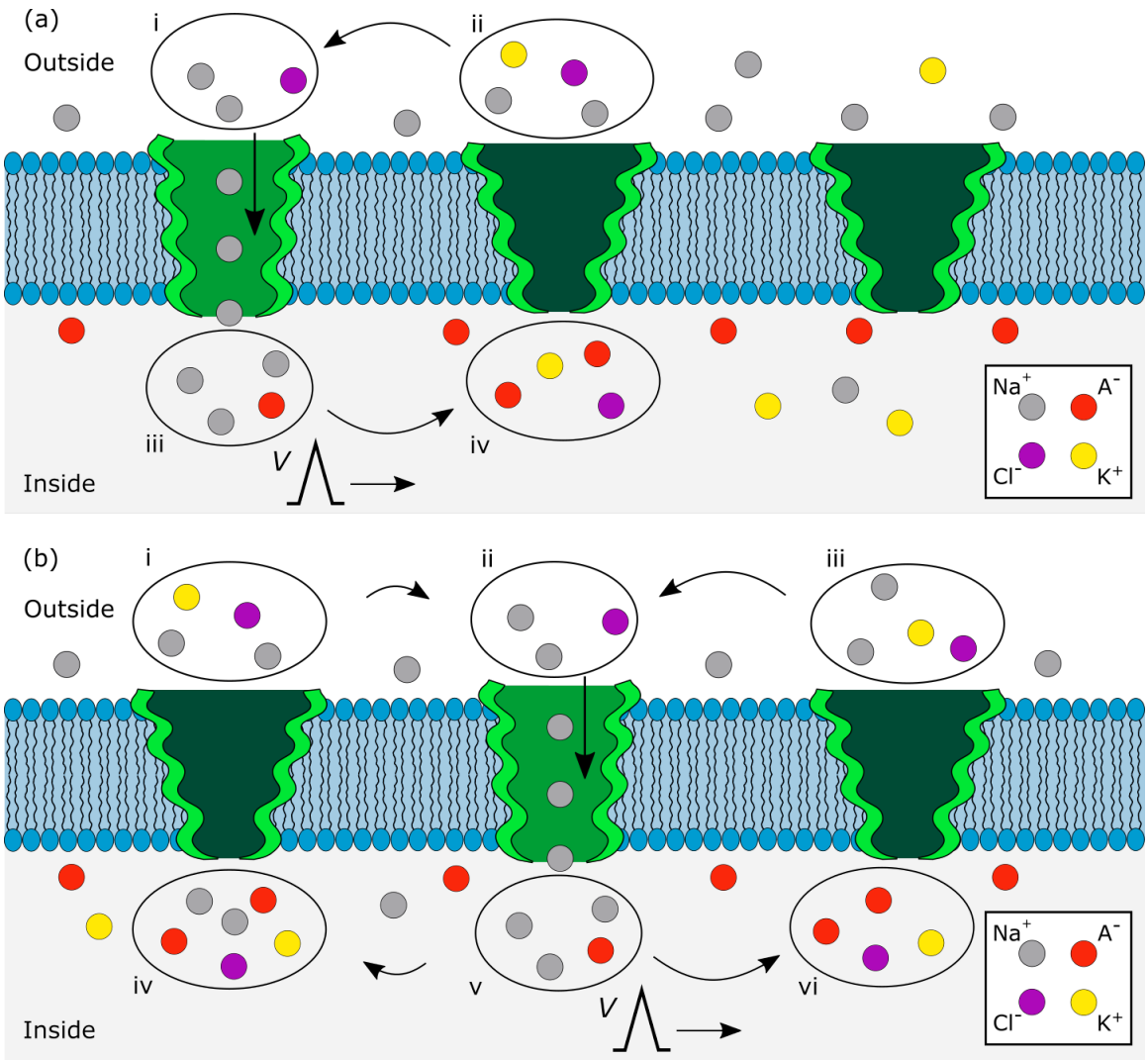

FIGURE 7. Action potential propogation
The green arrows indicate the direction of Na^+ current and the action potential is shown as a travelling spike.

soma, whether from a current stimulus or presynaptic neurotransmitters, and travels outwards through the axon. The action potential corresponds to an influx of Na^+ ions (Fig. 7a). This inwards current results in a net depletion of Na^+ ions immediately outside the membrane and a surplus inside the membrane. Electrodiffusive forces will push the Na^+ ions in the direction indicated in Fig. 7a. Now the next ion channel down the line (Fig. 7b), sees a larger Na^+ inside the membrane and becomes

depolarized enough to allow the ion channel to open. The action potential continues to propagate in this cork-screwing manner along the axon.

The speed at which this action potential propogates can be found from the cable model discussed previously. The propogation velocity is the distance the signal occupies along the axon divided by the membrane response time. Using (1.6) gives a conduction velocity, v, of

$$v = \frac{1}{C_m}\sqrt{\frac{a}{2R_iR_m}} \tag{1.8}$$

Typical values for conduction velocity are on the order of 10 m/s to 100 m/s.

Extracellular neuronal stimulation

Restoring sight through a retinal implant requires extracellular stimulation of the surviving healthy layers of the retina. How extracellular voltages extend into the electrolytic fluid surrounding a neuron is discussed in the upcoming section. The mechanism by which an action potential can be induced extracellularly is described below for both somatic stimulation and axonal stimulation.

The sequence of events illustrated in Fig. 8 describes the mechanism for inducing an action potential at the soma with an external field. Consider a neuron between two capacitor plates. At rest, the neuron's internal potential is about -70 mV (Fig. 8a). Now, let a constant electric field be applied to the neuron (Fig. 8b). If the cytoplasm was non-polarizable, superposition of these two potentials would show that the membrane potential is still -70 mV on both sides of the cell despite the applied field (Fig. 8c). However, in reality, the cytoplasm is conductive. Internal ions flow to oppose the field and reduce the field strength internally, causing one side of

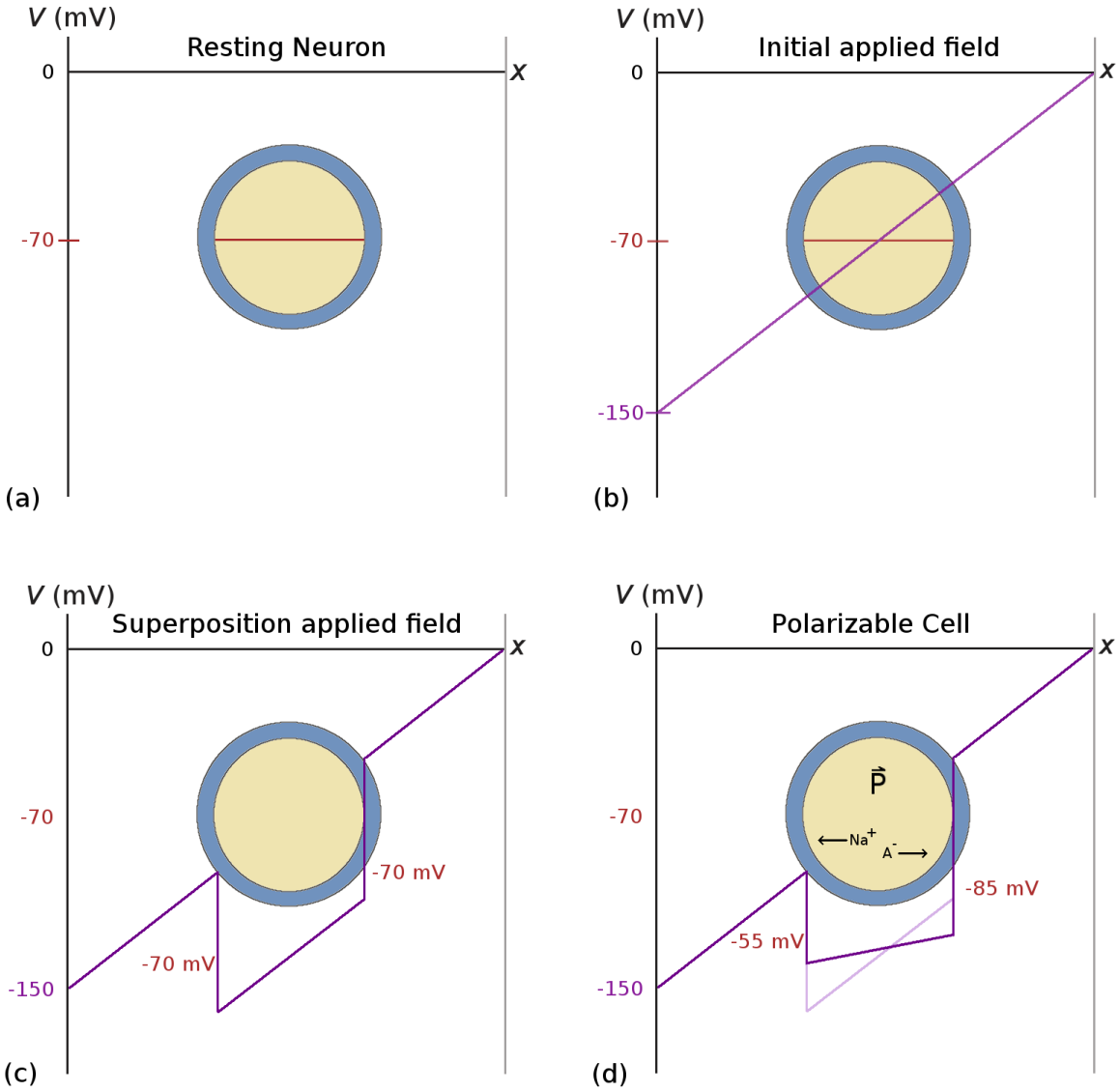

FIGURE 8. Sequence of events outlining extracellular neuron stimulation. Potential is plotted on vertical axis and distance on horizontal axis. The neuron is illustrated by a soma with a lipid bilayer membrane (blue) and an internal cytoplasm (beige).

the neuron to depolarize and the other to hyperpolarize (Fig. 8d). All it takes is a depolarization of about 15 mV across a small patch of membrane for all sodium ion channels to open and the neuron to fire.

External electrodes which stimulate axons running parallel to an electrode, such as peripheral nerve cuff electrodes used in prosthetic limbs, induce firing activity according to the activation function, f, which is proportional to the second spatial derivative of extracellular voltage, V_e, along the nerve axon [46].

$$f \propto \frac{\partial^2 V_e}{\partial x^2} \tag{1.9}$$

Positive values of f indicate a local depolarization of the nerve axon while negative values give a hyperpolarization. In particular, the activation function is important for epiretinal implants which use axonal stimulation to induce action potentials [47] [48].

Glia

Neurons have historically been viewed as the most important cell in the brain. However, in the human brain, 90% of cells are glia while only 10% are neurons [49]. In the most broad sense, the role of glia is to support neurotransmission. Without glia, neurons would die. There are three types of glia in the brain: astrocytes, oligodendrocytes, and microglia. Astrocytes provide a scaffold for neurons to grow on, encapsulate synapses in order to increase synaptic coupling, maintain homeostasis of ionic and neurotransmitter concentrations in the extracellular space, and signal blood vessels to constrict or dilate in order to control oxygen levels. Oligodendrocytes produce myelin and ensheath axons. Myelin is required to ensure a fast propogation velocity of action potentials down the axon. Finally, microglia act as the brain's immune cells. Microglia explore the brain in order to detect damage, engulf dead cells, and remove debris.

In the retina, the three types of glia cells are astrocytes, microglia, and Müller cells [50]. Astrocytes and microglia are located throughout the retina and have similar functions in the brain as in the retina. Müller cells are glia that extend through all retinal layers and have many of the same functions as astrocytes. They encapsulate neurons to improve synaptic coupling, maintain homeostasis, and provide structural support to the retina. Additionally, they regulate the volume of the retina and provide metabolites to microglia.

Disorders like trauma, infection, or neurodegeneration can initiate reactive gliosis – a process where astrocytes and Müller begin enlarging in an attempt to protect healthy portions of the retina [50]. For mild to moderate damage, this process may reverse. However, in cases of severe damage the reactive gliosis will advance to a glia scar – a thick layer of glia through which neuron axons and dendrites can no longer pass [51]. This is particularly problematic for retinal implants, which by nature, create damage upon implantation. For example, Turner et al. (1999) showed implantation of a silicon probe created a dense glia scar $\sim$150 μm in diameter after 6 weeks of being implanted [52]. This dense glia layer pushes the target neurons far away from the stimulating sites. Which in turn, prevents high resolution stimulation required for restoring visual acuities to useful levels.

Can glia scar formation be avoided upon device implantation in the retina? Potentially. Glia scar formation responses decrease with decreasing implant size [53] [54] [55]. For example, glia scar thicknesses after 5 weeks were 0.6$\pm$1.8 μm for 2.1 μm diameter implants and 25.5$\pm$10.0 μm for 26.7 μm diameter implants [53]. Glia formation in cortex is also increased when the implant is tethered to the head due to increased vibrations at the implant site [55]. As such, the retinal implant used by Palanker's group has a significant advantage over other groups in that it is completely

wireless. Other groups are creating electrodes which have a Young's modulus below the brain's critical rupture strength, 3 kPa, in order to reduce implant micromotions [56]. Yet another approach involves pre-loading the implant with an anti-glia drug, dexamethasone, to reduce glia scar formation [57]. Glia can also be 'herded' by the device geometry. Piret et al. (2015) showed that on rows of gallium phosphide nanowire (similar to a bed of nails) 100 μm wide separated by 100 μm of flat silicon, glia preferentially grew in the silicon gaps [58]. We are pursuing this method of using geometry to herd glia in between active electrode areas in subretinal implants in order to improve the neuron-electrode coupling.

Retina

The retina sits at the back of the eye and is responsible for the first stages of visual prossessing (Fig. 9). For a good modern overview of the retina, see Ref. [59]. When light enters the eye, it passes through the inner retina and is then absorbed by rod and cone photoreceptors. These photoreceptors hyperpolarize in response to light. Rods and cones are organized into a dense array which act like a set of pixels in a camera.

Horizontal cells provide the first steps in visual processing: local gain control and edge enhancement. Horizontal cells are inhibitory cells (they reduce the membrane potential of neurons they are connected to) connected to photoreceptors and bipolar cells. At rest, i.e. in the absence of light, photoreceptors try to depolarize by releasing the neurotransmitter glutamate. But, glutamate leads to inhibitory GABA (a different neurotransmitter) production in horizontal cells which causes negative feedback on the photoreceptors. At rest, these two processes reach an equilibrium. Now, when light strikes a photoreceptor, glutamate production is reduced which in

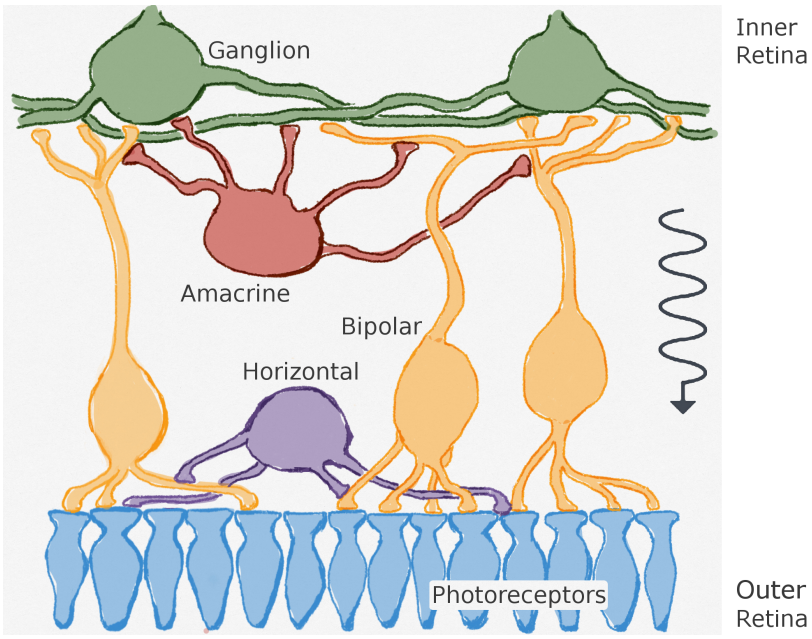

FIGURE 9. The retina.
There are five main classes of neurons in the retina. Photoreceptors, horizontals, and bipolars all respond to light with graded potentials (i.e., passively). Amacrine cells exhibit both passive and active membranes. Ganglion digitize the sum of signals from bipolars and amacrines and send action potential spikes to the optic nerve.

turn reduces GABA production of the horizontal cell. Since horizontal cells are wide spreading cells with synaptic connections to many photoreceptors, the neighboring photoreceptors also sense the reduction in GABA and depolarize. This depoarization of photoreceptors surrounding a bright object gives edge enhancement. The total sum of glutamate which a horizontal cell measures is averaged out over all the photoreceptors it connects to. This averaging out is akin to local gain control – allowing us to see both bright and dim objects simultaneously without the bright object saturating the total field of view.

To a first approximation, bipolar cells transmit graded potentials (i.e. bipolars are passive and do not undergo action potentials) from the photoreceptor layer to the ganglion cell layer. However, lateral spreading horizontal and amacrine cells also

affect the bipolar cell's membrane potential. Most mammals have 11 cone bipolar cells and 1 rod bipolar cell. Each bipolar cell connects to every photoreceptor within its dendritic reach and each cone is connected to 11 cone bipolar cells [60]. Thus, each cone transmits its signal in parallel to 11 different cone bipolars. As an analogy to electronics, each cone bipolar acts as a bandpass filter.

Amacrines connect to bipolars and ganglions and provide both lateral and vertical inhibition in the retina. Amacrine cells have a diverse set of roles in image processing, many of which are still not known. I will consider just one example here of object motion detection provided by Ref. [61]. How does the eye detect moving objects from a stationary background even though the eye itself is naturally moving? In the ganglion cell layer, a subset of ganglions detect object motion. These would fire continously if not inhibited by amacrines. Amacrine cells are very wide spreading cells that have synaptic outputs on $\sim$10 mm^2 of the retina but only receive synaptic inputs from about $\sim$ 500 μm^2. When the entire background moves from natural eye movements, synaptic inputs from bipolar cells cause all amacrines to inhibit the signal across the entire retina. However, when only a portion of the visual field moves, only amacrines under the moving object inhibit. The difference in signals from background motion and object motion do not overlap and the moving object is detected by the ganglion cells.

Ganglion cells perform the final stage of visual processing in the retina by digitizatizing bipolar and amacrine inputs. There are at least 20 kinds of ganglion cells each with their own role in interpreting the visual surroundings [59]. One example is a blue-ON, green-OFF ganglion cell. This ganglion cell is connected to two types of bipolar cells: bipolars which depolarize when blue cones hyperpolarize (blue-ON) and bipolars which hyperpolarize when green cones hyperpolarize (green-OFF). This

ganglion cell then outputs a train of action potentials rapidly at blue wavelengths and then less and less rapidly as the wavelength switches through yellow and onto green.

Electrochemistry for Extracellular Neuronal Stimulation

Because neurons operate in an electrolytic environment, the neuron-electrode interaction is highly dependent on the effects of mobile ions. The mobile sodium, potassium, chlorine, and other ions cause the extracellular space to be conductive. This conductivity causes two important processes to occur at the electrode-electrolyte interface: (i) charge screening and (ii) oxidation-reduction reactions. These processes would not occur if the extracellular space were nonconductive.

Physical processes of electrolytic capacitors

Typically, capacitors are used in circuits to store charge. The amount of charge, Q, that can be stored per volt, V is given by the capacitance, C, as

$$C = \frac{Q}{V} \tag{1.10}$$

For a parallel plate capacitor with area, A, and separation of the plates, d, the capacitance is given by

$$C = \frac{\epsilon A}{d} \tag{1.11}$$

where ϵ is the permitivitty of the dielectric material between the plates. Compared to conventional capacitors, electrolytic capacitors offer the ability to (1) store more charge on the plates through a process known as Debye screening, and (2) conduct DC currents through charge reactions at the surface as described below.

Electrical double layer

What does the electric potential look like inside an electrolytic capacitor? Before the electrode is biased (i.e., before a voltage is applied to the electrode), dissociated anions and cations are floating around the solution in a diffusive equilibrium. When the electrode is initially biased (Fig. 10a), the electric field acts the same as it would in a nonconducting material with a given permitivitty. There is an instaneous displacement current from the dipole moment of water molecules orientating along the electric field. However, the ions have not yet begun to conduct. As time goes on,

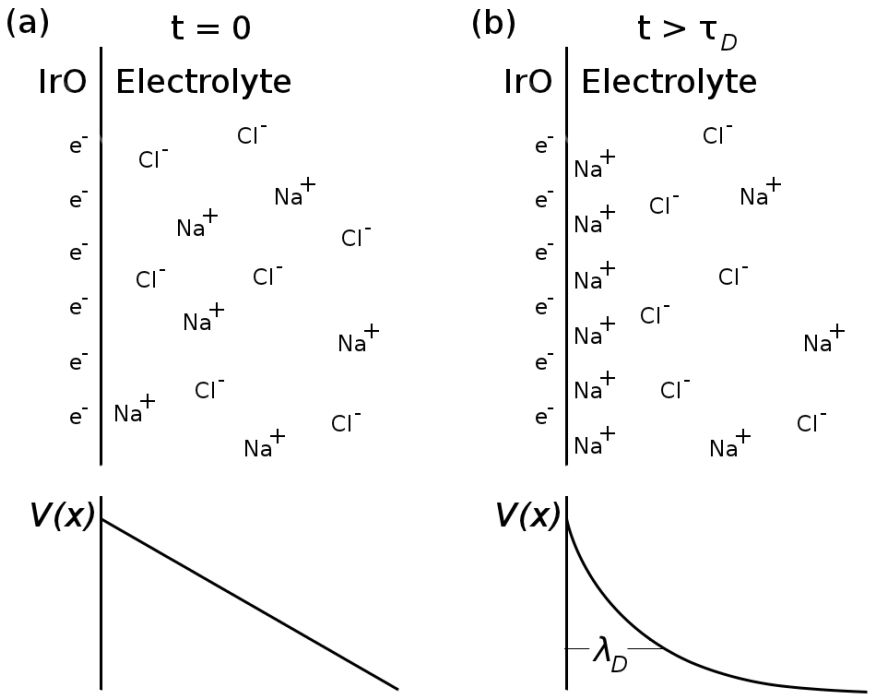

FIGURE 10. Debye screening for a biased electrode in an electrolyte. As an example, an iridium oxide electrode (labelled IrO) is biased in a NaCl electrolyte. Initially (a), the electric field only responds to the permitivitty of the fluid and not the conductive ions. The Na^+ then begin to move towards the negatively biased electrode. (b) After τ_D, the electric potential decays exponentially with a space constant of λ_D.

cations will be attracted towards the anode and anions towards the cathode. After some time, enough mobile ions will pile up on at the electrode's surface to cancel the charge on the plates provided by the battery, (Fig. 10b). The distance which the potential has dropped by $1/e$ is known as the Debye length, λ_D, and the time which it takes to screen the potential is known as the Debye time, τ_D.

Poisson's equation and Boltzmann statistics can be used to determine λ_D and the form of the potential drop. Poisson's equation is

$$\nabla^2 V = -\frac{\rho}{\epsilon} \tag{1.12}$$

where ϵ is the permitivitty of the fluid and ρ is the charge density. In terms of Boltzmann statistics, the charge density can be written as

$$\rho = q n_0^+ e^{-qV/kT} - q n_0^- e^{qV/kT} \tag{1.13}$$

where n_0^+, and n_0^- are the initial concentrations of positive and negative ions, respectively. Assuming the negative and positive ions are in equal concentration, combining (1.12) and (1.13), and linearizing the exponential term for $qV << kT$ gives

$$\nabla^2 V = \frac{q^2 n_0}{\epsilon k T} V \tag{1.14}$$

From (1.14), V decays exponentially with a space constant known as the Debye length.

$$\lambda_D = \sqrt{\frac{\epsilon k T}{q^2 n_0}} \tag{1.15}$$

For the extracellular regions in a human body, $\lambda_D \sim 1$ nm. Thus, if you apply a static voltage to an electrode in an electrolyte, the voltage will decay exponentially fast to zero within a few nanometers.

Drift velocity, chemical mobility, and diffusion coefficient

Ions in the bulk of the electrolyte undergo (i) resistive flow when an electric field is applied and (ii) thermal diffusion. The resistive flow is due to the ions scattering off water molecules while trying to flow down their electrical gradient. Force balance between the driving force and resistive force is

$$F = m\frac{v_d}{\tau} = qE \tag{1.16}$$

where m is the mass of the ion, v_d is the drift velocity, and τ the average time between collisions. Solving for the drift velocity gives

$$v_d = \frac{q\tau}{m}E \equiv \mu E \tag{1.17}$$

where μ has been defined as the chemical mobility. For a Na^+ ion, $\mu \approx 0.5 \times 10^{-3}$ $cm^2/V{\cdot}s$.

The extent of diffusion by the ions is controlled by the diffusion coefficient, D. The diffusion coefficient is related to the chemical mobility through the Einstein kinetic relation. In steady state, the current density, J, for an ion with concentration, c, is

$$J = 0 = J_{diff} + J_{drift} = -D\frac{d\rho}{dx} + v_d\rho \tag{1.18}$$

where J_{diff} is the ion diffusive current density and J_{drift} is the current density of ion drift. The charge density can be described with Boltzmann statistics as in (1.13). Solving for (1.18) by using (1.13) and (1.17) gives the Einstein relation

$$D = \mu kT \tag{1.19}$$

For Na^+ ions at $T = 310\,\mathrm{K}$, $D \approx 1.5 \times 10^{-5}$ cm^2/s.

Poisson-Nernst-Planck equations

Poisson's equation and Boltzmann statistics give the potential when the ions have reached a steady state response to the electrode bias. However, the time dependent response of the ion concentrations must be determined by a coupled set of non-linear partial differential equations known as the Poisson-Nernst-Planck equations. For an ion concentration, c, with a diffusion coefficient, D, they are given by

$$\begin{aligned} \nabla^2 V &= -\frac{q}{\epsilon} c \\ \frac{\partial c}{\partial t} &= D\nabla^2 c + \nabla(\frac{qD}{kT} c \nabla V) \end{aligned} \tag{1.20}$$

The second equation says that the concentration current, $\partial c/\partial t$, is dependent on a diffusive force, $\nabla^2 c$, and a driving force, $\nabla(c\nabla V)$. The concentration and potential are then coupled through Poisson's equation.

Faradaic reactions: charge transfer at the electrode/electrolyte interface

When the electrode is biased strongly enough, chemical reactions start occurring at the electrode-electrolyte interface. These chemical reactions are often referred to as *Faradaic reactions*. Faradaic reactions involve a charge transfer across the interface through processes such as (i) simple electron transfer, (ii) oxidation-

reduction reactions, (iii) water hydrolosis and (iv) electrode dissoulution. Hydrolysis refers to having enough voltage on the electrode to break H_2O molecules, creating O_2 and H_2 gas.

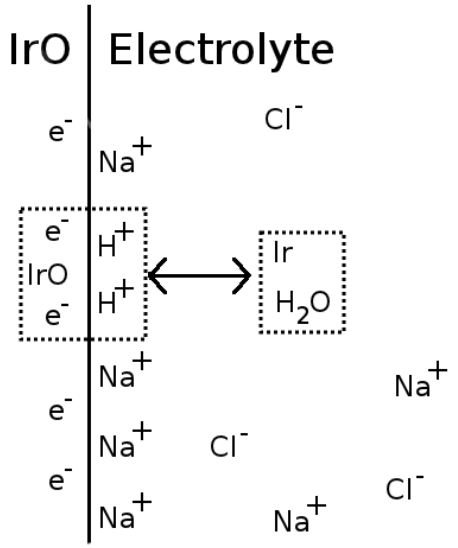

FIGURE 11. Faradaic reaction at an electrode surface in an electrolyte. An example of oxidation-reduction occurring at the IrO electrode - NaCl electrolyte interface. If the reaction is not confined to the surface, toxic iridium atoms will enter the cellular space.

Reversible Faradaic reactions are reactions which do not change the pH of the electrolyte and cause no electrode dissolution. These reactions are reversed by changing the direction of current across the electrode interface in a sufficiently short time period. Any chemical reaction which happens for one current direction, becomes reversed for the other direction. An example of a reversible iridium oxide oxidation-reduction reaction is shown in Equation 1.21 and illustrated in Fig. 11.

$$IrO + 2H^+ + 2e^- \Longleftrightarrow Ir + H_2O \tag{1.21}$$

where the left hand side of the equation occurs in the electrode and the right hand side occurs in the electrolyte. By reversing the direction of current across the interface, the reaction can be reversed and there will be no build-up of iridium ions in the electrolyte (provided the current is reversed on a timescale short enough that Ir ions in the electrolyte have not diffused away).

Irreversible Faradaic reactions are any Faradaic reactions which cannot be reversed. One example is applying a sufficiently high voltage to the electrode surface to induce water hydrolysis, thereby creating O_2 and H_2 gas which escape from the electrolyte. Irreversible Faradaic reactions are unsafe for neural stimulation [62].

Equivalent circuit model for electrical stimulation in an electrolyte

Electrochemistry of the electrode-electrolyte interface and ion flow through the electrolyte can be simply modeled by an equivalent circuit (Fig. 12). The current is carried by electrons on the electrode side and by ions on the electrolyte side. First, a capacitor, C_{dl}, models the separation of charge across the interface (i.e., the electrical double layer). The charge is separated by a distance of λ_D in a material with permitivitty ϵ so that the capacitance (per unit area) is

$$C_{dl} = \frac{\epsilon}{\lambda_D} \tag{1.22}$$

Typical values for the double layer capacitance of a metal are $C_{dl} \sim 10 - 100\,\mu\text{F/cm}^2$. Next, in parallel with the double layer capacitance, is the charge transfer resistance, R_{ct}. R_{ct} controls the amount of Faradaic reactions occurring across the surface. In general, R_{ct} is a nonlinear function dependent on the electrode bias, E. As an approximation, R_{ct}, has infinite resistance for small E and a constant impedance at high E. The majority of current for large biases is a Faradaic current. Finally, the

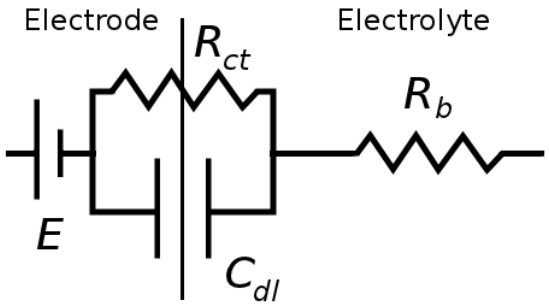

FIGURE 12. Electrochemical cell equivalent circuit model
The equivalent circuit model captures all the dynamics of an electrochemical cell. Debye screening across the interface is modeled by C_{dl}, Faradaic reactions by R_{ct}, ion resistance by R_b, and the applied potential by E.

ions in the electrolyte also encounter a frictional force while moving through the fluid. This frictional force acts as a bulk resistance, R_b. By unit analysis, an expression for the bulk resistance can be given as

$$R_b = \frac{\lambda_D^2 L}{\epsilon D} \tag{1.23}$$

where L is the length of the cell and D is the diffusion coefficient. An electrolytic parallel plate capacitor without any Faradaic reactions and with a plate separation of 1 mm in an electrolyte with ion concentrations similar to the body ($\lambda_D \sim 1\,\text{nm}$, $D = 1.5 \times 10^{-5}\,\text{cm}^2/\text{s}$, and $\epsilon = 80{\times}8.85 \times 10^{-12}\,\text{C}/(\text{V}\cdot\text{m})$) will have a bulk resistance of $R_b \sim 10\ \Omega\text{cm}^2$. Using (1.22) and (1.23) gives the Debye time scale

$$\tau_D = C_{dl} R_b = \frac{\lambda_D L}{D} \tag{1.24}$$

The Debye time scale for electrolytic parallel plate capacitor described above is $\tau_D \sim 0.5\,\text{ms}$.

Three ways to derive the extracellular potential in an electrolytic capacitor for no Faradaic reactions

In the previous sections, we outlined the processes of charge screening (Debye shielding) and electrochemical reactions (Faradaic reactions) at the electrode-electrolyte interface. In particular, when a static voltage is applied to an electrode surface and there are no Faradaic reactions, the voltage in the electrolyte will drop exponentially fast to zero in a distance λ_D and reach equilibrium after a time τ_D. Thus, static voltages cannot be used for neural stimulation because the voltage surrounding the neuron will be effectively zero.

In order to overcome Debye shielding, time-dependent voltages must be applied to the electrode. Because there is a time delay between when an electron arrives at the electrode surface and when an ion in the electrolyte arrives to screen it, time-dependent voltages will be only partially screened. This section illustrates three models to derive the electric field in the electrolyte for time-dependent voltages when no Faradaic reactions are present.

A simple model

Consider an effective charge, Q_{eff}, built up on the capacitor plates which is the difference between charge supplied by the battery and charge supplied by the electrolyte (Fig. 13). The electrolytic capacitor will then act exactly like a standard capacitor except with an effective charge which screens the electric field in the center. The electric field, E, in the center will be

$$E = \frac{V}{L} = \frac{Q_{eff}}{CL} = \frac{Q_{eff}}{\epsilon A} \tag{1.25}$$

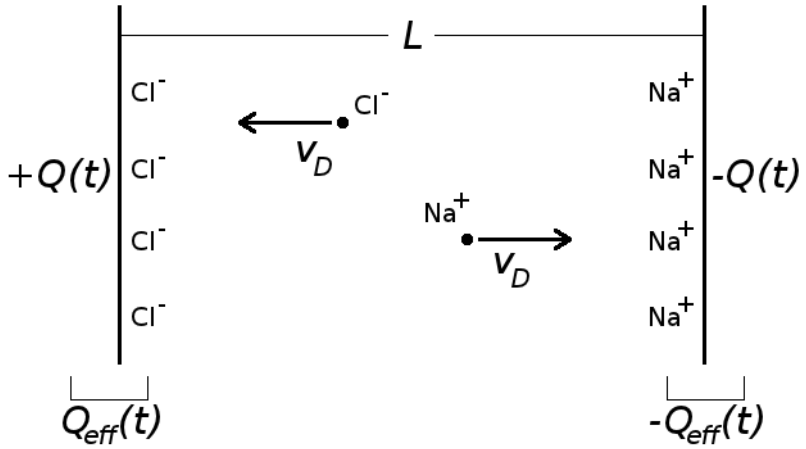

FIGURE 13. Simple model for electric field in an electrolytic capacitor. An effective charge, Q_{eff}, is built up on the capacitor plates with permitivitty ϵ and separated by a distance L. The battery is supplying the charge, *Q(t)*. For simplicity, the ions have the same drift velocity, v_d.

Let a constant current, I_0, be applied to the electrodes. And for simplicity, assume the Na^+ and Cl^- ions have the same chemical mobility. Then, the effective charge is given by

$$Q_{eff} = Q_{batt} - Q_{elec} = I_0 t - qAv_d[\mathrm{Na}^+]t \tag{1.26}$$

where Q_{batt} is the charge supplied by the battery and Q_{elec} is the charge arriving at the electrode surface from the electrolyte. Inserting into (1.25), plugging in (1.17), and solving for the electric field gives

$$E = \frac{I_0 t}{\epsilon A + q\mu A[\mathrm{Na}^+]t} \tag{1.27}$$

In the limit that $[Na^+]$ goes to zero, the standard capacitor case is recovered with $E = I_0 t/\epsilon A$. Unexpectedly, in the limit of time getting large, $E = I_0/q\mu A[\mathrm{Na}^+]$, approaches a constant value independent of the distance between plates or the

permitivity. The ions in the electrolyte thus have a small time delay before being able to arrive and shield the charge arriving from the electrode.

Finite element analysis approach on the Poisson-Nernst-Planck equations

Another approach towards determining the electric field in an electrolytic capacitor is to solve the Poisson-Nernst Planck equations (1.20). The PNP equations were solved for a capacitor 20 nm in length and an applied voltage of $V(t) = 1{\times}10^5$ [V/s]t between 0 and 0.1 μs using the finite element solver COMSOL (Fig. 14).

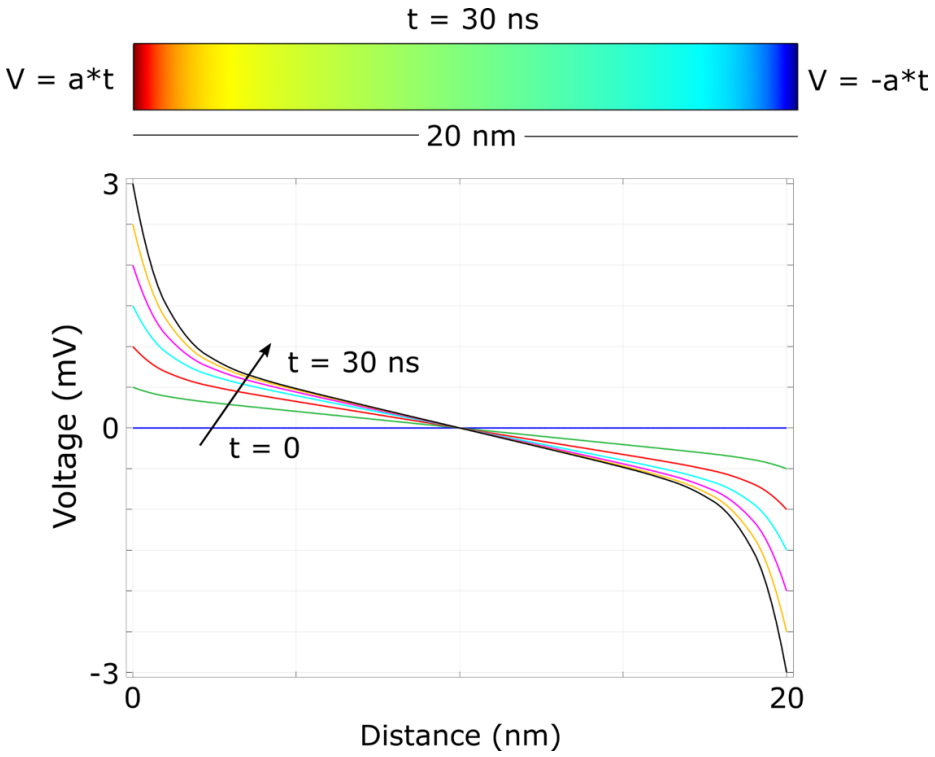

FIGURE 14. Poisson-Nernst-Planck solution to electric field in an electrolytic capacitor.
(top) The voltage inside the electrolyte after 0.1 μs of applying a linear ramp voltage to the top and bottom plates. (bottom) The voltage inside the electrolyte. Each line represents the voltage versus distance at a given time. The voltage begins at zero and steadily increases at the left electrode surface and steadily decreases at the right electrode surface. However, after a certain time, the electric field in the center becomes constant.

The effect of Debye screening is evident in Fig. 14a where the majority of the potential drop is in the first 2 nm next to the electrode surfaces. However, because we are applying a time dependent potential, the electrolyte response to shielding the charge on the electrode is delayed and a non-zero electric field is observed in the electrolyte. Figure 14b shows how the electric field approaches a constant value of $\sim$100 μV/nm after a time of $\sim$20 ns. This timescale corresponds with that given by the Debye timescale, Equation (1.24).

Equivalent circuit model

The equivalent circuit model described previously can also be used to determine the electric field inside a capacitor (Fig. 15). Qualitatively, the equivalent circuit shows that the Debye charge screening, i.e. C_{dl}, will block low frequency signals.

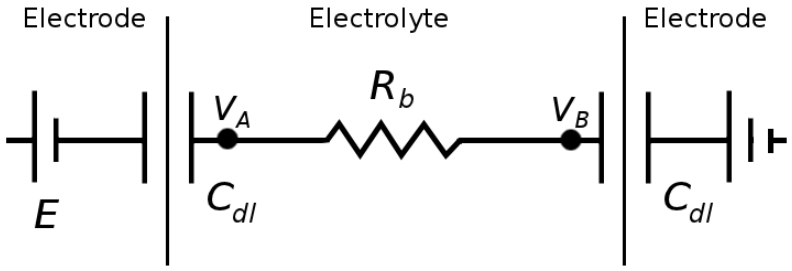

FIGURE 15. Equivalent circuit for an electrolytic capacitor with no Faradaic reactions.
A voltage, E, is applied to the left electrode while the right electrode is held at ground. The interface between electrode and electrolyte is modelled by a double layer capacitance, C_{dl}. The electrolyte also features a bulk resistance R_b. The potential inside the electrolytic capacitor is measured at two locations, V_A and V_B.

The potential difference through the electrolyte, $V_A - V_B$, can be solved using Kirchoff's current conservation as shown below.

$$I = C_{dl} d_t (V_A - E(t)) = \frac{V_B - V_A}{R_b} = C_{dl} d_t V_B \tag{1.28}$$

For a sinusoidally varying applied field, $E(t) = V_0 \cos(\omega t)$, the potential difference across the electrolyte is

$$\begin{aligned} V_A - V_B &= \frac{\omega \tau_D V_0}{\sqrt{4 + (\omega \tau_D)^2}} \sin(\omega t + \phi) \\ \phi &= \pi - \arcsin\left(\frac{\omega \tau_D}{\sqrt{4 + (\omega \tau_D)^2}}\right) \end{aligned} \tag{1.29}$$

where $\tau_D = R_b C_{dl}$ is the Debye time constant. The field is thus screened by a factor of $\omega \tau_D / \sqrt{4 + (\omega \tau_D)^2}$. In the DC limit $\omega \to 0$, $V_A - V_B \to 0$.

Extracellular potential when Faradaic reaction current is most significant

When the electrode potential is large, the majority of the current in the surrounding electrolyte will be due to Faradaic charge transfer at the interface [63]. In this case, the double layer capacitance can be ignored.

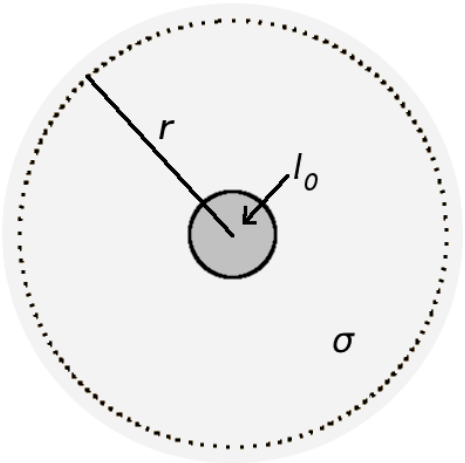

FIGURE 16. Spherical current source in an electrolyte.
An example of a spherical electrode (dark gray) bounded by an electrolyte (light gray, conductivity σ) with a constant inwards Faradaic current, I_0.

Consider a spherical electrode held at a large potential so that there is a constant inward Faradaic current of I_0 across the interface (Fig. 16). The surrounding electrolyte has a conductivity, σ. Then, the current density, J, at a distance r away is

$$J = -\frac{I_0}{4\pi r^2} \tag{1.30}$$

And in the electrolyte Ohm's law is

$$J = \sigma E \tag{1.31}$$

Since E is spherically symmetric, $E = \partial V/\partial r$. Equating (1.30) and (1.31) and integrating with respect to r gives

$$V(r) = \frac{I_0}{4\pi\sigma r} \tag{1.32}$$

Thus, constant inward currents create time-independent voltages that fall off as $\sim 1/r$ at large voltages when Faradaic reactions are most significant.

Electrochemical measurements

Characterization of electrode materials is performed using cyclic voltammetry and electrochemical impedance spectroscopy. Cyclic voltammetry identifies the extent of Faradaic and capacitive reactions at an electrode surface. Electrochemical impedance spectroscopy measures the current passed between the source and ground electrodes at a given frequency. These measurements form the standard for choosing safe and effective neural stimulating devices.

Cyclic voltammetry

Cyclic voltammetry is a three electrode measurement in which a current is passed between a working electrode (i.e., source electrode) and counter electrode (i.e., ground electrode) with the potential measured with respect to a distant reference electrode. The working electrode is the material being investigated and can exhibit reversible Faradaic reactions, irreversible Faradaic reactions, and capacitive reactions. The counter electrode typically a large area ($> 100,000\ \mu\text{m}^2$) platinum electrode with only capacitive reactions. Although the counter electrode is ideally held at 0 V, reactions at the surface can cause the counter electrode potential to drift. Therefore, a third electrode, the return electrode is placed far from the working and counter electrodes and has a well-defined voltage which the working and counter electrode voltages can be measured with respect to.

To measure the IV-characteristics of an electrode, the potential is increased and decreased at a constant rate between the limits at which hydrolysis occurs on the surface. Because hydrolysis leads to oxygen and hydrogen gas production, neural electrodes must be kept within the hydrolysis limits in order to be safe. A typical voltage versus time waveform is shown in Fig. 17.

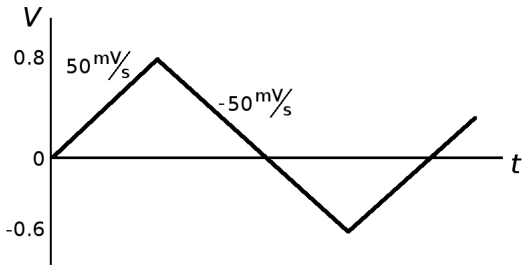

FIGURE 17. Cylcic voltammetry applied waveform.
An example of a potential swept at a rate of ±50 mV/s betwen the hydrolysis potential limits, -0.6 V to 0.8 V.

The current measured from sweeping the potential gives an IV-curve which indicates which type of reactions are occuring at the interface. An illustrative example of the difference between Faradaic and capacitive type electrodes is shown in Fig. 18. A purely capacitive electrode features constant currents (which switch between negative and positive) because the voltage sweep rate is linear and only the capacitive portion, $I = C\frac{dV}{dt}$, contributes to the current. Faradaic electrodes feature peaks at the voltages which initiate electrochemical reactions at the electrode surface.

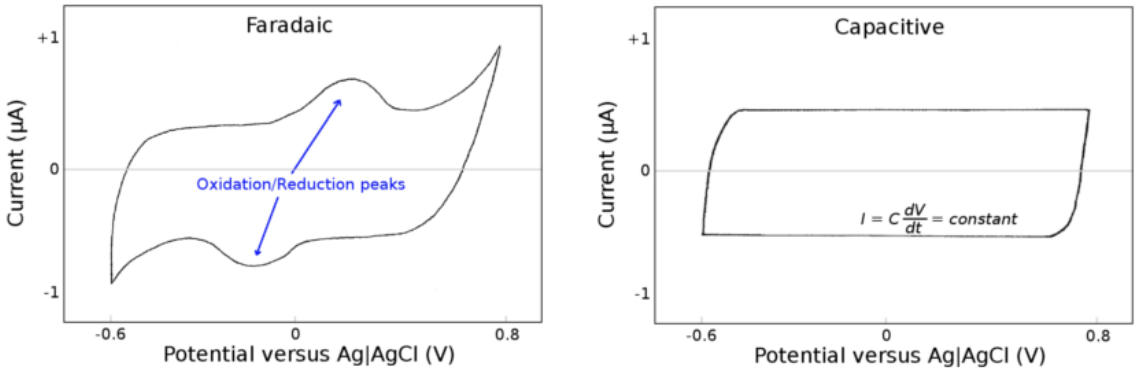

FIGURE 18. Cyclic voltammogram.
Faradaic reactions exhibit peaks corresponding to oxidation and reduction occuring at the electrode surface while capacitive electrodes exhibit an approximately constant current over the potential range.

The IV-curves obtained from cyclic voltammetry are also used to quantify the amount of charge which can be safely injected during stimulation of neural tissue. The charge injection limit, Q_{inj}, is given by the time integral of the cathodic current (Fig. 19). Two requirements limit Q_{inj}: (1) maintaining the electrode potential between the hydrolysis limits and (2) having equal charge delivered during the cathodic and anodic phases. In the first requirement, increasing the electrode potential beyond the hydrolysis limit produces hydrogen gas. And as an example of not enforcing the second requirement, consider the chemical redox reaction of an iridium oxide electrode

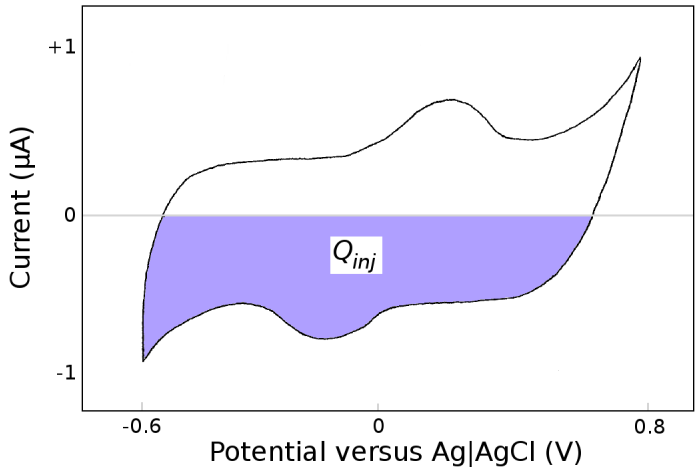

FIGURE 19. Determination of charge injection limit.
The area of the negative current (cathodic) between the potential hydrolysis limits gives the reversibly injected charge limit, Q_{inj}.

discussed previously in Equation 1.21. If this redox reaction is not balanced during the cathodic and anodic stimulation phases there will be a build up of iridium in the tissue. Furthermore, the build up of electrons on the electrode will shift the electrode potential over time which can lead to the applied voltage exceeding the hydrolysis limits.

Electrochemical impedance spectroscopy

Electrochemical impedance spectroscopy measures the impedance and phase between the working and counter electrodes. A small sinusoidal potential is applied to the working electrode and impedance versus frequency is measured. An example log-log plot of impedance versus frequency is shown in Fig. 20. At low frequencies, the capacitive component of impedance, $Z_C \sim 1/\omega C_{dl}$, at the working electrode's surface dominates while at high frequencies the resistive component of impedance due to the bulk resistance of the electrolyte, $Z_R \sim R_b$ dominates. Effective stimulation of

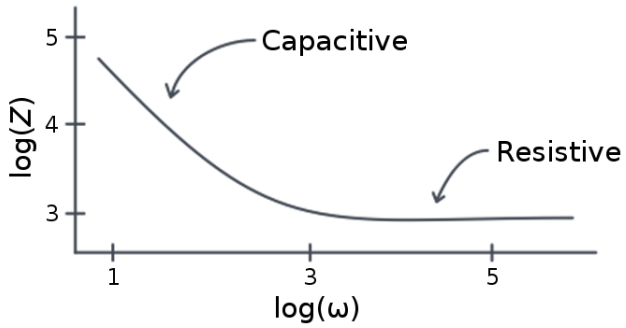

FIGURE 20. Electrochemical cell impedance plot.
Impedance diagram showing the characteristic capacitance dominated impedance and resistive dominated impedances of the electrochemical cell.

neurons aims to have a low impedance (i.e. greater current through the resistive electrolyte) at around 1 kHz (the neuron's firing frequency).

Stimulation of Tissue

Effective and safe stimulation of neural tissue requires delivering a sufficient potential to the extracellular tissue while at the same time avoiding electrode degredation. The amount by which the extracellular potential changes is dependent on C_{dl}, R_{ct}, R_b, and the stimulating waveform. If the electrode potential is raised too high or if the waveform is not charge-balanced, gas can be generated or electrode degredation can occur releasing toxic elements into the surrounding tissue.

Electrode materials

Safety limits for neural electrodes are often reported by the charge injection limit, Q_{inj}. This charge may pass through either the resistive or capacitive branches of the electrode/electrolyte interface so long as the electrode potential remains within the hydrolysis limits and the delivered cathodic and anodic charge is equal. Different electrode materials have different hydrolysis limits as well as conduct differently

through the resistive and capacitive branches. An ideal electrode would be purely capacitive with a double layer capacitance large enough (at least 1 mF/cm^2) to deliver a sufficient external potential. This ideal electrode would prevent deposition of the electrode material into the surrounding tissue. In absence of a perfectly capactive electrode, resistive electrodes injecting current reversibly can be used.

Early neural stimulating electrodes mainly focused on platinum, iridium oxide, and titanium nitride. Rose and Robblee (1990) measured Q_{inj} as 50 - 150 μC/cm^2 for platinium electrodes with a 0.2 ms charge-balanced biphasic current pulses [64]. Biphasic current pulses refer to current pulses which alternate between negative and positive. Titanium nitride and and iridium oxide are porous electrodes – this creates a larger surface area and thus increases Q_{inj}. Faradaic acting activated iridium oxide films (AIROF) were measured to have a charge injection limit of 1 mC/cm^2 and 2 mC/cm^2 for 0.2 ms cathodic and anodic pulses, respectively [65]. Later measurements on Q_{inj} for AIROF electrodes pulsed at 0.2 ms reported Q_{inj} as 4 mC/cm^2 *in vitro* [66] and 0.9 mC/cm^2 *in vivo* [67]. Sputtered iridium oxide film (SIROF) electrodes can increase Q_{inj} slightly over AIROF electrodes, 1 mC/cm^2 versus 0.9 mC/cm^2 [67]. Charge injection between 2 - 3 mC/cm^2 causes degredation of AIROF electrodes and deposition of iridium into the surrounding tissue [68]. AIROF electrodes show a significant decrease in Q_{inj} during long term pulsing of the electrode in tissue [69]. Titanium nitride injects charge capacitively providing an attractive alternative over the other Faradaic electrode materials. However, at frequencies used for neural stimulation TiN has a charge injection limit of 0.9 mC/cm^2 [66], lower than that of iridium oxide. C_{dl} for TiN is between 1 - 2.5 mF/cm^2 [66] [70]. Platinum, titanium nitride, and iridium oxide are still the materials used in retinal implants today because of their long accepted use of operating in the human body.

Electrode Material	Reaction Type	Q_{inj} (mC/cm^2)	C_{dl} (mF/cm^2)	Pulse Duration (ms)	Ref.
Pt	Capacitive/ Faradaic	0.05 - 0.15	—	0.2	[64]
TiN	Capacitive	0.95	1.25	0.5	[66]
		0.55	1.0	0.2	
		—	2.5	—	[70]
AIROF	Faradaic	1 - 2	—	0.2	[65]
		5.75	6.5	0.5	[66]
		4	5.2	0.2	
		2	—	0.4	[68]
		0.9	—	0.2	[67]
		0.5	—	0.1	
SIROF	Faradaic	1.9	—	0.3	[67]
		1	—	0.2	
PEDOT	Faradaic	3.6	—	0.1	[71]
		2.3	—	1	[72]
PEDOT/ CNT	Capacitive	2.5	—	1	[73]
TiN/CNT (3D)	Capacitive	—	10	—	[70]
TiN/CNT (2D)	Capacitive	—	2	—	[74]

TABLE 1. Charge injection limits and double layer capacitances of different electrode materials.

Two new promising neural electrode materials are based off a Faradaic conducting polymer, PEDOT, and capacitive carbon nanotubes, CNTs. The charge injection limit of PEDOT electrodes has been measured to be 3.6 mC/cm^2 on 2,500 μm^2 electrodes [71] and 2.3 mC/cm^2 on 10,000 μm^2 electrodes [72]. PEDOT electrodes implanted into tissue have been shown to have low cytotoxicity [75]. Three-dimensional hemispherical carbon nanotube electrodes have shown a 4 times increase in double layer capacitance over TiN electrodes, 10 mF/cm^2 versus 2.5 mF/cm^2 [70]. They have also been integrated into thin flexible films to improve biocompatibility

while still maintaining a relatively high double layer capacitance of 2 mF/cm^2 [74]. Luo et al. (2011) built capacitive PEDOT/CNT composities with a Q_{inj} of 2.5 mC/cm^2 for 1 ms pulses [73]. These PEDOT/CNT composites remained mechanically stable for 24 hours of 100 mV/s CV sweep between -0.9V and 0.5V. A summary of the charge injection limits and double layer capacitances for the different electrode materials is provided in Table 1.

Neuron Adhesion and Cell Cultures

Neuron adhesion, proliferation (cell division), and neurite outgrowth is mediated by the *extracellular matrix* (ECM). The ECM is a semi-rigid scaffold of proteins which (1) provides cell support, (2) influences cell division, and (3) directs neurite growth [76]. Neurons respond to these ECM proteins through transmembrane (spanning through the lipid bilayer membrane) receptors called *integrins*. Below, I'll begin with a brief overview of neurite adhesion and outgrowth. Then, I'll give an in depth overview on *in vitro* cell cultures and explain how neurons respond to varying surface chemistry, nanotopography, and microtopography. Finally, I'll finish up with a few examples of substrate elasticity and electric fields influencing neurite outgrowth.

Biological overview of neurite adhesion and outgrowth

Integrins are a set of transmembrane receptors approximately 10 nm in size which mediate cell-cell and cell-ECM interactions. *Ligand* binding at integrin sites activates intracellular signalling mechanisms responsible for cell adhesion, proliferation, and neurite outgrowth [77]. (Ligands generally refer to any molecule which binds to a protein receptor and then produces a signal.) The most common integrin ligands are ECM proteins such as laminin, collagen, or fibronectin. Different cell types

express certain integrins more strongly so that cell attachment is preferred on specific ECM proteins. Cell attachment to the ECM causes integrins to cluster and form *focal complexes* of size $\sim 0.25\,\mu\text{m}^2$ at the leading edge of the neurite [78]. These focal complexes assemble and de-assemble on a time scale of minutes. Some focal complexes will recruit other proteins and grow into large (greater than $1\,\mu\text{m}^2$ stable *focal adhesions*. Focal adhesions become fixed at the substrate and in the *cytoskeleton*, providing an anchoring point for cells to generate force. (The cytoskeleton is a network of filaments which provides structural integrity to the cell.) Axon elongation and direction is then determined by the *growth cones* [79]. Growth cones sample the surroundings through the *lamellopodium* (a flowing mesh of actin proteins) and *filopodia (rigid actin rods)*. The axon elongates and chooses a direction based off chemical and physical cues in the lamellopodium and filopodia.

Surface Chemistry

In the world of biomaterials research, substrates are often chemically modified to improve cell adhesion in a process called functionalization. Broadly, functionalization refers to any process which adds functional groups to the surface. For neural cell cultures, surfaces are typically biochemically functionalized with ECM proteins such as laminin, collagen, or fibronectin or cell adhesion molecules (CAMs) such as poly-L-lysine. Additionally, surfaces can be functionalized through chemical treatment methods such as exposure to oxygen plasma.

ECM protein functionalization occurs through either adsorption or covalent conjugation. In the case of adsorption, ECM proteins are first dispersed in solution and coated over the substrate (Fig. 21a). The amount of adsorped protein and the orientation of adsorption are dependent on the protein's charge distribution

and hydrophobicity coupled with the substrate's charge and hydrophobocity [80]. ECM proteins belong to a subfamily of proteins called glycoproteins. In contrast, to almost all other proteins, glycoproteins are hydrophilic and adhere preferentially to hydrophilic substrates [80]. Next, when the cells are placed onto the surface they are dispersed in cell culture medium which contains large hydrophobic proteins, such as the plasma protein albumin. Depending on the hydrophobicity of the substrate, these large hydrophobic proteins will have a higher binding affinity to the surface and will displace the ECM proteins (Fig. 21b-c). Without ECM proteins on the surface, there will be no binding sites for the neuron's through their integrin receptors, leading to poor adhesion. Thus, as as a general rule of thumb, hydrophilic surfaces promote neuron adhesion while hydrophobic surfaces deter it [81].

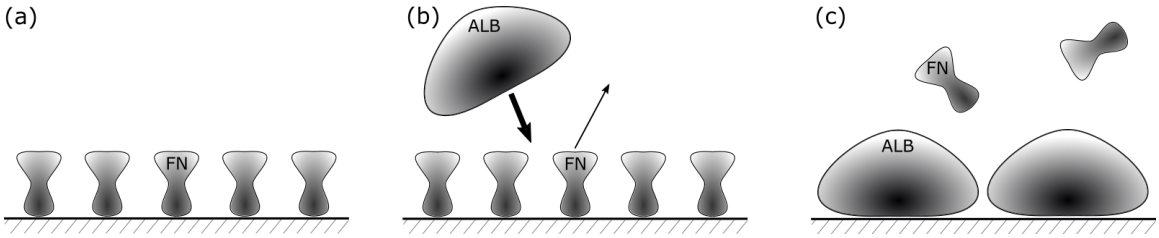

FIGURE 21. Protein adsorption at an interface.
(a) The ECM protein, fibronectin (FN), is coated on the substrate prior to cell plating in order to improve neuron adhesion and outgrowth. (b) Next, neurons are placed onto the surface in cell culture medium. The medium contains large hydrophobic serum proteins, such as albumin (ALB). (c) Depending on the surface's hydrophobicity, the albumin will displace the fibronectin due to a larger surface binding affinity.

In traditional neuron cultures, neuron adhesion, proliferation (i.e. cell division), and neurite outgrowth are measured in response to some independent variable. These independent variables include biological ones such as (i) neuron cell type, (ii) length of culture, (iii) age of animals, or (iv) presence of glia and chemical ones such as (v) type of ECM protein surface coating, (vi) ECM protein concentration, (vii) pH

of adsorbed protein, (viii) exposed surface functional groups, and (ix) cross-linking molecules. This paragraph lists examples of experiments specifically related to the retina investigating these above variables. In 1981 Akers et al. showed neurite outgrowth from retinal cell aggregates was greater on functionalized fibronectin surfaces than untreated plastic and glass [82]. Substrates pretreated with poly-L-lysine showed a minimal outgrowth extending 25-50 μm while those with fibronectin extended up to 1 mm. Additionally, they showed maximal outgrowth occurs when fibronectin is absorbed at a pH between 6 and 6.5 and that outgrowth saturates for a fibronectin incubation concentration of 25 μg/mL. Grinnel and Feld (1982) showed that cell spreading area is greater for fibronectin adsorbed onto hydrophilic versus hydrophobic surfaces [83]. In another study, retinal explants were placed onto substrates fuctionalized with collagen, fibronectin, or laminin [84]. Retinal ganglion axon outgrowth was greatest for substrates treated with laminin. Age of animals also influences neurite outgrowth. For example, rat embyronic retinal cells were cultured on substrates coated with poly-L-lysine and laminin for different embryonic ages. There were approximately 8 times more process bearing cells for E6 (embryonic 6 days) versus E11 on laminin coated substrate. Cultures on poly-L-lysine showed very few process growing cells for both E6 and E11 [85]. Different neuron types within the retina also respond differently to substrate coatings. For instance, neurite outgrowth from rods is minimal on substrates coated with laminin, fibronectin, or collagen. However, rods cultured on Müller cells, a subtype of glia, showed extensive outgrowth [86]. The pH at which proteins are absorbed onto the surface also affects neuron cultures. Using radiolabeled laminin, Freire et al. (2002) imaged self-assembled laminin matrices on glass substrates absorbed at different pH's [87]. Acidic pH resulted in a dense two dimensional morphology while neutral pH gave a sparse three

dimensional morphology. Rat cerebral cortex neurons (E14) were then cultured on the two substrates. The dense two dimensional laminin matrix resulted in large neurite outgrowth and few cell clusters while the sparse three dimensional matrix promoted cluster formation due to cell division.

In order to improve the neuron adhesion and neurite outgrowth, ECM proteins can be more strongly bound to the surface through a process termed covalent conjugation. Covalent conjugation is a process which strongly binds ECM proteins to the surface through covalently linked cross-linker molecules. The process includes three steps. First, surface functional groups, such as OH^- or COO^-, are created at the surface through chemical modification. Next, the substrate is immersed into a solution which contains a cross-linker molecule. These molecules may, for example, bind to a surface OH^- group on one end and leave an open NH^+_2 group on the other end (Fig. 22a). Finally, the substrate is immersed in a solution containing the ECM proteins (Fig. 22b). In theory, covalent conjugation is preferred over adsorption because the ECM proteins remain attached to the surface throughout the cell culture [88]. For instance, Kuddannaya et al. (2015) showed increased neurite outgrowth on covalently conjugated poly-L-lysine, laminin, fibronectin, and collagen on a PDMS

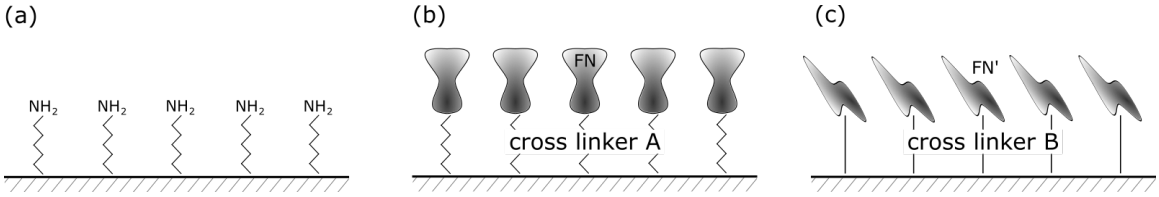

FIGURE 22. Protein covalent conjugation at an interface.
(a) Cross-linker molecules bind to exposed surface functional groups at one end and leave an open NH^+_2 functional group at the other. (b) FN proteins covalently bind to the cross-linker A with a strong binding affinity. (c) Depending on the cross-linker though, in this case cross-linker B, the confromational shape of the FN may be altered resulting in FN' which can adversely affect neuron adhesion.

substrate as compared to each respective adsorbed protein [89]. However, depending on the cross-linker molecule, the conformational shape of the ECM protein can be changed [90], resulting in the integrin binding site no longer being accessible (Fig. 22c). For instance, Valliéres et al. (2007) showed cell spreading area (of a non-neuron type cell) on covalently linked fibronectin is heavily dependent on the cross-linker molecule [91].

In addition to functionalizing an entire surface, patterns of biological molecules, typically stripes or grids, can be transferred onto substrates to create biophilic and bio-repellant domains. These separate domains allow researchers to direct axon growth, define geometrically simple neural networks, and/or seed cells above electrode sites [81] [92]. A wide variety of techniques are used to pattern bioactive molecules onto substrates. Perhaps the most popular method is micro-contact printing (μCP). μCP is a form of imprint printing in which a stamp (typically PDMS) is dipped into a solution with bioactive molecules and then stamped onto the surface. Binding affinity of biological molecules must be greater on the final surface than the stamp for the

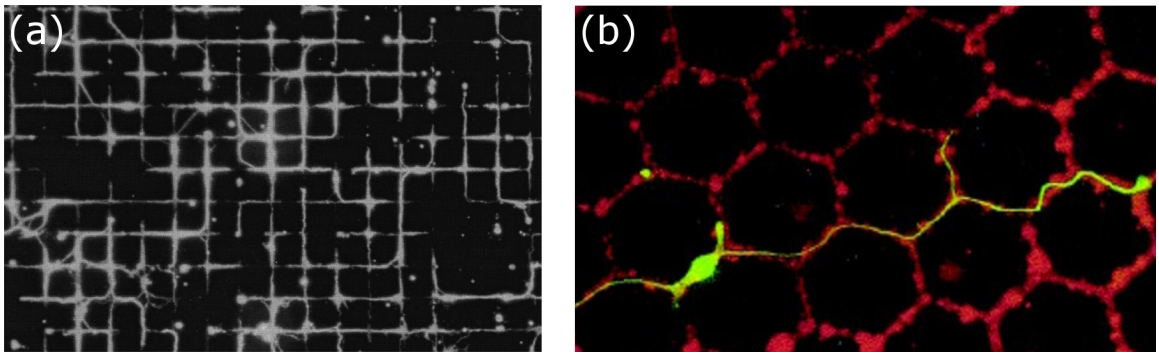

FIGURE 23. Neurite outgrowth on micro-contact printed patterns. (a) Hippocampal neuron somas adhere strongly to the crosspoints of an underlying grid of CAMs and then send processes along the grid directions. Image from Scholl et al., 2000. (b) A hippocampal axon (green) is capable of bending in order to follow a hexagonal μCP polylysine conjugated laminin chemical surface (red). Image from Kam et al., 2001.

molecules to transfer during the stamping process. For example, 90% of hippocampal neurons could be aligned onto square lattice with 5 μm line width and 50 μm pitch (Fig. 23a) [93]. Hippocampal neurons have also been aligned directly above gold electrodes [94]. Axonal outgrowth of at least 150 μm extensively followed polylysine conjugated laminin hexagonal lattices of line width 2.6 μm and side length 43 μm (Fig. 23b) [95]. In a more recent study, axonal orientation showed a preference for the sharpest vertex of micropolygons formed from μCP polylysine conjugated laminin [96]. Protein concentration gradients affect neurite differentiation into a primary axon and in which direction the axon grows [97]. Using laminar flows in microchannels, varying protein gradients of laminin and albumin were immobilized onto a substrate. Rat neonatal hippocampal cells were then cultured on the protein gradient surface. After 24 hours, the longest process grew in the direction of the laminin gradient provided the gradient was greater than 0.06 μg(mLμm)$^{-1}$. For a nice comprehensive overview of the vast number of biological molecule patterning methods, see [98].

In summary, neural adhesion, proliferation, and neurite outgrowth are influenced by a wide range of variables including: (i) neuronal cell type, (ii) age of animals, (iii) length of culture, (iv) type of ECM protein or CAM, (v) presence of glia, (vi) surface hydrophobicity, (vii) ECM protein adsorption versus covalent conjugation, (viii) ECM protein concentration, (ix), pH of protein adsorption, (x) exposed surface functional groups, (xi) cross-linking molecules, (x) geometry of biological molecule patterning, and (xi) ECM protein gradients. In addition, protein adsorption is also influenced by topography [99], which combinatorially affects the variables just listed.

Topography

Neuron adhesion and outgrowth are also influenced by substrate topography. For instance, Rajnicek et al. (1997) cultured Xenopus spinal neurons and rat hippocampal neurons on parallel microgrooved quartz substrates with groove depths varying between 14 - 1100 nm and line spacings of 1 - 4 μm [100]. Xenopus spinal neurites grew parallel to grooves for all depths and line spacings. However, rat hippocampal neurites grew perpendicular to narrow shallow grooves but parallel to wide deep grooves. Neurites also turned sharply to grow in their preferred growth direction when growing from a flat region onto the grooved region (Fig. 24). Neurites also emerged from the soma and elongated faster along the preferred growth direction. Finally, they noted that the preferred direction for rat hippocampal cells changed depending on the embryonic age of the rat. Neurite orientation and morphology is also affected by large channels with heights of 11 μm and widths varying from 20 - 60 μm [101]. In narrow channels, 20 - 30 μm, neurites oriented parallel to the channel walls and exhibited reduced complexity. In wider channels, the neurite orientation and morphology depends on the distance of the cell body to the channnel wall. Cell

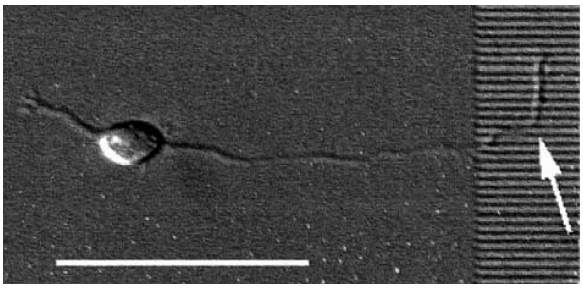

FIGURE 24. Neurites turn to grow perpendicular to narrow shallow grooves. Rat hippocampal neurites prefer to grow perpendicular to narrow shallow grooves but parallel to wide deep grooves. Image from Rajnicek et al. (1998).

bodies which landed far from a channel wall exhibited a greater complexity and more perpendicular neurites than from those which began close to a channel wall. Rat hippocampal cells cultured on poly-L-lysine coated etched silicon micropillar arrays showed an orientation preference and increased neurite lengths [102]. Pillars were $1\,\mu$m tall, varying between 0.5 - $2\,\mu$m in width, and varying between 0.5 - $5\,\mu$m in gap size. An entropy measurement was used to quantify the frequency of neurites changing directions. In particular, pillar widths of $2\,\mu$m and gaps of $1.5\,\mu$m resulted in significantly longer neurite lengths and significantly lower entropy. Substrate curvature has also been shown to influence the direction of neurite outgrowth [103]. In this experiment, dorsal root ganlia were cultured on cylindrical surfaces with varying radii between 30 - $500\,\mu$m. By measuring neurite orientation with respect to the long axis of the cylinder, the authors were able to show that neurite orientation follows a Boltzmann distribution, $p \propto e^{-E/kT}$, where the energy is just the bending energy of a thin flexible rod (Euler beam energy). The neurite bending stiffness was measured to be $6.45 \times 10^{-28}\,\mathrm{Nm}^2 \pm 7.9\%$.

Neurons respond not only to micron-sized topographies, but also to nano-sized topography. Recently, there has been growing interest in using nanoscale roughness to promote neuron adhesion. Wet etching is typically employed to achieve nanoscale roughness. For example, neuron adhesion and outgrowth on etched silicon is maximal for rms surface roughness between 20 - 70 nm [104] [105]. However, this size scale does not ubiquitously improve adhesion. The percentage of adhering neurons to nanorough gold continuously decreased as surface roughness was increased from 0.5 - 100 nm [106]. The authors hypothesized that the nanorough surfaces change ECM protein adsorption onto the surface. While this may [107] or may not [108] be the case, a nice alternative explanation was later provided by Gentile et al. (2013). In

this experiment, fibroblast adhesion and proliferation on silicon surfaces with varying surface roughness and fractal dimension was investigated [109]. Here the fractal dimension, D_f, quantifies the frequency with which peaks repeat over multiple size scales. Moderate roughness (∼40 nm) and moderate fractal dimension ($D_f \sim 2.4$) maximized proliferation while cell spreading area was maximized for higher roughness (∼50 nm) and lower fractal dimension ($D_f \sim 2.2$). The authors hypothesized that the sharp peaks that occur in high D_f substrates prevent the formation of large stable focal adhesion sites, thus resulting in reduced adhesion.

Nanotubes and nanofibers are receiving a lot of attention as biomaterials for neuron growth due to their similarity to the natural ECM. For instance, a fibrous scaffold of polymer fibers can be produced by electrospinning [110]. In this experiment, Yang et al. cultured neural stem cells on microfibers and nanofibers with random or aligned orientation. Nearly always, neurite orientation aligned parallel to both aligned nano and micro fibers. Cell differention was independent of fiber alignment, but the differention rate was twice as high on nanofibers. Mean neurite length was also slightly longer for aligned nanofibers. In another study it was shown that applying an electric field of 10 mV/cm to electrospun fibers coated with an organic conducting polymer increased neurite length by 40%-50% and number of neurite bearing cells by 40%-90% [111]. Electric fields applied to aligned nanofibers increased neurite length and number of neurites slightly over random fibers.

More recent nanomaterials which have emerged in the previous ten years as potential neural interfaces include carbon nanotubes, single layer graphene, nanopillars, silicon nanowires, and III-V nanowires. In particular, our group focuses on carbon nanotube (CNT) electrodes. As such, an in-depth review on CNTs is provided later in this section. Single layer graphene field effect transistors are a

flexible semiconducting material capable of extracellularly recording cellular spiking activity with a signal-to-noise ratio of at least 4 [112]. Approximately 80% of adult retinal ganglion cells cultured on non-coated single layer graphene could survive for 6 days in culture [113]. The mean total neurite extension was $\sim$700 μm on non-coated graphene and $\sim$1000 μm on coated graphene. Even though single layer graphene is modestly biocompatible, survivability and neurite outgrowth was greater on glass substrates. Neurons form strong focal adhesions to nanopillars capable of effectively pinning cultured neurons in place [114]. Embryonic cortical neurons were cultured on SiO_2 nanopillars 150 nm in diameter and 1 μm tall. After 5 days in culture, the average neuron's migration distance was reduced from $\sim$60 μm on flat Si to $\sim$4 μm on nanopillar substrates. Vertical silicon nanowires can penetrate the cell membrane and stimulate and record neural activity with a signal-to-noise ratio greater than 100 [115]. A nice review on cells interfacing with semiconducting nanowires is provided by Prinz [116]. For a very comprehensive up-to-date review on modern nanobiomaterials for neural interfacing, see [117].

Chemistry or topography? Which is the dominant surface cue in determing neural growth? Topography can affect adsorption of chemicals and vice-a-versa. So, typically, this question is very hard to answer. One experiment attempted to answer this question by seeding embryonic (E18) hippocampal neurons directly between PDMS microchannels and immobolized neural growth factor [118]. Microchannels were 1 or 2 μm wide and 400 nm deep. In the presence of solely topographical cues or chemical cues, hippocampal axons preferentially grow from a flat area onto the patterned stripes or neural growth factor, respectively. When placed directly between competing topographical and chemical cues, hippocampal axons preferentially grew

onto the striped pattern 70% of the time (Fig. 25), indicating the elongating axons prefer topographical cues.

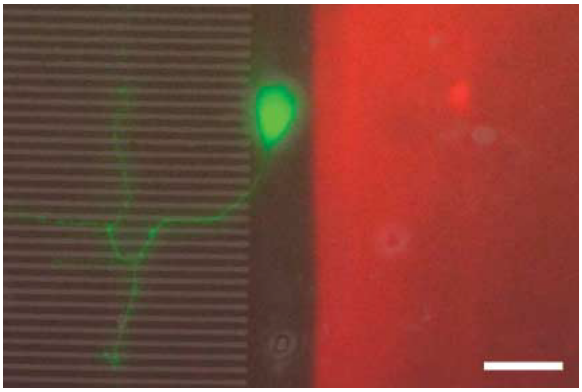

FIGURE 25. Axons prefer topographical over chemical surface cues. Hippocampal neurons placed between PDMS microchannels and neural growth factor preferentially grow axons towards the topographical surface cues. Image from Gomez et al. (2007).

Substrate elasticity

In addition to chemistry and topography, neurons respond to a substrate's mechanical stiffness. For example, Balgude et al. (2001) cultured dorsal root ganglion neurons on agragose gels with mechanical stiffness varying between $\sim$ 3 - 130 Pa [119]. The neurite elongation rate was inversely correlated with mechanical stiffness. Using time lapse microscopy, they measured a mean neurite elongation rate of $\sim$15 μm/h on gels with a 3 Pa mechanical stiffness. Elongation rate approached a constant value of $\sim$8 μm/h for stiffness greater than 70 Pa. In a similar experiment, embryonic mouse spinal cord neurons were cultured on protein laminated polyacrylamide gels with stiffnesses between 50 - 550 Pa [120]. Neurons formed more than three times as many branch points on $\sim$300 Pa or less stiffness gels as compared to 550 Pa gels. Interestingly, no glia cells survived on the gels after several weeks in culture. Under

identical culture conditions except on glass, glia cells typically dominate a culture after several weeks because they continuously divide. Neurite outgrowth can also be directed by substrate elasticity gradients [121]. Uniform gradients were created by filling a microfluidic channel with collagen, and then placing a crosslinking reagent in only one port. Dorsal root ganglion neurites grew in the direction of stiffness gradients of at least $0.064\,\mathrm{Pa}/\mu\mathrm{m}$.

Electric fields

Applying an electric fields to neurons in culture can enhance and/or direct neurite outgrowth. For instance, Schmidt et al. (1997) cultured the neuron cell line PC-12 on the conducting polymer, polypyrrole (PP). After 24 h in vitro, a 100 mV potential was applied to the PP substrate (ground located on other side of culture well) for 2h followed by 24 hours more in culture. Mean neurite length increased from $9.5\,\mu$m to $18.1\,\mu$m for neurons grown on the substrate receiving the 100 mV potential [122]. In another experiment, snail neurons were cultured on 4 different substrates and a constant electric field was applied throughout the solution for 8 h to 12 h [123]. Neurites grew preferentially down the field gradient (i.e., toward the cathode) on negatively charged plastic, laminin coated substrates, or poly-L-lysine + laminin substrates. In the case of substrates coated only with poly-L-lysine though (positively charged substrate), neurons grew up the field gradient (i.e. toward the anode). The authors hypothesized accumulation of positive proteins on the negatively charged surfaces at the cathodal end caused neurites to grow in that direction.

Interfacing Neurons with Carbon Nanotubes

Carbon nanotubes (CNTs) are an ideal material candidate for neural interaces. They are highly conductive and flexible. They can be functionalized to improve neuron adhesion and outgrowth. On the micron scale, they can be patterned for contact guidance. At the nano scale, they offer a topographical surface which mimics the neuron's natural ECM environment. They have a high tensile strength, but thin aspect ratio, so they are deformable by extending growth cones. Additionally, neuron membranes are capable of wrapping around CNTs providing a strong adhesive point. In the context of neural electrical devices, carbon nanotube electrodes can be broadly classified into either quasi-flat CNT 'mats' (Fig. 26a) or vertically aligned CNTs 'forests' (VACNTs) (Fig. 26b). Depending on the preparation method, the morphologies may look different than those shown. Below is a brief summary of CNT

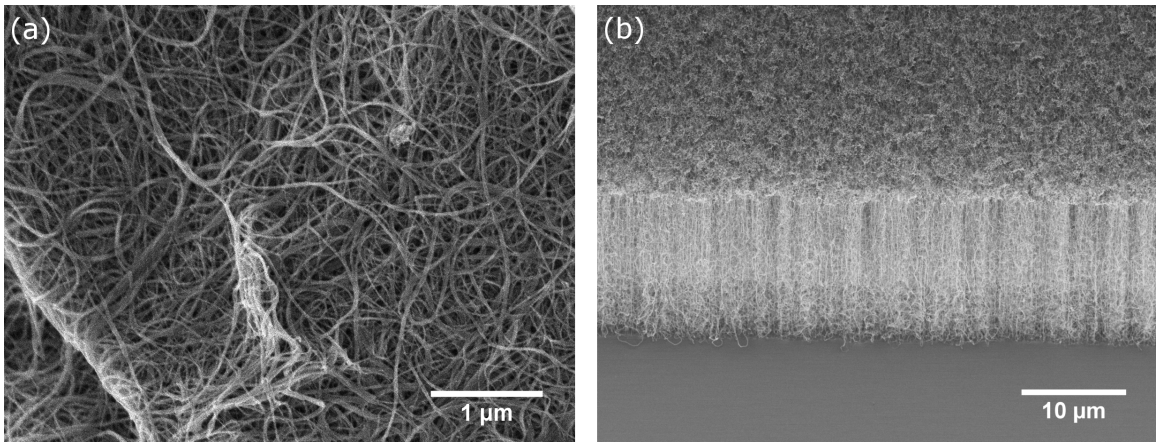

FIGURE 26. Quasi-flat CNT mats and vertically aligned CNT forests
(a) Quasi-flat CNT mats form a tangled bundle on the substrate with the majority of the area being exposed CNT sidewall area (image shown top-down) (b) VACNTs orient perpendicularly from the substrate with the top surface containing many CNT tips (image shown at 30°).

properties relevant to neural electrical devices. Neural adhesion experiments on CNT mats and VACNTs are summarized in Tables 2 and 3, respectively. Experiments investigating CNTs as an electrode material for stimulating and recording neural implants are summarized in Table 4.

CNT mats

CNT mats are typically prepared by sonication of dry CNTs in a solvent followed by dispersing the CNT solution onto a substrate and rinsing. For CNT mats greater than a few monolayers, the typical rms surface roughness is in the range of 5-40 nm [124] [125] [126], the elastic modulus is 1-10 GPa [127] [128], and the resistivity is $\sim 1 \times 10^{-4}\,\Omega$cm for films greater than $\sim$10 nm thick [129] [130].

Functionalization of quasi-flat solution deposited CNT surfaces improves neuronal biocompatibility as compared to non-functionalized CNTs. For example, in the first investigation of the biocompatibility of CNTs, Mattson et al. (2000) showed neurons could adhere to and extend neurites on non-functionalized multiwall carbon nanotube (MWCNT) surfaces [131]. However, sidewall functionalization through physioadsorption of the bioactive molecule, 4-hydroxynonenal, greatly increased the total neurite length, number of neurites per cell, and number of branches per neurite.

Hu et al. (2004) further explored CNT surface functionalization by attaching different functional groups to vary the surface charge [132]. Non-functionalized, negatively charged, zwitterionic (featuring both positive and negative domains), and positively charged nanotube surfaces were compared to a control polyethylenimine (PEI) coated glass surface. Neurite outgrowth and branching occurred on non-functionalized CNT mats, but the extent was significantly less than the control. Average neurite length, number of growth cones, and neurite branching all increased

going from negative to zwitterionic to positive charged functionalizations, although neither functionalization was as extensive as the PEI control surface. A follow up study found composite single wall carbon nanotube (SWCNT) - PEI polymer surfaces enable neurite outgrowth and branching intermediate to non-functionalized CNTs and PEI control surfaces [133]. Other functionalizations which have been shown to increase neurite outgrowth on CNT mats include poly-ethylene glycol [134], carboxylic and hydroxide groups [135], and covalently bound neurotrophins [136]. Lovat et al. (2005) cultured hippocampal neurons on glass and non-functionalized multi-walled carbon nanotube (MWCNT) surfaces [137]. There was no discernible difference in neurite adhesion or outgrowth between the two surfaces. However, connected neurons had six times as many spontaneous post synaptic currents on CNT surfaces as compared to glass.

Lovat's et al. 2005 observation of increased spontaneous synaptic activity for neurons grown on CNTs led to a set of follow up experiments investigating the nature of neuron-nanotube electrical connections. Mazzatenta et al. (2007) directly stimulated hippocampal neurons through a SWCNT substrate and developed a mathematical model proposing resistive coupling between the neuron membrane and nanotubes suggesting a tight membrane-CNT connection [138]. Cellot et al. (2009) found evidence for an 'electrotonic hypothesis'; nanotube surfaces directly effect neuron depolarization by providing an electrical shortcut between distal dendrites (far from the soma) and the soma [139]. Hippocampal neurons cultured on SWCNT substrates were given a current pulse so that six back-to-back action potentials were initiated. After the spike train, there was a large after-depolarization potential associated with indirect Ca^{2+} electrogenesis from back-propogating action potentials (action potentials which travel from the axon to the soma). After depolarization

potentials were significantly less for flat conductive surfaces or nanorough non-conductive surfaces. TEM analysis showed neurons formed tight synaptic connections with the nanotubes. Tight synaptic-CNT connections combined with high nanotube conductance give rise to an overall lower impedance in which distal dendritic depolarization takes an electrical shortcut through the CNT surface back to the soma to effectively act as a proximal (near to the soma) dendrite. Nanotube-PEG composite surfaces with varying conductance (achieved by varying nanotube-PEG film thickness), but equivalent surface roughness also modulate neurite outgrowth [140]. In particular, neurite outgrowth is maximal on intermediate conductivities of 0.3 S/cm and decreases with increasing substrate conductivity.

Quasi-flat CNT mats are also capable of directing neurite growth [141]. Rows of CNTs were prepared on glass substrates and the whole surface coated in the cell adhesive molecule, poly-L-lysine (PLL). CNT rows were tens of nanometers thick with ∼3 nm RMS roughness. PLL adsorption was greater on CNT rows than glass. Seeded neuron somas did not show a preference for adhering to CNT-PLL areas versus PLL areas nor was there any preference for neurite alignment up to two days in vitro. However, by four days in vitro, neurites aligned with the CNT-PLL pattern and extended ∼3x longer. Beduer et al. (2012) cultured a neuroblastoma cell line (neuroblastoma differentiate into cells which have many neuron like properties) on double walled nanotube (DWNT) lines 7-20 μm in width and 10-100 nm tall which turned once at a 90° corner [142]. Immediately after cell seeding there was no discernible difference in cell density between the double walled carbon nanotube (DWNT) or underlying SiO_2 surface. But, by one day in vitro, the majority of cells migrated to the DWNT rows, extended more neurites than those cells on SiO_2 areas and grew neurites which followed the 90° corner.

Vertical CNTs

Carbon nanotube topography, both at the nano and micron scale, strongly influences cell adhesion and neurite growth. Zhang et al. (2005) investigated neuron adhesion and growth on patterned vertical CNT forests on silicon substrates [143]. The entire surface was functionalized with PLL. For the CNT areas, functionalization occurs through adsorption at the CNT sidewall. First, neurite outgrowth was not preferred over a silicon substrate when the CNT height was only 500 nm. But, at $10\,\mu$m CNT height, neurites preferred the CNT surface, and in particular grew along CNT edges. They attributed the lack of neurite growth on 500 nm tubes to pinning of the neuron's growth cone. Neurite guidance was also observed on straight and curved CNT lines. Additionally, they observed growth cones wrapping around carbon nanotubes and deforming them.

A quick calculation gives a theoretical reason why neurites get pinned on 500 nm nanotubes but not $10\,\mu$m tall nanotubes. For the growth cone to grow, it must be able to deflect the CNTs it's attached to by a distance, d. Where d is the CNT interspace interval. Euler beam theory for a cantilever gives the deflection distance, w, as

$$w = \frac{\frac{F}{N} L^3}{1.5\pi E a^4} \tag{1.33}$$

where L is the CNT length, $E = 1$ TPa Young's modulus for CNT's, a the CNT radius, and N the number of CNT-growth cone contacts. For example, assuming $N = 100$, $a = 10$ nm, and $w = d = 50$ nm, and $F = 5 \times 10^{-9}$ N [144], then $L > 3.5\,\mu$m. This falls between the limits determined by Zhang et al. (2005).

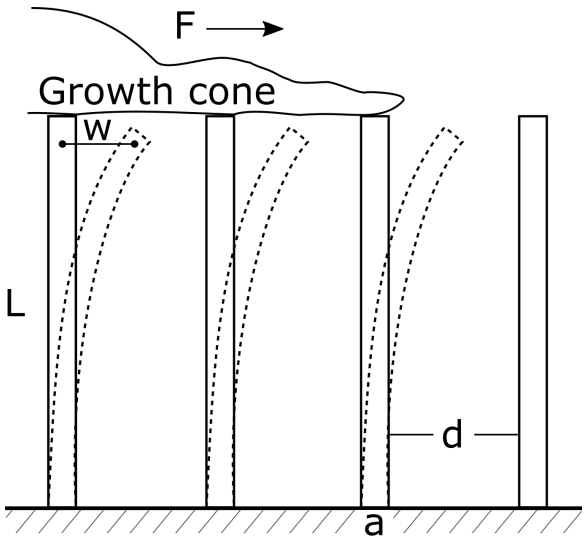

FIGURE 27. Model for growth cone on carbon nanotubes.
Each nanotube has a height, L, a radius a, and is separted by a distance, d, from its neighboring nanotube. The growth cone generates a force F when extending which causes nanotube to bend by a distance w at the top surface.

Functionalization of vertical CNTs can improve neurite outgrowth. For instance, in one experiment 1.5 μm tall sparse vertical CNTs were chemically treated with 6 different functionalizations – nonfunctionalized, 3 by adsorption, and 2 by covalent conjugation [145]. Of all the functionalizations, plasma treatment resulted in the greatest number of neurites and neurite length at both 3 DIV and 8 DIV. Cell clustering was observed at 8 DIV for nonfunctionalized and adsorption functionalized CNTs, indicating the neurons were not strongly bound to the underlying CNT surface. Covalently attached plasma with PEG_{5000} (an adhesion blocker) gave no outgrowth. In an experiment exploring fibroblasts (a connective tissue cell) Machado et al. (2015) explored plasma functionalization of CNTs grown from either Fe or Ni catalysts. The CNTs grown from Fe catalyst resulted in a dense forest like structure, while CNTs grown from island are sparser and more free-standing [146]. From their experiment,

they found fibroblast adhesion was greatest on plasma functionalized CNTs grown from Fe catalyst.

The mechanism by which neurons adhere to CNTs was studied in depth by Sorkin et al. (2009) [147]. Pristine CNT islands 20-80 μm in diameter were prepared on quartz substrates and seeded with either rat cortical neurons and glia or locust ganglion neurons. Insect neurons are larger and provide another length scale to study the neuron-CNT interaction. They found neurite outgrowth on CNT islands was distinctly curly, neurites extended preferentially at the CNT island edges, and glia adhered to and grew processes on the CNTs. Insect neurites with larger diameters (4 μm as compared to 1 μm) did not interact and curl on the CNT islands, but rather grew bundles together. The authors concluded the surface roughness is size selective to neurite diameter to allow for surface binding.

Another experiment investigated neural adhesion and outgrowth on vertically aligned carbon nanofibers [148]. In contrast to multiwall carbon nanotubes that have a diameter of ∼10-30 nm, carbon nanofibers have a diameter of ∼150 nm. Two varying topographies were studied; one with free standing nanofibers and one with collapsed bundles. In each case the surface was functionalized with collagen. Neural cell line PC-12 cells extended neurites over both free-standing and collapsed bundle carbon nanofibers although the free-standing interface allowed for a stronger mechanical contact between neurons and fibers including many observed instances of the neuron membrane wrapped around individual fibers. The topography can also be altered using different catalyst materials necessary for growth of vertically aligned carbon nanotubes. Machado et al. (2015) cultured embryonic fibroblasts on CNT forests grown from either iron or nickel catalysts and either pristine or plasma functionalized [146]. Although the surfaces grown from the two catalysts had

substantially different topographies, adhesion was similar between the two conditions. Adhesion did increase with plasma treatment.

Vertical carbon nanotubes are also a promising platform for neural network formation in vitro. For instance, Gabay et al. (2005) cultured cortical neurons in the presence of hydrophobic CNT 100 μm islands spaced 150 μm apart on hydrophilic SiO_2 or quartz [149]. Neurons initially dispersed isotropocally across the surface. By four days in vitro neurons migrated to CNT islands and formed axon bridges between neighboring islands. Similar results have since been repeated [150] [151].

Carbon Nanotube Electrodes

Carbon nanotube electrodes are an extremely effective neural interface material due to: (1) high conductivity, (2) flexibility, (3) a high aspect ratio which allows for tissue penetration and closer proximity to cells, (4) a textured topography important for neural adhesion, and (5) their large capacitance, which results from the extreme nanotexture creating a large effective surface area. Wang et al. (2006) first showed the promising applicability of vertically aligned (VACNT) electrodes for in vitro stimulation of hippocampal tissue [152]. Electrode sites were 30-50 μm in size and 40 μm tall with a measured charge injection limit of 1-1.6 mC/cm^2. Using cell spiking calcium indicators, they measured induced stimulation of hippocampal neurons for threshold currents of 10-20 μA and 1 ms cathodic pulses.

Carbon nanotube recording electrodes are equally as promising. Gabay et al. (2007) created a multielectrode array (MEA) with 80 μm VACNT electrodes and a measured specific capacitance of 10 mF/cm^2 [70]. Cortical neurons and glia were then cultured on the MEA in standard cell culturing conditions for up to 14 DIV. The recorded SNR ratio was as high as 135, surpassing the SNR of typical capacitive

type electrodes ∼5 fold [153]. This vast improvement was ascribed to a tight neural-electrical coupling and low electrode impedance. Tight neuron-electrode coupling was reaffirmed for cultured rat hippocampal neurons on quasi-flat single walled carbon nanotube mats [138]. Patch clamp recordings were used to demonstrate that action potentials can be elicited through the SWCNT electrode. SWCNT coatings of platinum electrodes can also be used to improve the SNR for recording electrodes [154], although the reduction in SNR was not nearly as effective as the vertically grown CNT electrodes presented by Gabay et al. (2007).

In 2009, Lin et al. realized the utility of a flexible device by embedding CNT electrodes into a flexible parylene-C film [155]. The flexible CNT device was capable of extracellularly recording action potentials from crayfish nerve cord with a SNR ∼3 times greater than the conventional reference electrode. A MEA with CNTs embedded in a thin polyimide film was used to obtain in vivo, electrocortigram, recordings with an improved SNR [156]. Another application utilized the high flexibility of CNTs to create an implantable electrode with a Young's modulus of 2.4 kPa, which is below the critical rupture strength for the brain of 3 kPa [56]. In contrast, conventional electrodes have a Young's modulus approximately 5 orders of magnitude higher than the brain, potentially leading to glia scar formation. CNT electrodes were embedded in parylene and had electrode sizes of 10-50 μm with charge injection limits of ∼1.5-2.5 $\mathrm{mC/cm^2}$. In vivo recordings identified low-frequency neural signals but failed to detect action potentials. Another application using all CNT electrodes embedded in biocompatible thin films (parylene, PDMS, polyimide, medical adhesive tape) recorded spiking activity in vitro from chick retinas [74]. CNTs were encapsulated between medical tape and a 150 μm thick polyimide layer with 50 μm holes exposing the CNT electrode sites to the tissue. The stimulating

threshold was a 4 μA pulse with 1 ms duration and spiking activity could be recorded although the magnitude was small due to the polyimide encapsulation layer. This large separation was overcome by Yi et al. (2015) who prepared a flexible CNT device with recording sites which extended past the encapsulation layer. [157].

Exposure of CNTs to oxygen plasma creates -OH groups at the surface which increase surface wettability and decreases electrode impedance [158]. MEAs with CNT recording sites of 2500 μm^2 had a specific capacitance of 0.54-2.25 mF/cm^2 and improved the SNR ratio of recorded spiking activity from crayfish neurons by 60% as compared to pristine CNTs. PEDOT/CNT composite structures have also been used to increase the charge injection limit to 2.5 mC/cm^2, increase the mechanical stability of PEDOT coatings, and provide a biocompatible interface [73].

CNT surface	**Functionalization**	**Cell Type**	**Observations**	**Reference**
Quasi-flat MWCNTs	· Pristine · 4-HNE	Rat (E18) hippocampal neurons	Neurons extend neurites on pristine MWCNTs. 4-HNE functionalization increased neurite length, number neurites per cell, and number branches per neurite	Mattson et al. (2000)
Quasi-flat MWCNT	· COOH · PABS · EN	Rat (P0-P2) hippocampal neurons	Neurite outgrowth less on PEI coated glass than pristine MWCNTs. Neurite length, number neurites, and number branches per neurite increases from negative to positive functionalizations.	Hu et al. (2004)
Quasi-flat SWCNT	· PEI	Rat (P0-P2) hippocampal neurons	Neurite outgrowth and number of branches intermediate to pristine MWCNTs and PEI coated glass	Hu et al. (2005)
Quasi-flat MWCNT mats	· COOH and OH	Rat (P1) DRG neurons	Neurite outgrowth greater on functionalized versus pristine CNT mats	Xie et al. (2006)
Quasi-flat MWCNTs	Covalently bound neurotrophin	Chick (P8) DRG neurons	Neurite outgrowth on CNTs bound with neurotrophin similar to outgrowth on glass in the presence of neurotrophin dissolved in the culture medium	Matsumoto et al. (2007)
Quasi-flat MWCNT	Nonfunctionalized	Hippocampal neurons	Neurite outgrowth and adhesion similar between MWCNT surfaces and glass. Increased spontaneous postsynaptic currents on MWCNT substrate.	Lovat et al. (2005)
Quasi-flat aligned CNT sheets and yarns	Pristine	Mouse cortical, cerebral, and DRG neurons	Multiple neuronal type adhesion and outgrowth. Neurite morphology and outgrowth similar to control functionalized glass surface.	Galvin-Garcia et al. (2007)
CNT rows on quartz	OTS and PLL	Rat (E18) hippocampal neurons	Neurites extend preferentially on CNT-PLL rows.	Jang et al. (2010)

TABLE 2. Summary of in vitro experiments investigating neuron growth on CNT films.

CNT surface	**Functionalization**	**Cell Type**	**Observations**	**Reference**
Patterned vertically aligned CNTs	PLL	H19-7 cell line	Neurite outgrowth similar between 500 nm tall CNTs and glass. Neurites followed CNT patterns and preferred growing along pattern edges.	Zhang et al. (2005)
Vertical CNT islands on silicon or quartz	Pristine	Rat P1 cortical neurons	Neurons migrate to CNT islands by 4 DIV and form a neural network with axon bridging between CNT islands	Gabay et al. (2005)
Freestanding and collapsed carbon nanofibers	Collagen	PC12 neural cell line	Neurite adhesion on both surfaces although a closer interface for freestanding nanofibers	Nguyen-Vu et al. (2007)
Vertical CNT islands on quartz	Nonfunctionalized	· Rat cortical neurons and glia · Locust ganglia	Cortical neuron processes curl on CNT areas and preferentially extend on island edges. CNTs support glia growth. Morphology of thicker diameter insect neurites is independent of CNTs.	Sorkin et al. (2009)
Sparse vertical CNTs	· Nonfunctionalized · 3 different adsorption functionalizations · Plasma · Plasma-PEG_{5000}	Rat E19 hippocampal neurons	Neurite outgrowth greatest on plasma treated CNTs at both 3 DIV and 8 DIV. Cell clustering was observed at 8 DIV for nonfunctionalized and adsorption functionalized CNTs. PEG_{5000} gave no outgrowth.	Liu et al. (2011)

TABLE 3. Summary of in vitro experiments investigating neuron growth on VACNTs.

Electrode Device	**Application**	**Electrode Size**	**Capacitance (mF/cm^2)**	**SNR**	**Reference**
· Hydrophobic VACNT MEA · Hydrophilic VACNT MEA	In vitro stimulation cultured hippocampal tissue	30-50 μm wide 40 μm tall	· 0.0054 · 1.6	—	Wang et al. (2006)
VACNT MEA on TiN contacts	In vitro recording cultured cortical tissue	80 μm wide 40 μm tall	10	135	Gabay et al. (2007)
Solution deposited SWCNTs on Pt contacts	In vitro recording retinal explant	40 μm diameter	45.9×10^{-6}	∼8	Gabriel et al. (2009)
Flexible CNT electrode encapsulated in parylene and PDMS	In vitro stimulation and recording crayfish nerve cord	25 μm diameter	11.8	257	Lin et al. (2009)
· As grown VACNT MEA · Plasma treated CNT MEA	In vitro stimulation and recording crayfish nerve cord	2500 μm^2	· 0.54 · 2.25	40	Chen et al. (2010)
Hydrophilic CNTs on flexible polyimide substrate	·In vitro recording crayfish nerve cord ·In vivo mouse electrocortigram recording	100 μm diameter 1.5 μm tall	0.21	·6.2 ·8.68	Chen et al. (2011)
Single CNT site encapsulated in parylene on flexible shaft	In vivo cortical recordings	10, 25, and 50 μm	∼0.15		Zhang et al. (2013)
Flexible CNT MEA	In vitro recording and stimulation of retina	100-450 μm	1-10	20	David-Pur et al. (2014)
CNT MEA encapsulated in parylene	In vivo stimulation and recording rat spinel nerve	4800 μm^2 area 2 μm tall	18.75	12.5	Yi et al. (2015)
Plasma treated VACNT MEA	In vitro recording and stimulation of retina	900-10 000 μm^2 2 μm tall	—	∼20	Eleftheriou et al. (2017)

TABLE 4. Summary of CNT electrodes interfacing with neural tissue.

Fractals

The term fractal was coined by Benoit Mandelbrot to describe self-similar objects in both mathematics and nature [159], where self-similar refers to being able to zoom in on a pattern and see that same pattern repeat at increasingly small size scales. In mathematics, fractal objects can repeat infinitely. For instance, Figure. 28a shows an exact branching fractal which can be zoomed in on at specific scales to show the exact same pattern repeated. In nature, fractals are statistically self-similar and only repeat over a finite length range. For example, the tree branches in Figure. 28b are statistically self-similar over a few orders of magnitude.

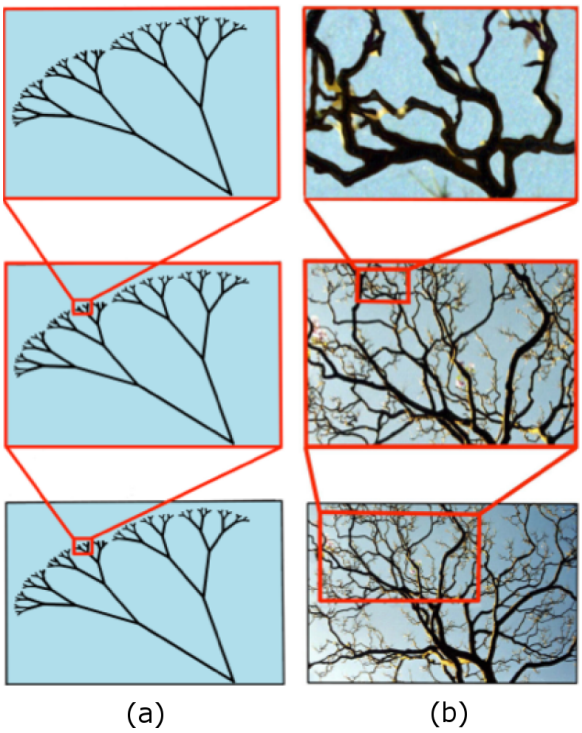

FIGURE 28. Mathematical and natural branching fractals.
(a) The mathematical branched fractal features an exact, infinitely repeating pattern when zoomed in at increasingly fine size scales. (b) The tree branch pattern statistically repeats at finer size scales. However, as with all fractals in nature, the size scale over which it is self-similar is finite.

Mathematically exact fractals can be constructed by scaling an initial seed pattern and then iterating the scaled pattern towards increasing fine size scales. The scaling rate, L, is set by the number of new patterns created, N, and the fractal dimension, D, according to the equation

$$N = L^{-D} \tag{1.34}$$

Throughout the thesis we model branched 'H-tree' fractal electrodes. Figure 29 illustrates H-tree fractals holding D fixed at 2.0 and increasing iterations from 1 to 2 to 3, and also holding the iterations fixed at 3 and increasing D from 1.4 to 1.7. In general, fractals becomes more space filling for increasing iterations or increasing D.

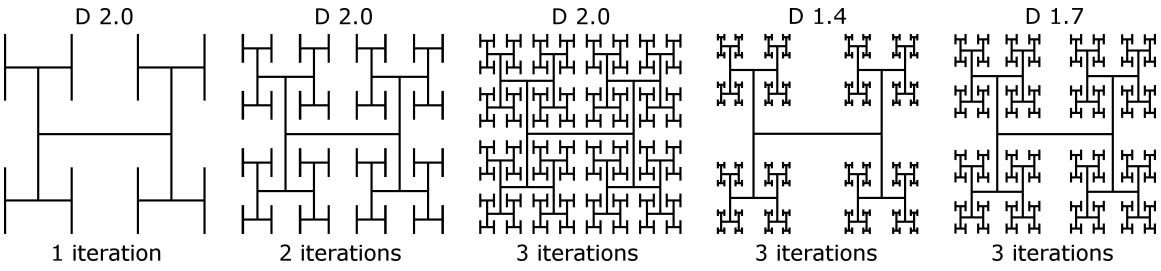

FIGURE 29. H-tree fractal electrodes.
Construction of H-tree inner electrodes with increasing iterations from 1 to 3 at D=2.0 (left 3 patterns) and D values of 2.0, 1.4, and 1.7 at 3 iterations (right 3 patterns).

Throughout this thesis, we utilize fractal geometries to achieve 5 improvents over the conventional Euclidean geometries used in neural electrodes. (1) Fractal electrodes maximize capacitance within a confined volume by maximizing the electrode area [7] [8]. For example, the large number of internal sidewalls for the H-tree electrode shown in Figure 29 provides a large area for charge accumulation. (2) Neurons prefer to attach to regions with high surface roughness [160] [81] [118] and neurites prefer to extend along edge patterns [58] [142] [143]. The fractal generates a high roughness

and a large amount of internal edges. Therefore, we expect the neurite adhesion and outgrowth will be maximized on the fractal, thereby ensuring high stimulation rates. (3) Previous experiments suggest glia can be 'herded' into the gaps between the electrodes depending upon the gap size [58]. Because the fractal features multiple sized gaps, glia could be herded between the gaps. This would allow the glia to continue to support the nearby neurons without forming a glia scar. (4) Fractals exhibit favorable optical properies including extraordinary transmission of light [161] [162] (where the light transmitted through an electrode is greater than a naive 'pixel count' predicted by ray optics) and tuning of the transmitted wavelength [163] [164]. (5) Finally, fractals are mechanically flexible, a desirable property for implanting electrodes in the curved space at the back of the eye [165].

Achieving the ideal fractal retinal implant will involve optimization of D and the number of iterations among each of the five categories listed above. For example, in the next chapter, we show the optimal geometry for stimulating neurons is an H-tree with $D = 2.0$ and 2 iterations. However, future experiments might find neurite outgrowth is optimal at, say, $D = 1.5$ and 2 iterations. We could then choose an intermediate D which optimizes between these competing factors. The work presented in this thesis identified the optimal geometry for electrical stimulation as well as preliminary results for increasing neurite outgrowth and reducing glia scar formation. Future work conducted in our group will consider the optimization of the optical properties and further identify the ideal fractal properties for neurite adhesion and reducing glia scars.

CHAPTER II

FRACTAL ELECTRODES FOR SUBRETINAL IMPLANTS

The research in the first section, "Voltage controlled subretinal implant electrodes", has been published in *Scientific Reports* [7]. Dr. Rick D. Montgomery (RDM) and Dr. Richard P. Taylor (RPT) are co-authors on this publication. Myself (WJW), RDM, and RPT designed the study. WJW and RDM performed the analysis. WJW and RPT drafted the manuscript. The research in the second section, "Photovoltaic subretinal implants", is currently in publication [8]. RDM and RPT are co-authors on this publication. As in the above publication, WJW, RDM, and RPT designed the study. WJW and RDM performed the analysis. WJW and RPT drafted the manuscript.

This chapter investigates improvements in subretinal implant performance that can be achieved by switching from the square electrodes used in today's implants to a fractal electrode. The first section, "Voltage controlled subretinal implant electrodes", assumes that equivalent voltages are supplied to the square and fractal subretinal electrodes and finds that a single fractal electrode can stimulate all surrounding retinal neurons providing a theoretical maximum in restored visual acuity of 20/80, whereas the square cannot. The second section, "Photovoltaic subretinal implants", determines the voltage supplied to square and fractal electrodes by modelling the underlying photodiode's response to inputted radiation. The simulations show that a fractal electrode can achieve complete neural stimulation with 75% less irradiation than the square. The final section, "Tissue heating from subretinal implant electrodes", investigates tissue heating that occurs during subretinal implant stimulation. We find that retinal heating levels from both square

and fractal electrodes are well within the safety limits. This work has not previously been published.

Voltage Controlled Subretinal Implant Electrodes

The emotional and economic impact of vision loss is staggering. According to the Brightfocus Foundation, the annual global cost of retinal diseases is in excess of $340 billion [14]. This has triggered the development of retinal implants to restore vision to victims of retinal diseases such as macular degeneration and retinitis pigmentosa [32] [34] [26] [35] [21] [166] [167] [24]. Human clinical trials have restored visual acuity up to 20/1260 for epiretinal implants [21] (positioned in front of the retina) and up to 20/546 for subretinal implants [32] [34] (positioned at the back). However, the latter was observed in only one patient; for 86% of patients, the visual acuity wasn't restored to a measurable level. Subretinal implants used in the clinical trials featured an array of 1500-5000 artificial photoreceptors fabricated on a 2-3 mm silicon chip, which was inserted into the retinal region where photoreceptors had been damaged [26] [32] [34]. A conventional implant architecture is summarized in Fig. 30. A p-n photodiode receives light and generates an electrical field between the inner and grounded outer electrodes. If located close enough to experience this field, the retina's bipolar neurons are stimulated and pass their signal via ganglion neurons down the optic nerve to the brain's primary visual area [41] [168].

Here, we propose an inner electrode that exploits fractal geometry rather than the Euclidean shapes used in today's implants (Fig. 30). Fractals are prevalent in nature, in part because of their ability to generate a large surface area within a given volume [159]. For example, this allows bronchial trees to transfer oxygen to the bloodstream, trees to absorb sunlight, and coastlines to disperse wave energy. Fractal electrodes'

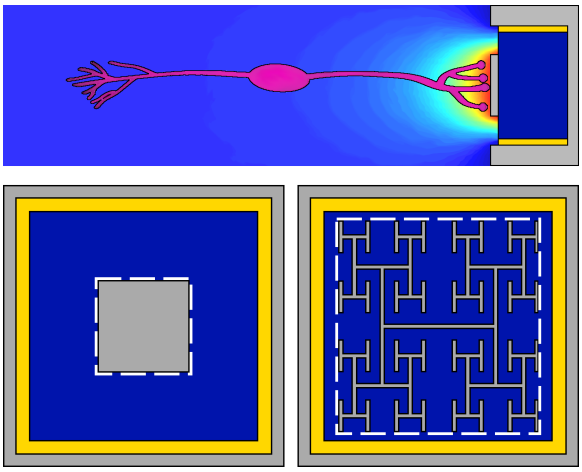

FIGURE 30. The subretinal implant design.
(Top) Side-view. Light passes through the retinal layer of neurons (pink) to reach the photodiode (dark blue). The photodiode then generates a voltage difference between its two electrodes (grey) which are separated by an insulating region (yellow). (Bottom-left) Top view of the traditional design featuring a square inner electrode. (Bottom-right) Top view of our fractal inner electrode featuring a repeating H design. In both cases, the dashed white line indicates the bounding perimeter of the inner electrode.

large surface area increases their capacity to hold electrical charge, which in turn generates large electric fields. Our fractal electrodes feature branching patterns that repeat at different size scales, similar to the neuron dendrites they interface with [169] [170]. These fractals contrast with other electrodes which feature a fractal mountain roughness [171] [62]. In addition to their enhanced fields, both types of fractal electrode are expected to promote neural adhesion. Experiments demonstrate that neurons adhere preferentially to textured surfaces [160] [81] [118]. In particular, they extend their neurites along the texture established by edge patterns [58] [142] [143]. Because our fractal branch design maximizes the density of electrode edges compared to Euclidean geometries, the resulting texture might increase neural adhesion. Their resulting proximity to the electric field would then ensure high stimulation rates.

Our fractal branch design offers two more advantages for retinal implants that are absent for fractal mountain electrodes. Firstly, the gaps between the fractal branches allow light to pass into the underlying photodiode. Studies unrelated to implants have shown that the gaps in fractal electrodes exhibit extraordinary transmission of electromagnetic radiation [161] [162] (i.e. the transmitted radiation is greater than a simple pixel count of the electrode's covering area would predict), and that the transmitted wavelength (and therefore color) can be tuned [163] [164]. Adopting a fractal branch design for implants could therefore result in enhanced light sensitivity. Secondly, fractal structures are mechanically conformal [165], a highly desirable quality for electronics required to match the retina's curved surface. Based on this potential to integrate their favorable electrical, adhesive, optical, and mechanical properties, here we quantify the superior neural stimulation generated by the enhanced capacitance of branched fractal electrodes compared to Euclidean designs.

Methods

Modified Nodal Analysis

The general strategy applied throughout the paper in determining electrode, neuron, and photodiode responses is to mesh three-dimensional geometries into a set of nodes, establish an equivalent circuit model between nodes (e.g. Fig. 32a,c for two-dimensional illustrations), and calculate the node voltages using modified nodal analysis (MNA) [172]. Briefly, MNA determines node voltages by applying Kirchoff's current conservation rule at each node along with the appropriate boundary conditions. For n node voltages, $\vec{V} = (V_1, \ldots, V_n)$, and m applied voltage sources, $\vec{V}^{app} = (V_1^{app}, \ldots, V_m^{app})$, the MNA system of equations is given by

$$\begin{pmatrix} G & A^T \\ A & 0 \end{pmatrix} \begin{pmatrix} \vec{V} \\ \vec{I} \end{pmatrix} = \begin{pmatrix} \vec{I}^{app} \\ \vec{V}^{app} \end{pmatrix} \tag{2.1}$$

where G is an $n \times n$ matrix containing conductance elements between nodes, A is an $m \times n$ matrix that sets boundary conditions to the applied voltages and only contains zeros and ones, $\vec{I} = (I_1, \ldots, I_m)$, gives the m currents flowing through the applied voltage sources, and $\vec{I}^{app} = (I_1^{app}, \ldots, I_m^{app})$ applies current sources to the n nodes. The lower right $m \times m$ matrix is zero. The system of equations is solved using the package SuperLU [173] [174].

It's helpful to understand modified nodal analysis with a brief example. Consider the circuit diagram shown if Fig. 31. There are four nodes, 1 through 4, each with their own potential, V_1 through V_4. The impedance between each node is illustrated. The boundary condition potentials are given by $V_1 = V_{app}$ and $V_4 = 0$. Current conservation at each node can then be written in terms of the matrix equation shown below.

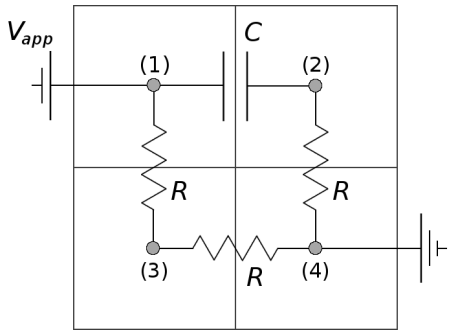

FIGURE 31. Example circuit used to illustrate modified nodal analysis algorithm.

$$\begin{pmatrix} \frac{1}{R}+C\frac{d}{dt} & -C\frac{d}{dt} & -\frac{1}{R} & 0 & 1 & 0 \\ -C\frac{d}{dt} & \frac{1}{R}+C\frac{d}{dt} & 0 & -\frac{1}{R} & 0 & 0 \\ -\frac{1}{R} & 0 & \frac{2}{R} & -\frac{1}{R} & 0 & 0 \\ 0 & -\frac{1}{R} & -\frac{1}{R} & \frac{2}{R} & 0 & 1 \\ 1 & 0 & 0 & 0 & 0 & 0 \\ 0 & 0 & 0 & 1 & 0 & 0 \end{pmatrix} \begin{pmatrix} V_1 \\ V_2 \\ V_3 \\ V_4 \\ I_V \\ I_G \end{pmatrix} = \begin{pmatrix} 0 \\ 0 \\ 0 \\ 0 \\ V_{app} \\ 0 \end{pmatrix} \tag{2.2}$$

where I_V is the current flowing through the battery and I_G is the current flowing through ground. There are four nodes and two boundary conditions, so the total number of equations is six. Equation 2.2 can be solved for the four node potentials and the currents flowing through the battery and through ground.

Electrode Operation

An equivalent circuit model was used to solve for the extracellular potential surrounding a TiN electrode (Fig. 32a). Each three-dimensional geometry was first meshed into a set of tetrahedral nodes using COMSOL. The meshes were then exported and the node-to-node impedances defined using custom C code. The fluid-fluid nodes are resistive while the fluid-electrode nodes consist of a capacitive and resistive branch in parallel [63]. The tissue resistivity was taken to be $3.5 \times 10^3\,\Omega$cm, the resistivity measured at the photoreceptor layer in macaques monkeys [28]. The specific capacitance of a TiN electrode is $2.5\,\mathrm{mF/cm^2}$ [70] and the surface resistivity is $3 \times 10^5\,\Omega\mathrm{cm}^2$ [175]. The electrode surfaces were assumed to be at an equipotential. A bounding domain of $1\,\mathrm{mm}^3$ was used for each electrode geometry. The boundary conditions were set to a potential of 0 V on the 5 faces of the cube far away from the

electrode and an insulating boundary for the face which the electrode lies on (Fig. 32b).

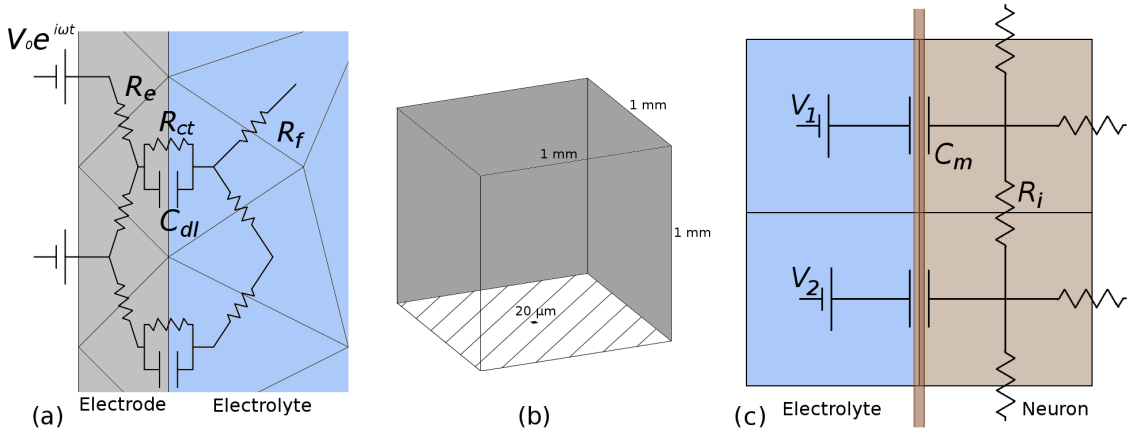

FIGURE 32. Electrode and neuron equivalent circuits.
(a) Equivalent circuit model with tetrahedral nodes for an electrode surrounded by a conducting electrolyte. (b) Boundary conditions for the bounding domain were set to V = 0 V on the 5 surfaces far from the center electrode (dark grey) and insulating on the bottom surface (striped). The 20 μm electrode (black) sits on the bottom surface. (c) Equivalent circuit model with cubic nodes for a neuron in an electrolyte undergoing high frequency stimulation. The external potential obtained from the electrode-electrolyte simulations was mapped onto the corresponding extracellular neural node, for example, V_1 and V_2.

With the equivalent circuit model established, modified nodal analysis (MNA) [172] was used to create a system of equations based on solving current conservation equations at each node along with the appropriate boundary conditions. The number of equations was given by the total number of nodes, n, plus the number of applied potential source nodes, m. The solution output consisted of n complex valued potentials and m complex valued currents (the complex valued potentials and currents arise from capacitive and resistive components). By applying a sinusoidal potential to the inner electrode, the voltage time derivative for current crossing the electrode-fluid interface, $C_{dl}d(V_e - V_f)/dt$, dropped off, where V_e and V_f are complex valued node voltages of an electrode and fluid element, respectively, and C_{dl} is the interfacial

capacitance. Additionally, since each node oscillated at a frequency, f, the $e^{i2\pi ft}$ term could be factored out from the system of equations. The system of equations then formed a sparse matrix which was solved using the linear equations software library, Distributed SuperLU [173] [174]. Up to ∼3 million node potentials were solved for. The resulting voltages and currents at differing locations all oscillated with frequency, f, but were not necessarily in phase due to varying capacitive and resistive components. Throughout the text, the peak magnitude within each cycle of the extracellular voltage is presented rather than the voltage at a specific time unless otherwise stated. We note that the extracellular potential at the neurons soma is within 1° of phase of the potential at the inner electrode. Although we only tested sinusoidal applied potentials, because any periodic waveform can be written as a sum of sines and cosines, this method could be used, in principle, to apply square waves, triangular waves, or any periodic waveform to the electrode. In addition to determining the potential and currents, the charge density delivered per phase at each node, Q_{ph}, on the electrode surface was also calculated by

$$Q_{ph} = \int_0^{\frac{1}{2f}} dt C_{dl} \left| \frac{d(V_e - V_f)}{dt} \right| = 2C_{dl}|V_e - V_f| \tag{2.3}$$

Neuron Response

The real and imaginary parts of the extracellular potentials computed from the electrode-electrolyte simulations were then mapped onto the outside membrane of the bipolar neuron (Fig. 32c). We considered extracellular stimulation of passive bipolar neurons (i.e., featuring no voltage-gated ion channels), as has been done previously [176] [177]. Although recent studies indicate voltage-gated transient calcium channels in retinal bipolar neurons are open at the extracellular stimulating frequencies that we operate at, 1000 Hz [43], calcium current through these open channels is negligible

for depolarizations up to ∼15 mV [44]. Therefore, the applied voltage, V, necessary to depolarize all 9 neurons above an electrode to the $\Delta V_m = 15$ mV condition associated with stimulating downstream ganglion neurons [178] is not affected by our models exclusion of voltage-gated channels.

Each neuron was 100 μm in length with a 10 μm diameter soma centered 30 μm above the electrode surface and with 1 μm wide branches [59] [60]. The neuron was first meshed into a set of cubic nodes using MATLAB code. Our custom C code then defined the node-to-node impedance by a capacitive impedance across the neuron membrane and an internal cytoplasmic resistance for the neuron-neuron nodes (Fig. 32c). The passive membrane properties of rod bipolar cells are given by a membrane resistivity $R_m = 2.4 \times 10^4\,\Omega\text{cm}^2$, a membrane capacitance $C_m = 1.1 \times 10^{-6}\,\text{F/cm}^2$, and a cytoplasmic resistivity of $R_i = 1.3 \times 10^2\,\Omega\text{cm}$ [179]. The capacitive and resistive components of the membrane impedance are in parallel. We ignored the membrane resistance since the capacitive impedance across the membrane is more than two orders of magnitude lower than the resistive impedance at frequencies of 1 kHz or more. We note that our two-step process of using a tetrahedral grid for the electrode-electrolyte simulations and a cubic grid for the electrolyte-neuron simulations had to be used because a single mesh consisting of electrode, electrolyte and neuron was too complex computationally to be meshed together. The external voltage applied to the neuron was transferred from the electrolyte potential solution to the external neural potential by using the barycentric coordinate formula to determine which tetrahedral node the cubic node fell into. From here, another MNA matrix was set up and solved using Distributed SuperLU. The solution contains the complex valued potential at each node in the model neuron.

Results

Electrode Properties

We modelled retinal implants operating with a sinusoidal electrical potential of frequency f, $V = V_0 e^{i2\pi ft}$, applied to capacitive TiN electrodes in retinal fluid. This oscillating potential is necessary to overcome ionic screening by the fluid and can be achieved by modulating the light entering the photodiode [36]. We chose a sine wave oscillation because of its broad applicability. Any waveform, including the square waves typically used in today's implants [32] [36], can be constructed from a Fourier sum of sine waves. Demonstration of the superior operation of the fractal electrode for a sine wave will automatically translate to a sum of sine waves and therefore to any waveform. We also note that, for simplicity, we excluded the rest period between pulses which retinal implants employ to minimize visual percept fading [32] [180]. Its inclusion post simulation would not impact any demonstration of superior operation.

The electrode height was 250 nm and the outer dimension of the ground electrode was $20\,\mu$m x $20\,\mu$m. The three chosen geometries for the inner electrode (fractal, square and grid) had identical covering areas of $50\,\mu\text{m}^2$, where covering area is the top surface area of the inner electrode (i.e. the area which blocks incoming light ignoring diffraction and extraordinary transmission). This was done to standardize light transmission. To model the electrodes' electric fields, three dimensional geometries were meshed and node-to-node impedances were defined using an equivalent circuit model (Methods).

When a voltage V is applied, the electric charge distributes throughout the electrode to minimize the Coulombic energy with the amount of charge set by the capacitance. The geometric contribution to capacitance can be approximated by

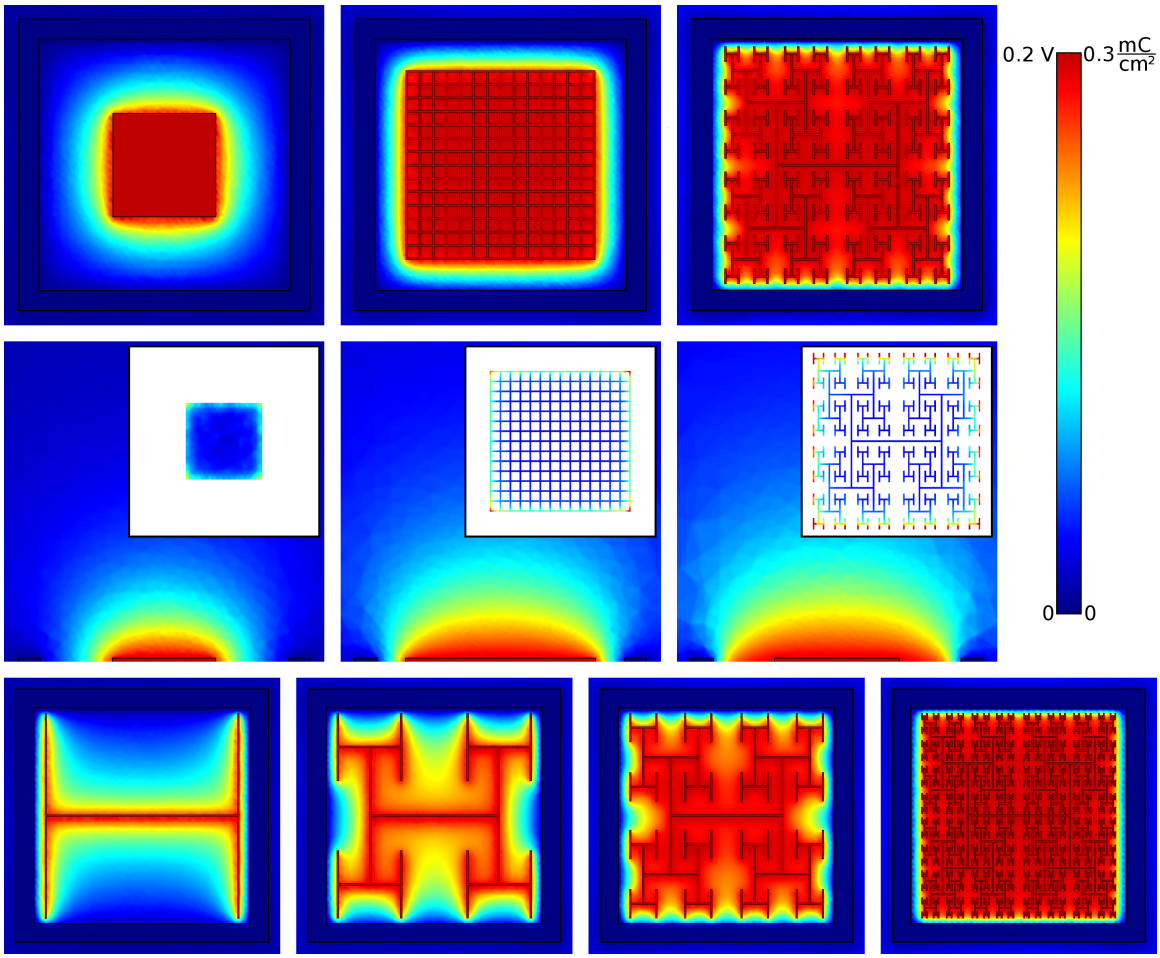

FIGURE 33. Square, grid, and fractal extracellular voltages under equivalent bias. The maximum extracellular voltages reached during each oscillation for the square, grid, and the 3-iteration fractal electrodes (each with an electrode height of 250nm). In each case, the applied voltage was $V_0 = 0.2$ V and $f = 1$ kHz. A horizontal slice (at the inner electrodes top surface) of the three-dimensional voltage distribution for each electrode geometry is shown in the top row. Vertical slices through the middle of the electrodes are shown in the middle row. The charge density on the top surface of each inner electrode is shown in the insets. The bottom row shows the field uniformity achieved by increasing from 0 to 4 iterations.

$C \sim A_{eff}/d_{eff}$, where A_{eff} is the effective area (i.e. the area available for charge accumulation) and d_{eff} is the in-plane separation distance between inner and outer electrodes. When the covering area is held constant across the 3 electrode geometries, the multi-sized gaps in the fractal design give rise to a larger bounding perimeter than

the grid or the square. This increases A_{eff} while also reducing d_{eff}, with a net effect of maximizing the capacitance for all frequencies typically used in neural stimulation, 100 Hz - 10 kHz. The increase in A_{eff} results from an inherent interplay of fractal features, as follows. The charge distribution simulations (Fig. 33) demonstrate that much of the charge resides on the bounding perimeter, providing a physical explanation for why the fractal electrode with its large bounding perimeter holds so much charge. Surprisingly, the presence of gaps in the fractal electrode doesnt reduce A_{eff} below the Euclidean values. Instead, the gaps generate a large pattern perimeter and the associated vertical side walls supply extra area for charge accumulation. The increased capacity to hold charge leads to the fractal electrode generating an extracellular field which extends further from the electrode surface (Fig. 33). This field penetration is enhanced by the lower resistance of the liquid surrounding the fractal electrode (Fig. 34). As expected, the vertical component of the current also

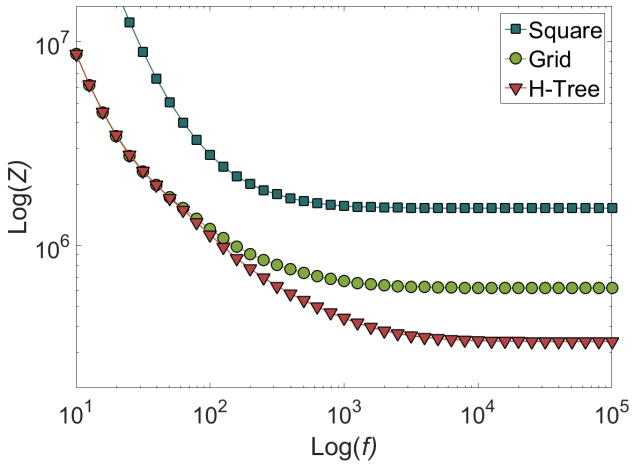

FIGURE 34. Square, grid, and fractal impedance versus frequency
Impedance Z plotted against oscillation frequency f for square, grid, and fractal H-tree geometries. At large f, Z is inversely proportional to the bounding area of the electrode (total area enclosed by the white dashed lines in Fig. 30).

penetrates further (Fig. 35). With enough fractal iterations, both the field and current density become as uniform as those of the square despite the presence of the light-transmitting gaps (Fig. 33). The field penetration of the grid is intermediary to that of the square and fractal. As with the fractal, the grid also increases its surface area due to the internal side walls. However, the fractal more efficiently utilizes its available area within the 20 μm confined space due to its larger bounding area.

To optimize the enhanced field penetration achieved by the fractal geometry, we simulated different electrode heights varying from 25 nm to 1 μm. The ground electrode's height was kept constant at 250 nm in order to isolate the fractal effect. As the fractal's height is increased, and more charge accumulates on the vertical walls, the field becomes more uniform (Fig. 36). In particular, the average field at the electrodes surface begins leveling off as the electrode height approaches 250 nm (Fig. 36b). This observed saturation height is confirmed by de Levie's model [181] [182], which states that charge accumulation on the gap's vertical sidewalls switches from using all available area at low gap depths to accumulating predominantly at the top of the sidewalls at large depths. This crossover behavior occurs at the field's penetration depth into the gap, $\lambda_p = 1/4\sqrt{\sigma d/\pi f C_{dl}}$, where σ is the electrolytic conductivity, C_{dl} is the interfacial (double layer) capacitance of the electrode, and d is the gap diameter. For the 3 iteration fractal, the largest circle that can be inscribed in the fractal's gaps has $d = 1.7\,\mu$m, resulting in λ_p= 200 nm. The slight increase in average field as the electrode height exceeds λ_p is due to the continuing charge buildup on the sidewalls at the bounding perimeter. Combined, these two effects lead to the observed increased field penetration as a function of electrode height (Fig. 36c). Although the fractal geometry will therefore increasingly out-perform the square for

larger electrode heights, for the remainder of the discussion we focus on 250 nm to facilitate a direct comparison with today's implants.

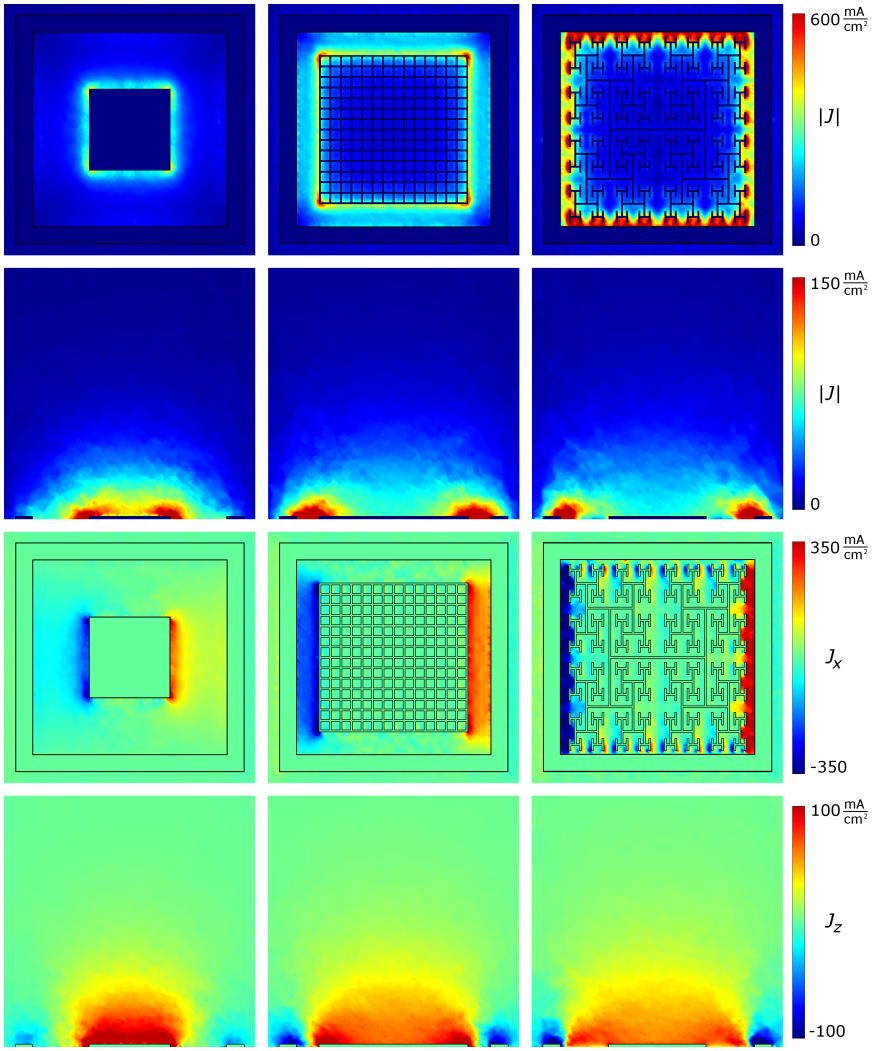

FIGURE 35. Square, grid, and fractal extracellular E-fields under equivalent bias. Current density J surrounding the square, grid, and H-tree electrodes occurring at the electrodes maximum voltage within each oscillation for an applied voltage with $V_0 = 0.2$ V and $f = 1$ kHz. First and second rows show the current density magnitude for a horizontal slice at the inner electrodes surface and a vertical slice half way through the electrode, respectively. The third row shows the horizontal component of the current density J_x at the inner electrodes surface (where x is the left-right direction). The fourth row shows the vertical component of current density J_z at the slice half way through the electrode.

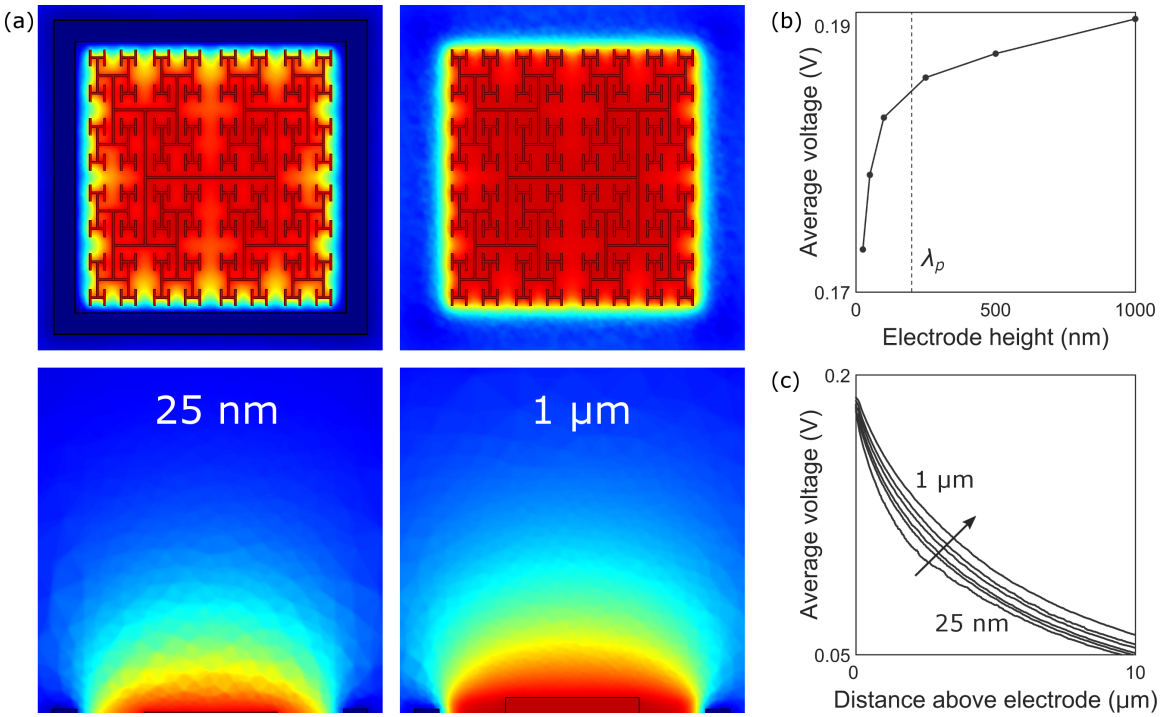

FIGURE 36. Varying fractal electrode height.
(a) Maximum extracellular voltages reached during each oscillation for inner electrode heights of 25 nm (left) and 1 μm (right). In each case, the applied voltage was $V_0 = 0.2$ V and $f = 1$ kHz. The scale ranges from 0 V (blue) to 0.2 V (red). A horizontal slice (at the inner electrodes top surface) of the three-dimensional voltage distribution is shown in the top row. Vertical slices through the middle of the electrodes are shown in the bottom row. (b) The average voltage at the inner electrode surface (averaged across locations within the bounding perimeter) for varying electrode heights. The penetration depth, λ_p, occurs at 200 nm. (c) The average voltages plotted as a function of distance above the inner electrode surface for inner electrode heights of 25 nm, 50 nm, 100 nm, 250 nm, 500 nm, and 1 μm (bottom to top).

Neural Stimulation

Because of the enhanced voltage penetration, the fractal electrode induces larger voltage differences across the neuron membranes compared to the square at the same V (Fig. 37 and Fig. 38). To show this, a patch of 9 bipolar neurons was placed directly above each inner electrode. Voltages obtained from the first part of the

simulation were mapped onto the outer membrane of each neuron and an equivalent circuit model was used to solve for the neurons internal potentials (Methods). Bipolar neurons have an analog response with depolarization ΔV_m (the change of potential across the membrane before and after stimulation) growing gradually with applied voltage. Previous experiments suggest that the downstream ganglion neurons are stimulated when $\Delta V_m = 15$ mV at the bipolar neuron's soma [178]. Measuring ΔV_m

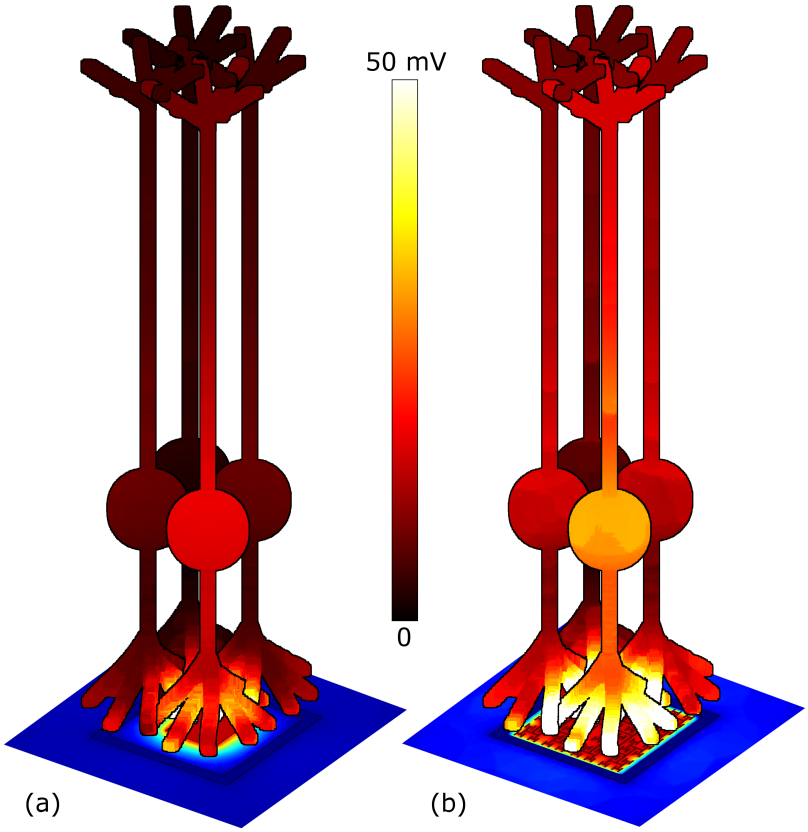

FIGURE 37. Neuron depolarization magnitudes above square and fractal electrodes. Plot of the maximum ΔV_m (the change of potential across the membrane before and after stimulation) for a patch of bipolar neurons above (a) the square and (b) fractal electrodes both with $V_0 = 0.2$ V and $f = 1$ kHz. Maximum ΔV_m within an oscillation is plotted to quantify the greatest stimulation achieved during a cycle. For visual clarity, only 4 of the 9 neurons (center and 3 surrounding) are shown. Images are drawn to scale; the neurons are 100 μm in length and the soma is centered 30 μm above the surface.

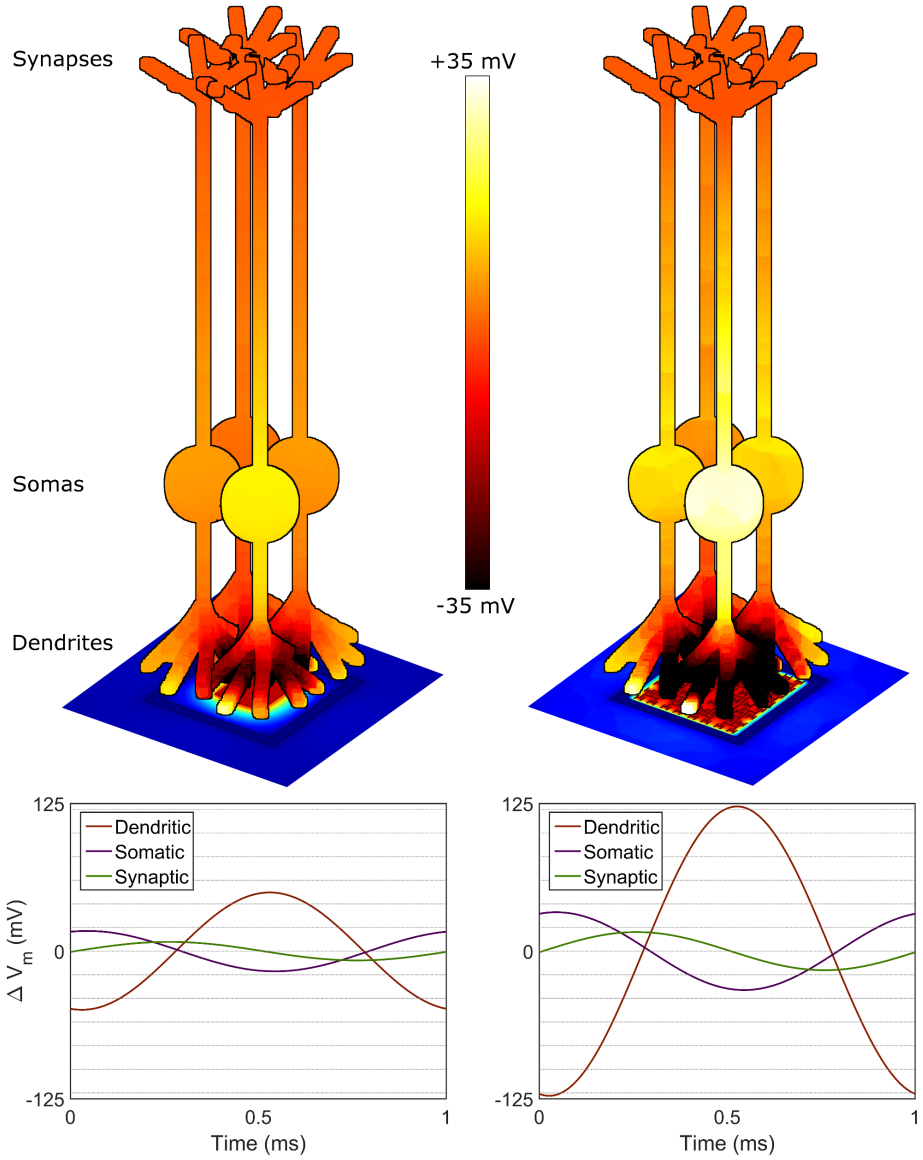

FIGURE 38. Membrane potential changes during one voltage cycle. Top: Change in membrane potential, ΔV_m, for a patch of 4 bipolar neurons at the time of maximum somatic depolarization for the square (left) and H-tree (right) electrodes. In each case, this maximum somatic ΔV_m occurs during the positive phase of applied electrode voltage. For both the square and fractal electrodes at this time in the cycle, the neurons soma and synapses are depolarized while the dendrites are hyperpolarized (i.e., $\Delta V_m < 0$). Bottom: ΔV_m is compared at three locations for the central neuron (dendritic, somatic, and synaptic) as a function of time during the electrodes oscillation. For the fractal, the peak synaptic depolarization leads the peak somatic depolarization by 77° degrees of phase while for the square it leads by 78°.

at the somas, the center neuron (the front most neuron in Fig. 4) above the fractal electrode was depolarized by ∼80% more than the center neuron above the square for $V_0 = 0.2$ V. This larger depolarization for fractal versus Euclidean geometries requires 2 or more iterations (Fig. 39).

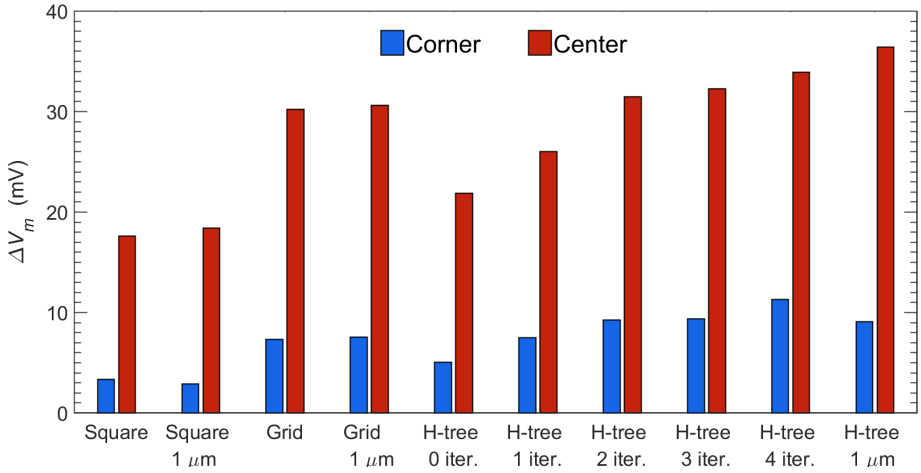

FIGURE 39. Neuron depolarizations versus electrode geometry. ΔV_m for neurons located directly above the electrode for each electrode geometry with $V_0 = 0.2$ V and $f = 1$ kHz. Neurons positioned above the electrodes' center are represented in red, while those positioned above the electrode's corners are shown in blue. The associated extracellular potentials are shown in Fig. 33. There is a general trend towards greater depolarization as more iterations are added into the H trees. There is also a trend of increased depolarization for the center neuron above 1 μm electrodes (compared to 250 nm for the other bars).

To compare stimulation efficiencies, we considered the condition when all 9 bipolar neurons above each electrode (1 center, 4 edges, 4 corners) depolarize by the 15 mV necessary for ganglion stimulation. All 9 neurons above the fractal electrode depolarized by 15 mV for $V_0 = 0.32$ V while, at this same applied voltage, only the center bipolar neuron above the square met this requirement (Fig. 40). In fact, all 9 neurons above the square did not reach 15 mV depolarization until $V_0 = 0.90$ V. The voltage required for the grid geometry to stimulate all nine neurons was 0.41 V, intermediary to the fractal and square. We emphasize the general applicability of the

above results. The fractals superior operation quantified for one sine wave voltage oscillation will be amplified for a summation of sine waves and therefore for the square waves typically used in today's implants.

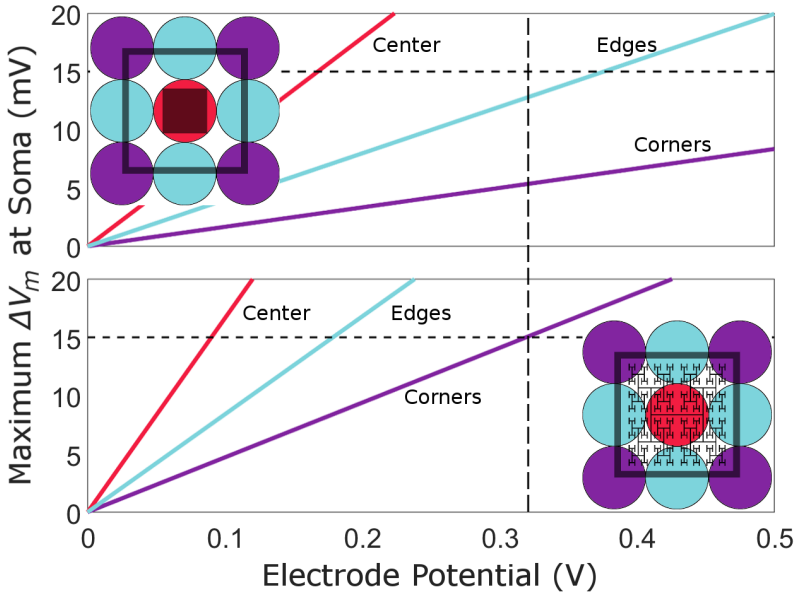

FIGURE 40. Threshold electrode voltages.
Maximum ΔV_m at the soma plotted against electrode voltage for the 9 bipolar neurons (1 center neuron, red; 4 edge neurons, blue; and 4 corner neurons, purple) above square (top) and fractal (bottom) inner electrodes (each located within an outer electrode of width 20 μm). The vertical dashed line indicates the potential at which all 9 bipolar neurons above the fractal electrode have reached the 15 mV depolarization condition for ganglion stimulation.

Discussion

We have shown that the branching fractal geometry is an effective approach to increasing the electrodes capacitance within the confined area of a 20 μm pixel while still facilitating light transmission into the underlying photodiode. Compared to conventional Euclidean geometries, this increased capacitance results in the field penetrating further into the extracellular space and, consequently, an

improved stimulation of bipolar neurons. The voltage required to reach the 15 mV depolarization for all 9 neurons above the electrode was 0.90 V for the square but only 0.32 V for the fractal.

This enhanced stimulation holds a number of consequences for subretinal implant operation. Firstly, the fractal voltage resulted in a maximum charge density of only $0.83\,\mathrm{mC/cm^2}$ on the electrode's surface. In contrast, at 0.90 V, the charge density at the square's corners reached $1.01\,\mathrm{mC/cm^2}$, above the $1\,\mathrm{mC/cm^2}$ safe charge limit at which TiN electrodes induce hydrolysis [66]. Secondly, the enhanced stimulation influences the visual acuity achieved by the implant as follows. For a typical silicon photodiode (0.6 V open circuit voltage), the fractal voltage can be generated with a single diode of pixel width $20\,\mu$m. In contrast, to reach 0.90 V, the square design would require linking 2 or more diodes in series, with current Euclidean designs using 3 photodiodes occupying a $70\,\mu$m pixel width [36]. In a simplistic picture, pixel size directly impacts acuity. In natural vision, 20/20 acuity is achieved by resolving 1 arcminute of visual scene, corresponding to a $5\,\mu$m pixel at the retina [35]. Assuming acuity scales inversely with pixel size in electronically restored vision, the $70\,\mu$m Euclidean design would generate 20/280 and $20\,\mu$m fractal would generate 20/80 acuity.

It is important to note, however, that pixel size is not the sole factor determining the acuity generated by today's Euclidean electrodes. One limiter which has the potential to reduce visual acuity is electrode crosstalk (when the field from one electrode stimulates the neurons above a neighboring electrode). However, this can be reduced by surrounding each inner electrode with a grounded outer electrode [183] [184] such as employed here. To check the extent of the fractal electrodes' crosstalk, the depolarization of a neuron centered above a neighboring electrode was measured

(Fig. 41a). With one of the fractal electrodes (left) set at its operating voltage of 0.32 V and no voltage applied to the adjacent electrode (right), the neighboring neuron was depolarized by 5.7 mV. For identical voltages applied to square electrodes, the neighboring neuron was depolarized by 2.1 mV. In summary, for the voltage at which all nine neurons above the fractal electrode were stimulated and only one was stimulated above the square, the depolarization of the neighboring neuron due to cross talk remained less than half of the 15 mV stimulation condition. This crosstalk could potentially be reduced even further by employing different grounding electrode strategies [184].

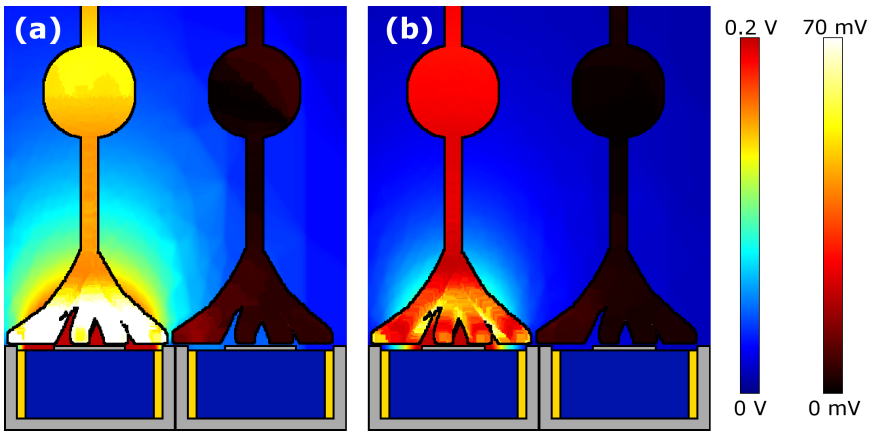

FIGURE 41. Electrical crosstalk for subretinal electrodes.
Side-view of neurons above two neighboring photodiodes with (a) fractal and (b) square electrode geometries. For both geometries, each photodiode features the inner and outer grounded electrodes shown in Fig. 30. In each case, the inner electrode of the left photodiode was biased at $V_0 = 0.32$ V and $f = 1$ kHz, while the inner electrode of the right photodiode was unbiased. Scale bar for the electrodes field ranges from 0 V (blue) to 0.2 V (red). Scale bar for the neuron stimulation ranges from 0 mV (black) to 70 mV (white).

Another limiter is that the Euclidean implants induce glia scarring on their smooth electrode surfaces [51] which prevents neurons from maintaining close proximity to the electric fields. However, adopting a textured surface reduces glia

scarring and keeps neurons in closer proximity to the textured regions [40] [58]. Because the fractal exhibits extensive texture generated by its many inner edges as compared to the square's four outer edges, we predict the fractal will promote stimulation by ensuring that the neurons are located well within the electrode's electric field.

Experiments performed on rats with retinal implants reveal a degradation factor of 5.8 in the measured visual acuity when compared to the expected acuity calculated from pixel size [185]. However, this experiment did not employ the local grounded electrodes of our design. Taking into account the minimized crosstalk and potentially reduced glial scarring, we expect the degradation factor of the fractal designs to be less than the 5.8 factor of Euclidean designs, with the precise factor to be quantified by future experiments. However, if we consider a pessimistic scenario and apply a Euclidean degradation factor of approximately 5 to the reduced pixel size of our fractal implants, the predicted acuity is 20/400. In order to gain widespread use, implants must restore vision to ambulatory levels (i.e., those associated with the ability to independently navigate rooms and streets) of 20/400 vision [186]. Our fractal implants therefore offer the first viable approach to restoring vision to ambulatory or better levels.

In the current study, we focused on subretinal implants which stimulate the bipolar neurons located at the retina's back surface. In our discussions, we assumed the voltage, V, was generated by a photodiode [35] but it could equally be generated by an external voltage source [166]. In either case, the fractal generates an enhanced field leading to greater neuronal stimulation to that achieved by the Euclidean designs considered in this paper. We expect fractal electrodes to also outperform Euclidean geometries in epiretinal implants. However, this would require a lower number of

fractal iterations for the following reason. For subretinal implants, the 3 iteration fractal electrode generates a uniform electric field that maximizes stimulation of the bipolar neurons aligned perpendicular to the electrodes. In contrast, epiretinal implants stimulate parallel ganglion axons through a large spatial variation in the electric field [47] [48]. This can be generated by employing the 1 iteration fractal rather than the square electrode (Fig. 33).

In addition, fractal electrodes could be employed for deep brain stimulation, which is being used to address conditions ranging from Parkinson's disease [187] to depression [4], and for prosthetic limbs [5]. In terms of the latter application, it is interesting to contrast our use of fractal electrodes to another study based on larger (5 mm compared to our 20 μm) fractal electrodes designed to stimulate peripheral neurons in the human arm [188]. In our study, we exploit fractal geometry to maximize the electrode's effective capacitive area A_{eff} for a constant covering area by embedding repeating patterns within the confined region of a photodiode pixel. In contrast, the limb study employs the repeating patterns to build outward at the expense of losing pixel resolution. The authors show that this large fractal boundary leads to a considerable variation in local charge density, which generates the large spatial variation in the electric field necessary for stimulating peripheral neurons. The two studies demonstrate how fractal geometry can be exploited to achieve very different goals and, taken together, highlight the great promise for future integration of fractal electronics with the human body.

Photovoltaic Subretinal Implants

In order to optimize the electrode geometry, we must balance two competing factors. In the previous section, we explored neuron stimulation from square, grid, and fractal electrodes with equivalent top-contact covering areas and with equivalent applied voltages. These voltages were assumed to be supplied by the underlying photodiode. However, for equivalent irradiances, the photodiodes will generate different voltages depending upon the top-contact electrode geometry; the more light an electrode blocks (i.e., larger covering area), the lower the generated voltage. However, in contrast to this, larger covering areas increase the electrode's capacitance and thus the field delivered to the extracellular space. Therefore, optimizing the electrode geometry requires a balance between transmitting lots of light into the photodiode while still maintaining a high capacitance.

In this section, we investigate fractal electrodes as a means towards achieving a high capacitance while still transmitting light into the photodiode and compare these results to square electrodes. We tune the size of square electrodes and the fractal dimension and number of iterations on H-tree electrodes to optimize the neural stimulation achieved between light entering the photodiode and voltage on the top contact electrode. We show by optimizing the fractal inner electrode geometries, all neighboring neurons can be stimulated using 74% less irradiation (12 mW/mm^2) compared to the best optimized square (47 mW/mm^2), providing a visual acuity up to 20/80. In contrast, the square at 12 mW/mm^2 only stimulates $\sim$10% of the neighboring neurons. By ramping up the irradiation, the square can stimulate all surrounding neurons, although it is very near the maximum permissible exposure safety limit. In contrast, the fractal is capable of long-term safe stimulation due to its significantly reduced irradiation requirements. Therefore, by optimizing the fractal

electrode, the threshold irradiation necessary to stimulate all neighboring neurons is significantly reduced compared to square electrodes. Adoption of the fractal electrode for subretinal implants can lead to a safe, long-term restoration in visual acuity up to 20/80.

Introduction

The promise of restoring vision to patients blinded by dry age-related macular degeneration (AMD) and retinitis pigmentosa (RP) has spurred the development of retinal implants worldwide [32] [34] [26] [35] [21] [166] [167] [24]. In the United States alone, an estimated ∼50,000 people are blind (with visual acuity $< 20/200$) due to dry AMD [189] [14] and ∼20,000 due to RP [13]. Central to both AMD and RP is the loss of the light-detecting photoreceptors (i.e., rods and cones), while the remaining retinal neurons remain intact [10][11]. The goal of electronic retinal implants is to replace these lost photoreceptors by electrically stimulating the remaining healthy retinal layers with a pattern of the visual surroundings. Currently, retinal implants restore vision up to a visual acuity of 20/1260 for epiretinal implants (positioned at the front of the retina) [21] and 20/546 for subretinal implants (positioned at the back of the retina) [32][34]. However, the restored acuity for subretinal implants has only been achieved in one patient; 86% have no measureable restored acuity. Therefore, restoring vision beyond even the blindness level would represent a revolutionary breakthrough in retinal implant performance.

Today's photodiode-based subretinal implants feature arrays of up to 1500 photodiodes on 1-3 mm implants [32] [41]. Each photodiode (pixel) is 70 μm wide. A prototypical design for a subretinal photodiode is shown in Figure 30a. Radiation incident on the silicon generates a voltage difference between an inner electrode and an

outer grounded electrode. The associated electric field extends into the extracellular fluid of the retina and stimulates nearby bipolar neurons which then pass their signals downstream to ganglion neurons and from there to the visual cortex. Traditional designs employ a square-shaped inner electrode (Fig. 30b). Proponents of the square electrode design face a predicament though; the electrode's surface area should be maximized to increase its electrical capacitance so that the field generated by the large amount of charge on the electrode extends far into the extracellular space. Unfortunately, increasing the surface area also blocks more light from entering the underlying photodiode which reduces the inner electrode voltage and the associated electric field.

Recently, our simulations demonstrated that replacing the square electrode with a branched fractal electrode (Fig. 30c) increases the capacitance while still permitting light into the photodiode, resulting in a significant improvement in visual acuity of up to 20/80 [7]. Inherent to all fractal objects is a large surface area to volume ratio [159]. Our fractal electrodes use this large surface area to store more charge (i.e. an increased capacitance) within a confined volume. Other researchers had previously investigated fractal mountain electrodes which use a roughened surface to increase surface area and thus capacitance [171][62]. However, the mountain electrode, like the square, blocks incident light from entering the photodiode. Our branched fractal electrode provides the ideal solution to this problem - the sidewalls of the repeating branches generate a large surface area and capacitance while the gaps between the branches allow the light to pass through. In particular, a 20 μm pixel featuring a branched fractal electrode was shown to stimulate all neighboring neurons (i.e. all neurons immediately above the electrode) using an electrode voltage which was less than the open-circuit voltage generated by a typical silicon photodiode [7]. In

contrast, the equivalent square electrode required voltages in excess of those generated by a single photodiode. Consequently, conventional implants featuring non-fractal electrodes employ 3 photodiodes per pixel in order to generate a large enough voltage to stimulate the neighboring neurons [41][36]. However, the larger pixel size reduces the visual acuity.

In addition to an increased capacitance, fractal electrodes offer 3 other potential advantages over conventional implants. (1) The fractal geometry introduces a textured surface topography featuring many electrode edges. Because neuronal adhesion is greater on textured surfaces [160] [81] [118] and neurites also prefer to extend along edges [58] [143] [142], we expect the target neurons will remain in closer proximity to the fractal electrodes than to geometries with fewer edges. This closer proximity to the field promotes neural stimulation. (2) Fractal electrodes exhibit favorable optical properties, including extraordinary transmission (whereby the transmitted light intensity is greater than that expected from a simple pixel count of the photodiode's exposed area) [162][161] and tuning of the transmitted wavelength [163][164]. In particular, extraordinary transmission could make the inner electrode effectively transparent, allowing a larger photocurrent to be generated per watt of incoming radiation. (3) Finally, fractal geometries increase the mechanical flexibility of electronic devices [165], which could be exploited to facilitate less obtrusive surgery and also to allow implants to conform to the curved surface at the back of the eye.

Each of the fractal's favorable properties can be optimized by tuning the scaling properties of the repeating patterns (as quantified by the fractal dimension, D) and the number of iterations of the patterns. As one example, Gentile et al. (2013) cultured fibroblasts (a type of connective tissue cell) on mountain-like roughened silicon surfaces with varying D and surface roughness and found the fibroblast

adhesion rates could be tuned [109]. As another example, by appropriately selecting the number of iterations for a given fractal, the transmission efficiency through fractal apertures at resonant wavelengths can be increased by over an order of magnitude compared to square apertures [190]. Or alternatively, etching fractal holes into silicon can greatly increase the absorption of light, providing more generated voltage per watt of incident radiation [191]. As yet another example, a fractal's capacitance per unit area can be significantly increased relative to a parallel plate capacitor by varying D, with higher D values giving larger capacitances [192]. Finally, Golestanirad et al. (2013) demonstrated that for implants designed to interface with neurons in the human arm, more efficient stimulation of peripheral nerves can be achieved by increasing the number of iterations in a fractal electrode [188].

In this paper, we tune D and the number of iterations of an H-tree electrode in order to quantify the degree to which fractal electrodes can generate superior neural stimulation. Whereas our recent simulations simply applied identical voltages to H-tree and square electrodes to investigate neural stimulation, here we extend the simulations to include the underlying photodiode. By modelling the whole operation of the pixel (photodiode and electrode), we show that a fractal design requires 74% less radiation to stimulate all of the neighboring neurons than the best square design. This has the important implication that the fractal-based implant operates significantly below the safety limit setting of how much radiation can be beamed into the eye, while the square-based implant operates just barely below the limit. Furthermore, we show that whereas the 20 μm fractal implant has the potential to deliver 20/80 visual acuity, the square suffers a dramatic decrease in perceived image quality due to stimulating 90% fewer neurons when operated at the same radiation levels as the fractal implant.

Methods

The retinal implant's operation is simulated in 3 separate stages in order to manage the computing power restraints. Firstly, photodiode simulations calculate the electrode voltages based on the incoming radiation intensity. These voltages then serve as the input parameters for the electrode simulations which model the associated electric field penetration into the fluid surrounding the neurons. Finally, neuron simulations then determine if these extracellular voltages are sufficient to stimulate the bipolar neurons and pass a signal downstream to the ganglion neurons. In order to overcome ionic screening by the fluid, it is necessary to have an oscillating electrode potential, which is achieved in today's implants by modulating the light entering the photodiode [36]. We focus on a sine wave modulation due to its universal applicability. Any repeating waveform, including the square-wave pulsed illumination used in today's implants [41] [36], can be generated as a sum of sine waves via a Fourier series. We also note that we exclude the interpulse rest period used in today's implants to minimize visual percept fading [32] [180]. Its inclusion post simulation would not impact our demonstration of the fractal electrode's superior operation. All model parameters are listed in Table 5.

Electrode Construction

We consider single 20 μm silicon photodiodes featuring an inner electrode (with either a square or fractal geometry) and an outer, grounded electrode (Fig. 30). Both electrodes are 250 nm tall and are composed of titanium nitride (TiN), a commonly used electrode material [32][34]. The silicon area (Fig. 30 blue) is 16 μm x 16 μm and is surrounded by a 500 nm wide insulating layer (Fig. 30 yellow). The bounding area

Parameter	**Value**	**Ref.**
TiN resistivity	$20 \times 10^{-6}\,\Omega$cm	[193]
TiN specific capacitance	$2.5\,\mathrm{mF/cm^2}$	[70]
TiN charge transfer resistance	$3 \times 10^5\,\Omega\mathrm{cm}^2$	[175]
Retina resistivity	$3500\,\Omega$cm	[28]
Neuron membrane capacitance	$1.1\,\mu\mathrm{F/cm^2}$	[179]
Neuron cytoplasmic resistance	$2.4 \times 10^4\,\Omega$cm	[179]
Photodiode sheet resistance	$20\,\Omega$/sq	[194]
Photodiode-TiN contact resistance	$2.4 \times 10^{-6}\,\Omega\mathrm{cm}^2$	[195]
Photodiode dark current density	1-1000 $\mathrm{nA/cm^2}$ *	[37]
Photodiode responsitivity	0.30 A/W	[37]

TABLE 5. List of model parameters and their associated values.
*A photodiode dark current density of $100\,\mathrm{nA/cm^2}$ is a typical photodiode used in retinal implants today. Future implants could stimulate neurons more efficiently by minimizing the dark current. Varying values of dark current density from 1-1000 $\mathrm{nA/cm^2}$ are considered in Section 2.2.

(Fig. 30 dashed white lines) for the square electrodes is varied between 50 - 200 $\mu\mathrm{m}^2$. The construction of the fractal electrodes is as follows.

Mathematically exact fractals can be constructed by scaling an initial seed pattern and then iterating the scaled pattern towards increasingly fine size scales. The scaling rate, L, is set by the number of new patterns created, N, and D, according to the equation

$$N = L^{-D} \tag{2.4}$$

where $1 \leq D \leq 2$. Throughout this paper we model branched H-tree fractal electrodes. Figure 29 illustrates H-tree fractals holding D fixed at 2.0 and increasing the iterations from 1 to 2 to 3, and also holding the iterations fixed at 3 and increasing D from 1.4 to 1.7. In general, the H-tree electrode becomes more space filling for increasing iterations and increasing D. Each fractal electrode features line widths

of 160 nm and a fixed bounding area of 15.4 μm x 15.2 μm. In total, 13 electrode geometries were studied: 4 square electrodes with areas of 50 μm^2, 100 μm^2, 150 μm^2, and 200 μm^2 and 9 fractal electrodes from each combination of D values of 1.4, 1.7, and 2.0 and iterations of 1, 2, and 3.

Photodiode operation

The MNA algorithm outlined above is used to characterize the current and voltage generated by the photodiode under illumination. The photodiode is first recreated as a 2-layer cubic mesh featuring TiN elecrode nodes in the top layer and semiconducting silicon nodes in the bottom layer (Fig. 42a). The node-to-node impedances feature an electrode resistance between metal nodes, a sheet resistance between semiconducting nodes, and a contact resistance between metal and semiconducting nodes. Under illumination, the photodiode current is modelled as an array of current sources (i.e., photocurrents generated from the incident radiation) in

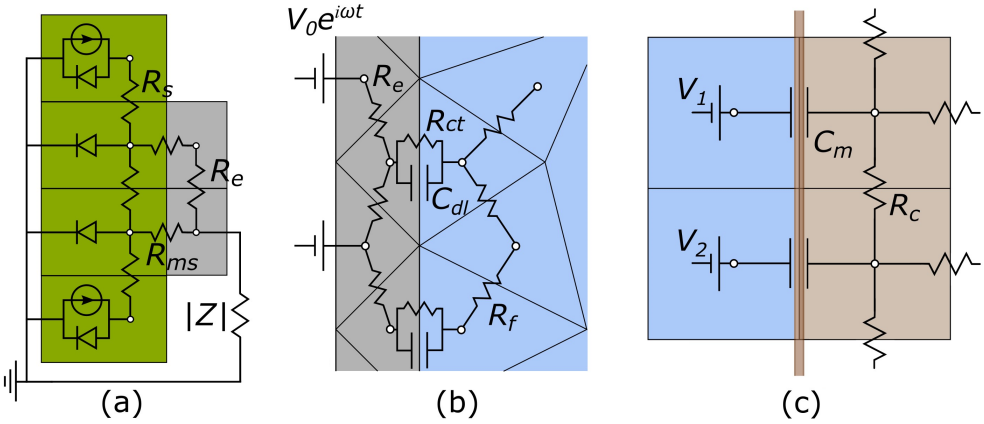

FIGURE 42. Photodiode implant equivalent circuit models. Two-dimensional representations of the equivalent circuit models used to calculate node voltages for each portion of the 3-step algorithm: (a) photodiode-electrode, (b) electrode-electrolytic fluid, and (c) electrolytic fluid-neuron. Nodes are labeled green (photodiode), grey (electrode), blue (electrolytic fluid), brown (neuron).

parallel with diodes (i.e., 'dark' currents) (Fig. 42a). Photocurrents are included only for nodes which are exposed to the radiation (i.e. not blocked by the inner electrode). The net current for node j, I_j^{app}, is given by an ideal diode under illumination according to

$$I_j^{app} = I_{sc} - I_{dark} = a(I_{rad}R - J_0(e^{V_j/V_T} - 1)) \tag{2.5}$$

where a is the node's top surface area, I_{sc} is the short-circuit current, I_{dark} the 'dark' reverse current, I_{rad} the irradiation, R the photodiode responsivity, and J_0 the dark current density at 0 V. The dark current density is estimated to $100\,\mathrm{nA/cm^2}$ by comparing to similar microphotodiode subretinal implants [26] [37]. The thermal voltage, $V_T = 0.0268$ V at the body's temperature of 310 K. V_j is the voltage at node j. Semiconducting nodes below the top-contact only feature a dark current. The only term included in V_{app} (Eq. 2.1) is setting the ground to 0 V. The MNA equation is solved iteratively using a global Newton method [196] [197] to determine the node voltages, $\vec{V}$, and the current flowing through the load impedance, I. Additionally, the open circuit voltage, V_{oc}, can be estimated by

$$V_{oc} = V_T \ln(\frac{I_{rad}RA_{pd}}{J_0 A_{tot}} + 1) \tag{2.6}$$

where A_{tot} is the total photodiode area and A_{pd} is the photodiode area not blocked by the electrode.

Electrode Operation

The MNA algorithm outlined in Section 2.1 is used for calculating the extracellular voltages generated by the electrodes. First, a $1\,\mathrm{mm^3}$ cubic domain containing the inner electrode, the outer grounded electrode, and the extracellular

space is meshed into a set of tetrahedral nodes using COMSOL. Next, an equivalent circuit model is created by exporting the mesh into custom C code which defines node-to-node impedances. The fluid-fluid nodes are resistive (R_f) while the fluid-electrode nodes feature a capacitor (C_{dl}) and resistor (R_{ct}) in parallel (Fig. 42b) [63]. The fluid resistivity is taken to be $3500\,\Omega$cm, that measured just above the photoreceptor layer in macques monkeys [28]. An oscillating voltage, $V = V_0 e^{2\pi i f t}$, (where the value of V_0 is inputted from the photodiode simulations) is applied to the inner electrode while the outer electrode is held at 0 V. Due to the oscillating voltage, time derivatives in current crossing the fluid-electrode interface, $C_{dl} d(V_e - V_f)/dt$, where V_e and V_f are electrode and fluid node voltages, respectively, lead to a factor of $2\pi i f$ being placed into the appropriate position of the G conductance matrix (Equation 2.1). Furthermore, since every node oscillates at frequency f, $e^{2\pi i f t}$ terms can be factored out of the MNA equation. We note that each node voltage is not necessarily in phase due to the capacitive and resistive impedance elements. The remaining boundary conditions are set to be insulating for the plane in which the electrode is located, and 0 V at the other 5 faces of the cubic domain. Having established the equivalent circuit model along with the boundary conditions, Equation (2.1) can be solved for the n complex valued node voltages and m complex currents through the boundary condition nodes. The load impedance magnitude, $|Z|$, (which is set by the network of R_f, C_{dl}, and R_{ct} components) can also be calculated by

$$|Z| = |V|/|I| \tag{2.7}$$

where $|I|$ is the current leaving the inner electrode. Additionally, we calculate the charge density, Q_{ph}, at each node delivered on the electrode surface per positive phase of voltage by

$$Q_{ph} = \int_0^{\frac{1}{2f}} dt C_{dl} |\frac{d(V_e - V_f)}{dt}| = 2C_{dl}|V_e - V_f| \tag{2.8}$$

Neuron Stimulation

The extracellular voltages, V_f, calculated in Section 2.2 induce a change in the membrane potential, $\Delta V_m = \Delta V_i - \Delta V_o$, in the bipolar neurons located near the electrode, where ΔV_i is the change in internal potential of the neuron and ΔV_o is the change in outside potential. In turn, these bipolar neurons pass their signal downstream to retinal ganglion cells when ΔV_m reaches a minimum of 15 mV at the bipolar neuron's soma [178]. Here we model passive bipolar neurons. We do not include active voltage-gated ion channels because, although calcium ion channels remain open at the stimulating frequencies our implants operate at (1 kHz) [43], the calcium current through the ion channels is negligible for ΔV_m values of 15 mV or less [44]. Thus, the exclusion of active channels does not affect our results.

Our model bipolar neurons are 100 μm long with a 10 μm soma centered 30 μm above the electrode surface [60][59]. In our simulations, each neuron features a cubic mesh constructed in MATLAB. Passive rod bipolar neurons are quantified by a membrane capacitance of 1.1 μF/cm^2 in parallel with a membrane resistance of $2.4 \times 10^4\,\Omega$cm^2, along with an internal cytoplasmic resistivity of 130 Ωcm [179]. For the applied stimulation frequencies used here (1 kHz), the resistive impedance is more than 2 orders of magnitude higher than the capacitive impedance. We therefore ignore the resistive component and create an equivalent circuit model containing solely membrane capacitances and internal cytoplasmic resistances (Fig. 42b). The real and imaginary parts of the extracellular voltages obtained in Section 2.2 are mapped onto the outside of the neuron's membrane and serve as a set of applied voltage sources,

$\vec{V}^{app}$ in Equation (2.1). The MNA equation is then solved to obtain the neuron's internal voltage at each node.

Results

Photodiode Performance

We first consider the load impedance, $|Z|$, because this will determine how close the photodiode operates to open or closed-circuit. The load impedance for the square electrode is found to decrease with increasing electrode size (Fig. 43). This is expected because the geometric contribution to the load impedance is inversely proportional to the inner electrode's effective surface area and directly proportional to the distance between the inner and outer electrodes [7]. The fractal electrode reduces its impedance relative to the square by increasing its effective surface area (by maximizing the surface area via the large number of branch sidewalls). This leads to a general trend of decreasing impedance for increasing D value and increasing iterations (Fig. 43).

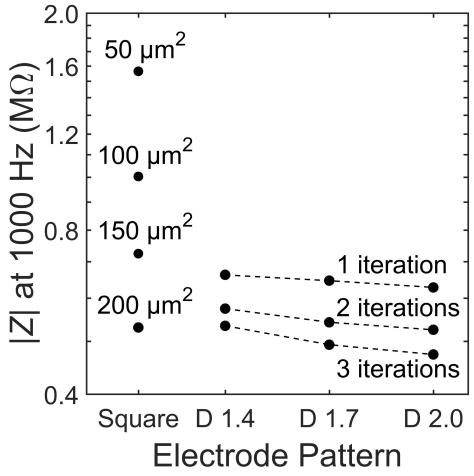

FIGURE 43. Load impedance for square and fractal electrodes.
Load impedance, $|Z|$, for each of the 13 electrode geometries. Dashed lines depict constant iteration with varying D for fractal electrodes.

Figures 44a-c show the IV curves for photodiodes with square and fractal electrode geometries under an illumination of $I_{rad} = 10\,\mathrm{mW/mm^2}$. Each electrode exhibits an open-circuit voltage of ∼0.40 V and a short-circuit voltage proportional to the exposed photodiode area. In a conventional solar cell, the load impedance would be chosen to maximize the power generated. However, here each photodiode has a load impedance set by the electrode geometry. The black dot on each trace in Figure 44a-c shows the operating point on the IV curve set by the impedances reported in Figure 43.

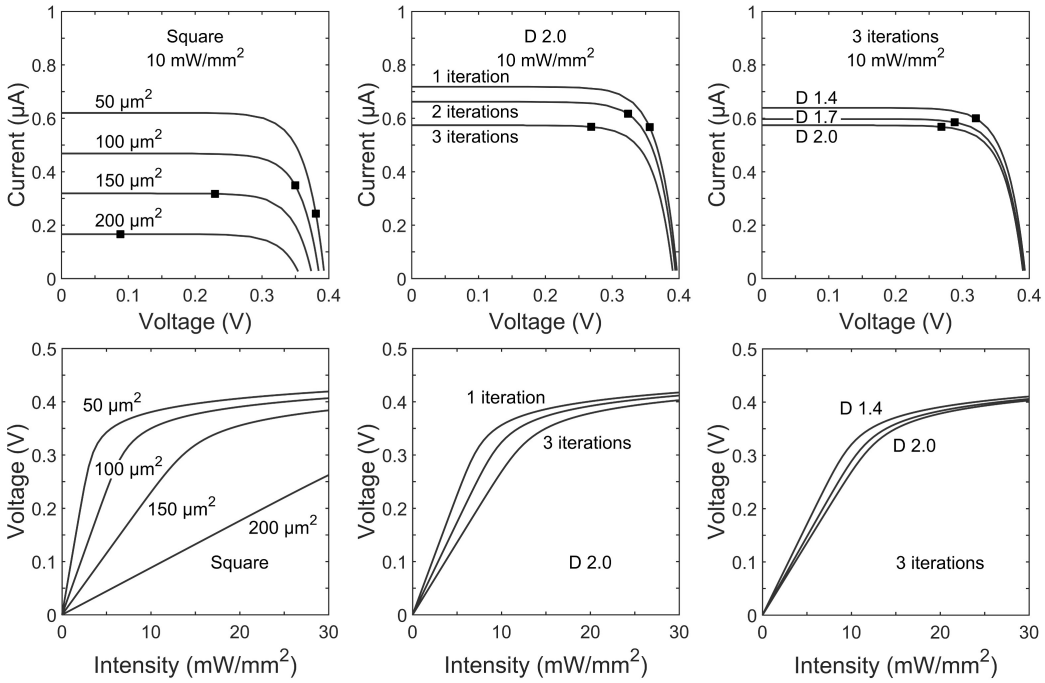

FIGURE 44. IV curves and voltage-intensity curves for square and fractal electrodes. Top row: IV curves for photodiodes with (a) square, (b) 1 to 3 iteration D=2.0 H-trees, and (c) D=1.4, 1.7, or 2.0 H-trees with 3 iterations inner electrode geometries. The black dot on each trace indicates the load impedance for that electrode operating at 1 kHz stimulation frequency. Bottom row: Voltage generated for varying incident irradiation on (d) square, (e) 1 to 3 iteration D=2.0 H-trees, and (f) D=1.4, 1.7, or 2.0 H-trees with 3 iterations inner electrode geometries.

The voltages generated by each electrode geometry as a function of irradiation display several common characteristics (Fig. 44d-f). Firstly, at low voltages the slope of each trace is given by $\Delta V/\Delta I_{rad} = R|Z|A_{pd}$, where A_{pd} is the unblocked photodiode area. The electrodes with smaller covering areas have both large $|Z|$ and A_{pd} and therefore generate relatively high voltages at the lower intensities. Secondly, as the voltage begins to approach the open circuit voltage, increasing illumination intensity provides minimal increases in the electrode voltage.

Extracellular fields

The results of Section 2.2 highlight the importance of electrode geometry when determining the voltage generated for a given illumination. However, electrode geometry also influences how the field from this voltage extends into the extracellular liquid and this can lead to competing considerations. For instance, Figs. 45a and 45d show the effect of increasing a square electrode's area from $100\,\mu\text{m}^2$ to $150\,\mu\text{m}^2$. As expected from the decrease in $|Z|$ and A_{pd}, the larger electrode's voltage decreases significantly and the field does not therefore extend as far vertically into the liquid as the smaller electrode's field. However, the field from the larger electrode has the advantage of extending further horizontally within the pixel. An inevitable consequence of the square design therefore is that fields that extend far vertically do not extend far horizontally and vice versa.

The fractal design offers a potential solution for optimizing this competition. The fractal electrode generates high voltages for a given illumination (Fig. 44). Furthermore, its maximal capacitance (due to the large surface area generated by the branch sidewalls) allows a large amount of charge to reside on the electrode and this generates a large field for a given applied voltage, which will penetrate far vertically

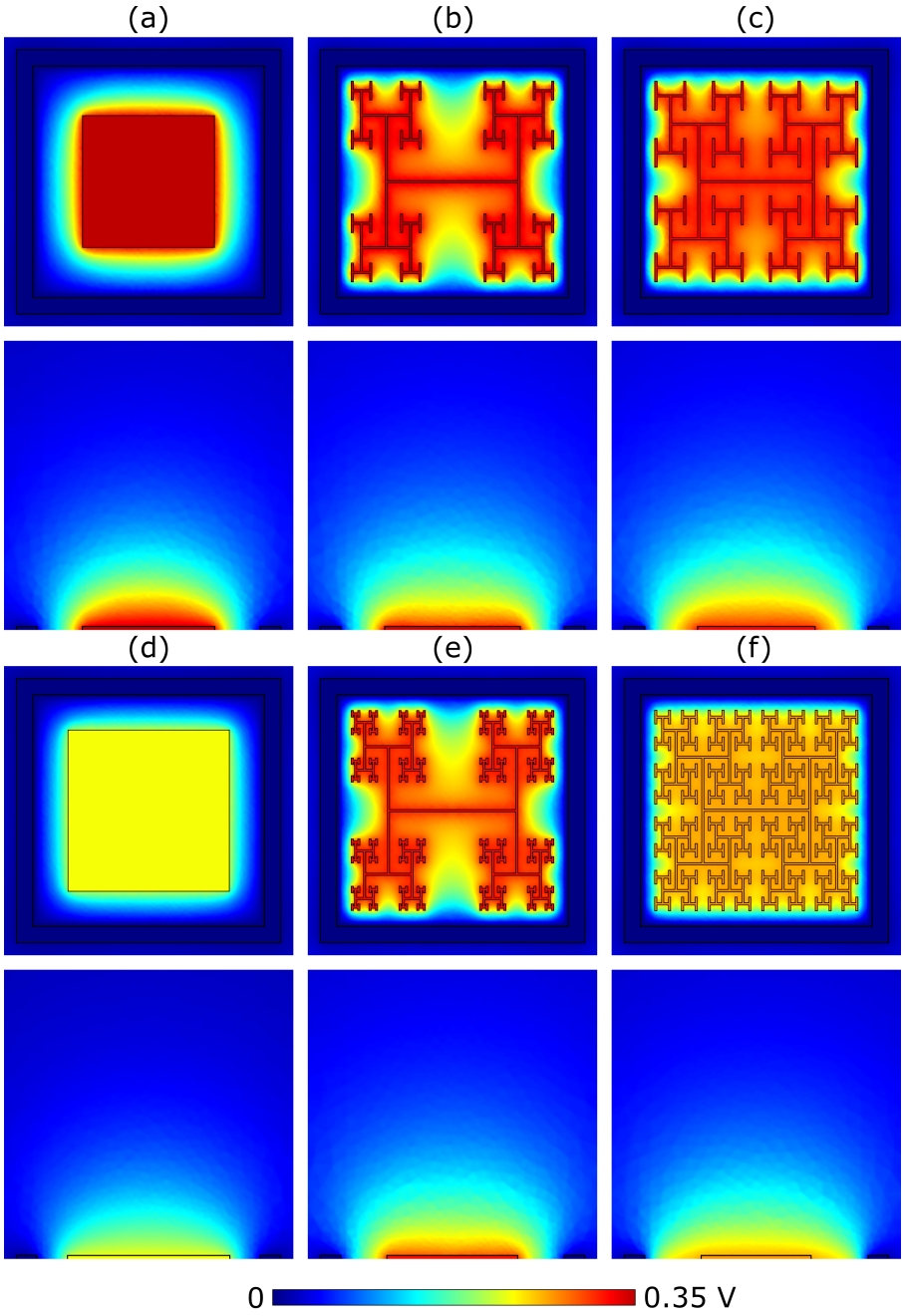

FIGURE 45. Extracellular voltages due to 10 mW/mm^2 incident irradiation. Magnitude of extracellular voltages under 10 mW/mm^2 incident irradiation at 1 kHz stimulating frequency delivered by square electrodes of size (a) 100 μm^2 and (d) 150 μm^2, and D=1.4 H-trees with (b) 2 and (e) 3 iterations, and D=2.0 H-trees with (c) 2 and (f) 3 iterations. Rows 1 and 3 show horizontal slices at the top surface of the inner electrode, while rows 2 and 4 show vertical slices through the center of the electrode.

into the liquid. Because the electrode spreads further laterally than a square electrode for the same covering area, the fractal electrode's field will also extend far horizontally. However, the presence of the gaps in the fractal design needs to be taken into account. Figs. 45b and 45e show the fields for the D=1.4 electrode; both the 2 and 3 iteration electrodes feature large gaps which reduce the extracellular voltage in the central region. For the D=2.0 fractals shown in Fig. 45c and 45f, increasing the number of iterations from 2 to 3 reduces the voltage but the field spreads out relatively uniformly across the entire pixel. Given that larger extracellular fields generally induce large depolarizations, ΔV_m, of the bipolar neurons, it is clear from the above that careful geometric optimization will be required to supply a large voltage which extends into the most extracellular space.

The stimulation efficiency for each design is determined by measuring ΔV_m, for a patch of 9 bipolar neurons directly above each electrode. Figure 46 depicts ΔV_m for a patch of 4 of the 9 neighboring bipolar neurons above electrodes under equivalent illuminations of 10 mW/mm^2. Because the 150 μm^2 square electrode (Fig. 46a) blocks a larger percentage of the underlying photodiode and therefore has a lower voltage on the inner electrode, the neurons above the square depolarize less compared to the 2 iteration D=1.4 and D=2.0 H-trees (Fig. 46b and 46c). Additionally, the fractal electrode's D value influences the field distribution in the extracellular space, leading to varying neural depolarizations. For instance, although the voltage on the 2 iteration D=1.4 H-tree is slightly larger than the voltage on the 2 iteration D=2.0 H-tree (0.38 V versus 0.36 V), the depolarizations are larger for neurons above the 2 iteration D=2.0 H-tree (Fig. 46b and 46c).

To quantify the stimulation efficiency, we define the electrode threshold stimulating voltage, V_{thresh}, as the electrode voltage at which all 9 neighboring bipolar

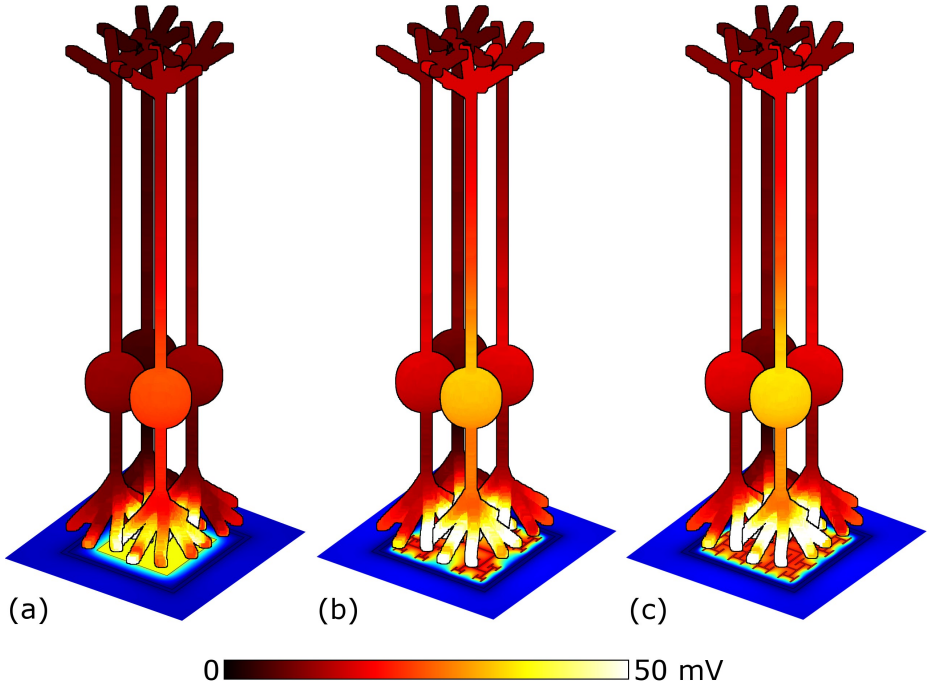

FIGURE 46. Membrane depolarizations due to 10 mW/mm^2 incident irradiation. Peak membrane depolarizations achieved during a voltage oscillation for a patch of 4 bipolar neurons above the (a) 150 μm^2 square, (b) 2 iteration D=1.4 fractal, and (c) 2 iteration D=2.0 fractal electrodes. The front most neuron in each image is centered above the pixel. Bipolar neurons are 100 μm tall and images are drawn to scale. The remaining 5 of the 9 neighboring neurons are not shown for clarity.

neurons reach a somatic depolarization of $\Delta V_m = 15$ mV. Previous experiments show this 15 mV condition results in stimulation of the downstream ganglion neurons [178]. For square electrodes, increasing the electrode area reduces V_{thresh} due to an increase in capacitance. Likewise, increasing the capacitance for fractal electrodes either by increasing the number of iterations or increasing the D value leads a to lower V_{thresh} (Fig. 47a). However, as discussed in Section 2.2, increasing the electrode's covering area also reduces the voltage generated on the inner electrode. Therefore, efficient stimulation requires a careful optimization of supplying enough voltage from the photodiode and maintaining a low V_{thresh}.

Across all of the electrode patterns, the 2 iteration D=2.0 fractal provides the best balance between these 2 competing factors (Fig. 47). In particular, the incident radiation required to stimulate all neighboring bipolar neurons is 74% less for the 2 iteration D=2.0 fractal than for the best square electrode of 200 μm^2. We note that at their threshold voltages, the maximum surface charge density, Q_{ph}, of the optimized electrodes are Q_{ph} = 0.67 mC/cm^2 for the 200 μm^2 square electrode and Q_{ph} = 0.93 mC/cm^2 for the 2 iteration D=2.0 H-tree. These charge densities are less

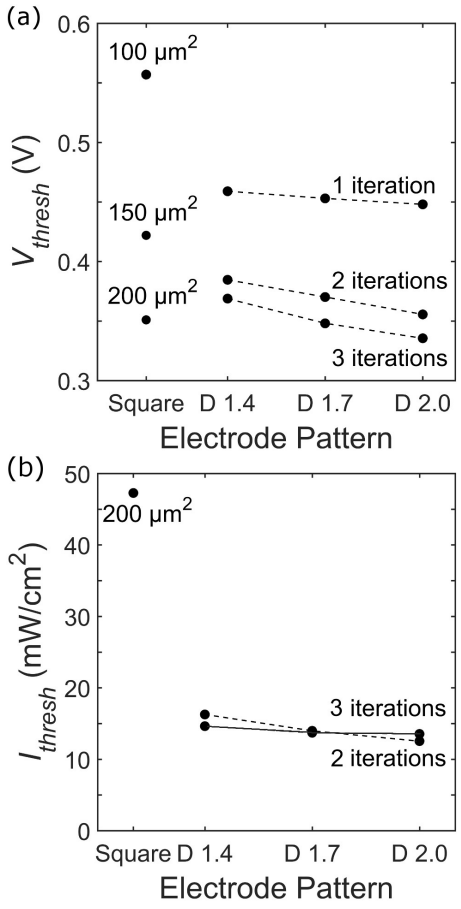

FIGURE 47. Threshold voltages and irradiances required for stimulation. Threshold (a) electrode voltages, V_{thresh}, and (b) irradiant intensities, I_{thresh}, necessary to induce ΔV_m = 15 mV somatic depolarization in all 9 bipolar neurons above each electrode. The dashed line connects 2 iteration fractals and the solid line connects the 3 iteration fractals.

than the $1\,\mathrm{mC/cm^2}$ safety limit for TiN electrodes based on the charge densities that induce hydrolysis [66].

Stimulation Frequency

So far, we have considered stimulating pulses operating at a frequency of 1 kHz. However, conventional subretinal implants being developed today use stimulating frequencies ranging from 250 Hz - 2 kHz [32][41][36]. In order to verify the fractal maintains a lower threshold irradiation at lower stimulating frequencies than 1 kHz, we repeated the above analysis for the $150\,\mu\mathrm{m}^2$ square, the $200\,\mu\mathrm{m}^2$, and the 2 iteration D=2.0 fractal at a stimulating frequency of 250 Hz.

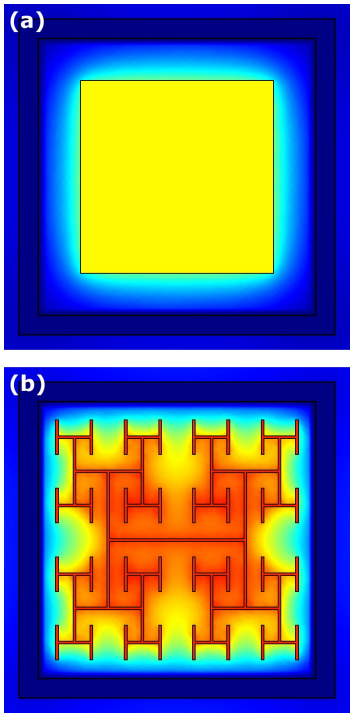

FIGURE 48. Extracellular voltages at 250 Hz.
Magnitude of extracellular voltages under $10\,\mathrm{mW/mm^2}$ incident irradiation at 250 Hz stimulating frequency delivered by (a) $150\,\mu\mathrm{m}^2$ square and (b) 2 iteration D=2.0 H-tree electrodes.

First, lowering the stimulating frequency causes a rise in the load impedance, $|Z|$, for each geometry due to an increase in capacitive impedance at the electrode-electrolyte interface. This increased $|Z|$ leads to a larger voltage generated on the inner electrode (i.e., the operating point on the IV curve shifts to a higher voltage). For example, under $10\,\mathrm{mW/mm^2}$ illumination, reducing the frequency from 1 kHz to 250 Hz causes an increase in the inner electrode voltage from 0.09 V to 0.11 V for the $200\,\mu\mathrm{m}^2$ and from 0.34 V to 0.36 V for the 2 iteration D=2.0 fractal. Simultaneously though, the increased impedance leads to a smaller spreading in the extracellular field generated by each electrode (Fig. 48). Additionally, the lower frequency causes smaller depolarizations in the bipolar neurons due to a higher capacitive membrane impedance.

Combining all of these factors, we find the threshold irradiations, I_{thresh}, necessary to depolarize all 9 surrounding neurons at 250 Hz are $90\,\mathrm{mW/mm^2}$ for the $150\,\mu\mathrm{m}^2$ square, $42\,\mathrm{mW/mm^2}$ for the $200\,\mu\mathrm{m}^2$ square, and $15\,\mathrm{mW/mm^2}$ for the 3 iteration D=2.0 fractal. Therefore, lowering the stimulating frequency from 1 kHz to 250 kHz caused a reduction in I_{thresh} for the $200\,\mu\mathrm{m}^2$ square and an increase in I_{thresh} for the 2 iteration D=2.0 fractal. However, the fractal implant still requires 64% less radiation intensity to stimulate all surrounding neurons than the best square design.

Discussion

Irradiance Efficiencies

We have shown that by optimizing the fractal's iterations and D values, the threshold irradiance can be reduced by 74% compared to the best square design. In particular, we have shown, for a $20\,\mu\mathrm{m}$ pixel with typical photodiode and electrode properties found in today's retinal implants, that I_{thresh} for the optimized fractal, 2

iteration D=2.0 H-tree, is 12 mW/mm^2 while for the best square, 200 μm^2, I_{thresh} is 47 mW/mm^2 when operated at f = 1 kHz. For reference, the irradiance of direct sunlight at the Earth's surface is 1 mW/mm^2.

Because today's implants, including our fractal designs, require more radiation than that supplied by direct sunlight, pulses of infrared (IR) radiation are repeatedly beamed into implants [41][36]. For 20 μm pixels, our fractal designs would therefore require 74% less power beamed in than the same sized pixel featuring a square design. An alternative approach to reducing power requirements is to increase pixel size to collect more radiation. For example, some conventional implants beam in 4 mW/mm^2 to 70 μm pixels [36]. However, increases in pixel size reduce visual acuity (see Section 2.2).

Intensity Safety Limits

The light intensities which can be safely beamed into the eye without overheating the retina are set by the maximum permissible exposure limits [198]. These intensities are labelled for single pulses of light as I^{sp}_{safety}, and for pulses which repeat indefinitely at some given frequency, I^{av}_{safety}. In today's implants, pulses of infrared (IR) radiation are repeatedly beamed into the implant [41][36]. IR is used because the cornea and lens are transparent to IR, the silicon photodiode responsivity is maximal in the IR, and the maximum permissible exposure limits are higher for IR than for visible. Assuming IR light of an identical wavelength to that used in today's implants is beamed into the square and fractal photodiodes considered in this paper, $I^{sp}_{safety} = 285 f^{0.25}$ and I^{av}_{safety} = 5.2 mW/mm^2 [36]. For single pulses of frequency f = 1 kHz, the optimized fractal electrode (2 iteration D=2.0) is a factor of 24 below I^{sp}_{safety} while the best square (200 μm^2) is only a factor of 6 below.

For repeated stimulation by sinusoidal pulses as considered here, the average threshold intensity is $I_{thresh}^{av} = \frac{F}{\pi f} I_{thresh}$ where F is the interpulse frequency. Current implants operate at an interpulse frequency up to $F = 20$ Hz [32][41]. However, since the critical flicker-fusion rate (the rate at which 95% of people cannot perceive an image as flickering) is 80 Hz [199], future implants could aim to operate at a higher frequency of $F = 80$ Hz. At $f = 250$ Hz and $F = 80$ Hz, $I_{thresh}^{av} = 4.3\,\mathrm{mW/mm^2}$ for the $200\,\mu\mathrm{m}^2$ square and $I_{thresh}^{av} = 1.5\,\mathrm{mW/mm^2}$ for the 2 iteration D=2.0 H-tree. While both the square and fractal have $I_{thresh}^{av} < I_{safety}^{av}$, the square is quite close to surpassing the safety limit. The reduction in threshold intensity afforded by the 2 iteration D=2.0 H-tree therefore ensures a long-term safe operation of the implant.

Visual Acuity

The fractal inner electrode incorporated into a $20\,\mu$m pixel is capable of stimulating all the surrounding bipolar neurons within the maximum permissible exposure safety limits. The visual acuity associated with a $20\,\mu$m pixel is calculated as follows. Visual acuity is inversely related to the number of arcminutes at which an object can be resolved. In natural vision, 20/20 acuity equates to resolving 1 arcmin, corresponding to a $5\,\mu$m pixel at the retina. For electronically restored vision with a $20\,\mu$m, as considered here, the maximum restored acuity is therefore 4 times reduced from 20/20 vision, corresponding to 20/80 vision. In reality, the restored acuity may be worse than this upper limit due to electrical crosstalk (whereby the voltage on one electrode pixel stimulates neurons above neighboring pixels) [7] or glia scarring [51]. However, we have previously demonstrated that electrical crosstalk for a $20\,\mu$m fractal electrode does not stimulate the neurons above a neighboring pixel [7] and we expect the fractal electrode will reduce glia scarring since glia scarring is reduced on textured surfaces [58] [40]. We note that when operated at the same illumination

level of $12\,\mathrm{mW/mm^2}$ as the fractal electrode, the best square design only stimulates 1 of the 9 neurons above the $20\,\mu$m pixel. This reduced stimulation will generate fewer spiking events per second in the downstream ganglion neurons, which will reduce the perceived image quality [168].

Optics

Here we have considered a simplified pixel count model of light transmission into the silicon. This pixel model is based on ray optics, in which light either reflects off the electrode surface or passes through the gaps. This pixel model is valid when $a \gg \lambda$, where a is the gap size and λ is the wavelength. In reality, because the electrode features gap sizes which are either the same order of magnitude as the wavelength of light ($a \sim \lambda$) or smaller ($a < \lambda$), one of two different optical regimes will dominate. In the diffraction regime, where $a \ll \lambda$, light through subwavelength holes transmits only a fraction proportional to $(a/\lambda)^2$ of that predicted from ray optics [200]. This leads to more space filling fractals (i.e., smaller a) transmitting less radiation into the photodiode. In the surface plasmon regime, when $a \sim \lambda$, fractals have been shown to exhibit extraordinary transmission of light, i.e., the radiation entering the photodiode is greater than that predicted from a simple pixel count [162][161]. By optimizing the D value and number of iterations, the intensity could be maximized and the transmitted wavelength (i.e. color) could be tuned [163][164]. Because we cannot model the full 3-dimensional optics for complex fractal geometries, we instead chose the 'pixel count' model which is intermediary to the diffraction and surface plasmon regimes. Future experimental measurements aim to investigate which regime dominates for our fractal electrodes.

Open circuit voltage

We modelled the silicon microphotodiode using an open-circuit voltage, $V_{oc} \sim$ 0.4 V, similar to devices previously reported in the literature [26][37]. In theory though, the V_{oc} silicon voltage can reach as high as 0.6 V. A higher V_{oc} leads to a larger range of irradiation in which $\Delta V/\Delta I_{rad}$ is linear (Fig. 44), thereby reducing the required intensity necessary to induce the 15 mV depolarization in neighboring neurons. For instance, at a larger $V_{oc} \sim 0.5$ V (corresponding to a dark current density $J_0 \sim 1\,\mathrm{nA/cm^2}$), the I_{thresh} for the optimal fractal electrode drops to $10\,\mathrm{mW/mm^2}$ compared to $12\,\mathrm{mW/mm^2}$ for $V_{oc} \sim 0.4$ V (Fig. 49). Interestingly though, the 2 iteration D=1.4 geometry now corresponds to the lowest threshold irradiation as compared to the 2 iteration D=2.0 at $V_{oc} \sim 0.4$ V ($J_0 \sim 100\,\mathrm{nA/cm^2}$).

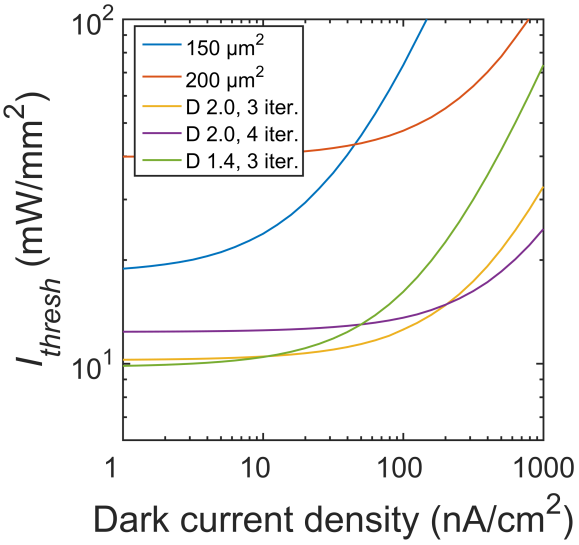

FIGURE 49. Threshold irradiations for varying dark current densities. Photodiodes used in subretinal implants today operate at a dark current density of $100\,\mathrm{nA/cm^2}$ (equating to $V_{oc} \sim 0.4$ V). At this J_0, the D=2.0 H-tree with 2 iterations is the optimal geometry. Reducing the dark current density to $1\,\mathrm{nA/cm^2}$ ($V_{oc} \sim 0.5$ V) would lead to the D=1.4 H-tree with 2 iterations being the optimal geometry.

Conclusions

Branched fractal electrodes best balance a number of competing requirements necessary for efficient neural stimulation from photodiode implants. (1) The gaps between the branches transmit large amounts of light into the underlying photodiode, thereby generating high electrode voltages. (2) The sidewalls of the branches create a large surface area and therefore a high electrode capacitance. For a given voltage, the fractal electrode then holds a large amount of charge and the electric field generated by this charge extends vertically far into the extracellular space. (3) The gaps ensure that, for a given covering area, the fractal has a large bounding area. By carefully selecting the optimal D and number of iterations, the field penetrates the gaps and ensures a uniform field that extends far laterally. Combined, the above factors ensure a large uniform field that penetrates a maximal volume of extracellular space.

Consequently, the 20 μm fractal implant stimulates all of the surrounding bipolar neurons using 74% less irradiation compared to the square. In addition to an improved efficiency, the fractal's decreased threshold irradiation holds important consequences for the safe operation of future implants. For long-term continuous operation of implants, the square is just barely below the maximum permissible exposure limit while the fractal is significantly below. Moreover, for equivalent irradiations of 12 mW/mm^2 illuminating the best optimized square and fractals, the fractal stimulates $\sim$90% more neurons. Thus, whereas the 20 μm fractal implant has the potential to deliver 20/80 vision acuity, the square suffers a significant decrease in perceived image quality. When the performance factors reported here are coupled with potentially beneficial adhesive, optical, and mechanical properties, it is clear that fractal electrodes have the potential to dramatically improve the restored visual acuity from subretinal implants.

Tissue Heating from Subretinal Implant Electrodes

Before adopting the H-tree geometry, it is important to verify that the stimulating electrodes do not overheat the surrounding retinal tissue to unsafe levels. Previous research has shown retinal temperature increases of up to 2 °C are safely tolerated from heat sources placed in the vitreous cavity [201]. However, if the heater dissapated 50 mW or more directly in the retina visible whitening of the retina occurred. Gosalia et al. [202] showed that a 4 mm x 4 mm x 0.5 mm chip in the retina causes a 0.10 °C temperature rise for 12.4 mW dissapated heat and a 0.57 °C temperature rise for 49.6 mW dissapated heat. A quick back of the envelope calculation will show that an individual 20 μm microelectrode biased to 0.2 V can not heat up the majority of surrounding tissue to anywhere near even 0.5 °C. However, it is not immediately obvious if 'hot spots' occur near the thin branches on the H-tree. This section develops a joule heating model to answer that question (Fig. 50).

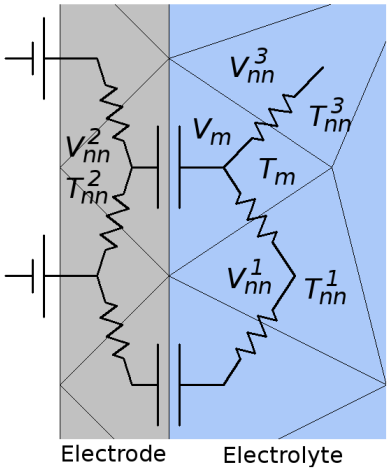

FIGURE 50. Equivalent circuit model for tissue heating.
Finite element model used to solve temperature change in the extracellular region around an electrode. Node voltages are determined first using MNA algorithm described previously. The nn subscripts denote nearest neighbors to node m.

Three terms contribute to the heat rise around the electrode: (1) resistive Joule heating, Q_J, (2) internal temperature rise through specific heat, Q_{rise}, and (3) Fourier heat conduction between nodes, Q_{exit}. Two other terms often show up in the bioheat equation. One for metabolic heat production and one for capillary removal of heat through blood flow. However, numerical simulations of a 5 mm x 5 mm retinal chip determined that neither term is significant for less than 50 mW of dissipated heat [203]. For a time step, Δt, the three terms can be written down by

$$\begin{aligned} Q_J &= I^2 R \Delta t \\ Q_{rise} &= \rho V C \Delta_t T \\ Q_{exit} &= -\Delta t \sum_{nn} \frac{k_{nn} A}{\Delta x} \Delta_x T \end{aligned} \tag{2.9}$$

where R is node-to-node resistance, I current between two nodes, $\rho_{ret} = 1039\,\mathrm{kg/m^3}$ retina density [204], $\rho_{TiN} = 5400\,\mathrm{kg/m^3}$, $C_{ret} = 3680\,\mathrm{J/kg \cdot K}$ the retina's specific heat [204], $C_{TiN} = 604\,\mathrm{J/kg \cdot K}$ the specific heat of TiN [193], A the area between two nodes, Δx the distance between neighboring node centroids, V the volume of a node, and nn is an index over all neighboring nodes. Thermal conductivities are $k_{ret} = 0.565\,\mathrm{W/m \cdot K}$ for the retina [204], $k_{TiN} = 28.8\,\mathrm{W/m \cdot K}$ for TiN [193], and the interfacial conductivity, $k_{int} = 0.552\,\mathrm{W/m \cdot K}$, since thermal conductances add like resistors in parallel. For Q_{rise}, $\Delta_t T$ is a change in temperature over time. While in Q_{exit}, $\Delta_x T$ is a change of temperature between neighboring nodes. Fourier's law of heat conduction is typically written in the differential form, $q_{exit} = -k \nabla T$, where q_{exit} has units of $\mathrm{W/m^2}$. For the discrete element case, the differential form translates to that shown in equation (2.9).

Each term in equation (2.9) is straightforward with the exception of the current between two nodes, I. Recall the complex potential at node m is $V_m e^{i\omega t}$. Which can be rewritten as $|V_m|e^{i(\omega t+\phi_m)}$ where

$$\begin{aligned} |V_m| &= \sqrt{\mathrm{Re}(V_m)^2 + \mathrm{Im}(V_m)^2} \\ \phi_m &= \arctan \frac{\mathrm{Re}(V_m)}{\mathrm{Im}(V_m)} \end{aligned} \tag{2.10}$$

Since only the real part of the current contributes to Joule heating, the current between node m and a nearest neighber node nn is

$$I = \mathrm{Re}(\Delta V)/R = [V_m \cos(\omega t + \phi_m) - V_{nn} \cos(\omega t + \phi_{nn})]/R \tag{2.11}$$

Finally, conservation of energy at each node is

$$Q_{rise} - Q_{exit} = Q_J \tag{2.12}$$

Which can be written down as a matrix equation

$$\rho V C T_m + \Delta t \sum_{nn} \frac{kA}{\Delta x}(T_m - T_{nn}) = I^2 R \Delta t + \rho V C T_{m,init} \tag{2.13}$$

and solved iteratively for T_m. $T_{m,init}$ is originally set to 310 K at each node. On subsequent time step iterations, $T_{m,init}$ is set to the temperature distribution from the previous iteration.

Simulations reveal that although tissue heating surrounding fractal electrodes is higher than the square, it is still well within safety limits (Fig. 51 and Fig. 52).

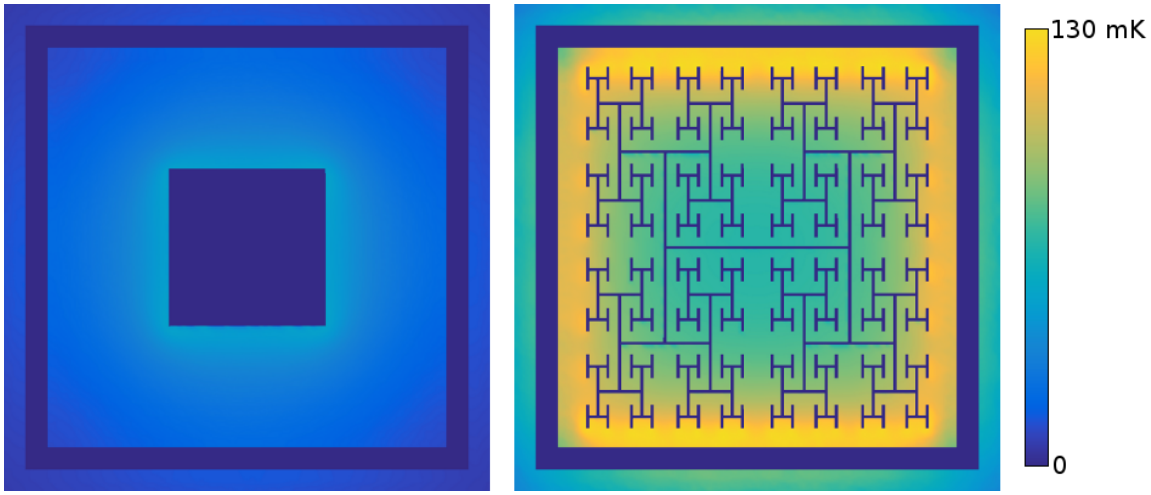

FIGURE 51. Temperature increases during one stimulation pulse.
Temperature rise, ΔT, surrounding 20 μm square and a fractal electrodes after 1 ms of 1 kHz, 1.5 V applied potentials. The initial temperature is 310 K.

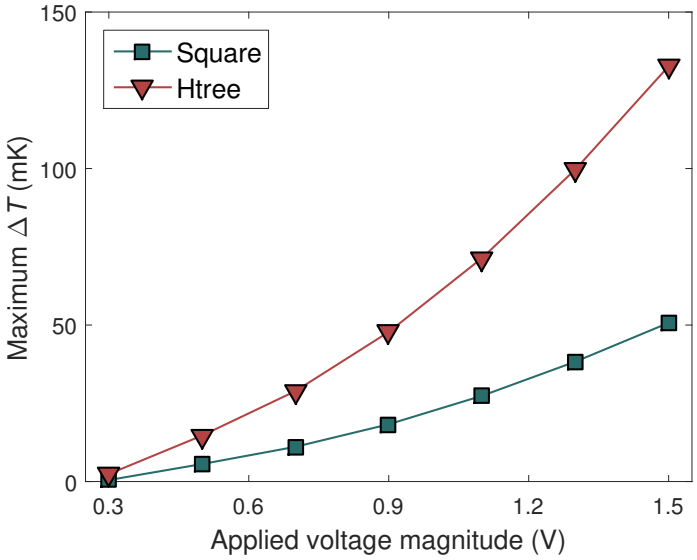

FIGURE 52. Temperature increase versus applied voltage.
Maximum temperature increase for one phase of 1 kHz applied potentials. For all voltages within the safe-operating water window of TiN, the maximum temperature increase is less than the suggested safety limit of 0.5 °C.

CHAPTER III

BIOCOMPATIBILITY OF CARBON NANOTUBES FOR RETINAL IMPLANT ELECTRODES

The first section, *Retinal cell cultures on unfunctionalized vertically aligned carbon nanotubes*, contains co-authored work currently in publication [9]. I (WJW) am the first author. The co-authors listed in order are Saba Moslehi (SM), Kara M. Zappitelli (KMZ), Julian H. Smith (JHS), David J. Miller (DJM), Julie E. Chouinard (JEC), Stephen L. Golledge (SLG), Richard P. Taylor (RPT), Maria-Thereza Perez (MTP), and Benjamín Alemán. SM and DJM fabricated the CNTs. JEC and SLG performed XPS analysis. WJW, KMZ, and JHS performed the cell cultures. WJW and JHS analyzed the data. WJW, SLG, MTP, and BA prepared the manuscript. RPT, MTP, and BA are PIs on this project.

It is widely established that micro and nano topographies of neural interfaces influence cell adhesion, differentiation, and neurite outgrowth (see Section 1.7). By appropriately optimizing the topography, device longevity, stimulation efficiency, recording quality, and/or neural regeneration can be improved. This topographical optimization is typically achieved by varying Euclidean geometrical parameters such as row width, device curvature, or r.m.s. surface roughness. However, the geometry of neurons is fractal [170] [169]. In particular, the branching patterns of neuron axons and dendrites repeat at multiple size scales. In this chapter, we outline preliminary experiments investigating the following hypotheses: do fractal interfaces (1) increase neuron adhesion and neurite outgrowth and (2) reduce glia scarring?

Retinal cell cultures containing neurons and glia are examined on carbon nanotubes (CNTs). CNTs are an ideal electrode material with favorable electrical,

chemical, mechanical, and morphological properties (see Section 1.8). The CNT fractals were patterned with feature sizes of 50 μm or larger.

Although our ultimate goal is to examine fractal topographies, it is essential to first ensure that the surface chemistry is favorable for neurons. Therefore, the bulk of this chapter is dedicated to identifying surface treatments for CNTs. At the end of the chapter, we briefly explore preliminary data for in vitro retinal cell cultures on Euclidean and fractal interfaces.

Retinal Cell Cultures on Unfunctionalized Vertically Aligned Carbon Nanotubes

Photoreceptor degeneration (i.e. loss of rods and cones) in the retina can lead to blindness in patients with retinitis pigmentosa or age-related macular degeneration. Retinal implants are currently restoring vision to these patients by electronically stimulating the remaining healthy portions of the retina. However, the restored visual acuity (VA) remains significantly below the acuity required to read text or recognize faces [21] [32]. One key factor for this low VA is poor signal fidelity and transmission during neural stimulation, which is often dictated by the electrode-neuron interface. In order to achieve a higher VA, it is critical to improve the electrode materials at the interface [205] [206].

Electrode materials must meet a demanding set of electrical, chemical, mechanical, and morphological requirements all while remaining biocompatible. (1) Electrically, electrodes aim to maximize the charge injection limit, which enables sufficiently large currents to be safely injected into the tissue through small electrode areas [62]. Charge injection occurs through either charging and discharging of the electrical double layer (capacitive) or reversible oxidation reduction reactions

(Faradaic). The ideal electrode is purely capacitive to avoid any unwanted irreversible Faradaic reactions. (2) Chemically, electrode materials should support surface functionalization to increase their hydrophilicity, since in vitro measurements across a wide range of material systems show that neurite outgrowth on hydrophilic surfaces is superior to hydrophobic surfaces [81]. (3) Mechanically, flexible electrodes increase the longevity and effectiveness of the neural interconnect. Large rigid neural prosthetic devices induce the brains inflammation response and glia scarring due to rupturing of the neural tissue during implantation as well as movement of the implant after implantation [51]. A few weeks after implantation, the glia scar will encapsulate the device, pushing the target neurons away from the stimulating electrodes. Increasing the implant's flexibility, however, can reduce glia scarring [207] [208]. Because the electrodes must maintain a close proximity to the target neurons over a time period of years, electrode materials should have a mechanical compliance which allows them to be integrated into flexible implants without sacrificing electrical connectivity. Furthermore, neurite outgrowth, elongation rate, and number of branch points are maximized on materials with low elastic modulus [119] [120]. (4) Electrode materials should also feature a favorable nanotopography. For instance, neuron adhesion and outgrowth can be maximized on substrates with appropriate surface roughness [209] [105], groove widths [100] [210], or nanowire dimensions [211]. (5) Finally, especially relevant to subretinal implants (implants positioned behind the retina and directly interfacing with retinal bipolar cells in the inner nuclear layer) are electrode materials that can adopt a high height-to-width aspect ratio. High aspect ratio electrodes could simultaneously reduce glia scar formation at the implant surface [40] [58] and penetrate from the subretinal space into the inner nuclear layer to reduce the electrode

voltage thresholds required to induce membrane potentials in the closely apposed bipolar neurons [36][212].

Arguably, the electrode material which best meets the electrical, mechanical, and biocompatibility requirements for neural prosthetic devices is carbon nanotubes (CNTs). Electrically, CNTs are extremely conductive with a double layer capacitance of $10\,\mathrm{mF/cm^2}$ [70], a capacitance that compares favorably to nearly every other material. CNTs can be functionalized to improve neurite outgrowth and branching [131] [145]. CNT films are mechanically flexible and have been incorporated into flexible films of polyimide, parylene, PDMS, and medical tape [74] [155] [156] . The CNT nanotopography enables tight adhesive contacts between nanotubes and neurons allowing for strong electrical coupling and increased neurogenesis [139] [147]. Cortical neurons also attach to and extend neurites on high aspect ratio CNTs with heights of up to $500\,\mu$m and widths of only $30\,\mu$m [151]. In general, CNTs are biocompatible although heavy metal catalysts used in CNT growth can render the electrode cytotoxic [213].

Previous research has incorporated carbon nanotubes into multielectrode arrays (MEAs) for epiretinal implants (positioned in front of the retina)[74] [154] [214] [215]. For instance, in a recent study, Eletheriou et al. (2017) found the retina was capable of incorporating a CNT MEA into the tissue over 3 days in vitro (3 DIV) providing a close coupling which improved the signal to noise ratio and decreased the stimulation threshold. Additionally, very little glia scarring was seen for implants featuring $30\,\mu$m diameter CNT islands. While these previous CNT developments have taken advantage of the electrical, chemical, flexibility, and nanotopography properties to create an effective MEA for interfacing with retinal tissue, they have yet to explore electrode structures with a high aspect ratio. Vertically aligned carbon

nanotubes (VACNTs) with high aspect ratios and distinct nanotopography can be readily prepared from carbon vapor deposition (CVD) on iron (Fe) catalysts [216], potentially capable of penetrating into the inner nuclear layer and minimizing glia scar formation. Yet, despite their promise for retinal implant electrode materials, the biocompatibility of VACNTs with retinal neurons has not yet been tested.

Methods

Carbon nanotube growth

We fabricated VACNT forests on silicon/silicon oxide substrates using a Fe catalyst alone (Group Fe) and a Fe catalyst on an Al layer (Group Al/Fe). Substrates (University Wafer) were $\sim$1 cm^2 in size with a thermal oxide thickness of 300 nm. Metals were evaporated onto entire substrates using a thermal evaporator to a thickness of 4-8 nm for Al and 6-12 nm for Fe. We used the Al layer to improve the adhesion between the CNTs and the substrate; thin films of Al will oxidize and form aluminum oxide. CNT growth was performed by atmospheric pressure chemical vapor deposition (CVD) in a 2 quartz tube for 5 minutes at 650 °C in a 2:1 mixture of ethylene (C_2H_4) and hydrogen (H_2) at 200 and 100 SCCM, respectively, in presence of 600 SCCM flow of Ar. This growth results in a VACNT forest covering the entire chip. Additionally, we fabricated VACNT pillars with diameters ranging from 2-50 μm. Patterned regions of aluminum and iron used for pillar growth were defined with optical lithography. The metal layer thicknesses and CVD growth conditions for the pillars were identical as those for group Al/Fe forests.

Carbon nanotube characterization

VACNT surfaces were characterized using scanning electron microscopy (SEM), contact angle goniometry, and x-ray photoelectron spectroscopy (XPS). Visual characterization of the CNT structure, topography, and heights was carried out

using a Zeiss Ultra-55 SEM. Wetting contact angles (WCAs) were measured using a Ram-Hart Model 290 goniometer with water drop sizes of 10 μL and the WCAs measured immediately after placing the water drop on the CNT surface. The atomic compositions of VACNT surfaces were obtained by XPS using a Thermo Scientific Escalab 250. XPS provides composition and bonding information from the outermost $\sim$10 nm of a surface. The binding energy scales for the high-resolution spectra were calibrated by setting the main feature of the C 1s peak envelope to 284.8 eV. The balance of the composition was attributable to C. Survey spectra were acquired at a pass energy of 150 eV. High resolution spectra of Fe 2p, C 1s, O 1s, and Al 2p regions acquired at a pass energy of 20 eV were used to determine the composition. Fe 2p spectra were obtained by averaging over 75 scans.

Dissociated retinal cell cultures

All experiments were performed under protocols approved by the University of Oregon's Institutional Animal Care and Use Committee. Retinal cells were obtained from wildtype C57BL/6 mice at postnatal day 4 as previously described [211]. Animals were first euthanized and then whole retinas were dissected from the eyes and placed into DMEM culture medium with high-glucose, sodium pyruvate, and L-glutamine (Thermo Fisher Scientific). After dissection, 4 retinas were transferred into an enzyme solution and digested for 22.5 min at 37 °C to loosen cell-cell adhesion. The enzyme solution was prepared by combining 3 mL DMEM, 3 mg papain (Worthington Biochemical Corporation), and 0.9 μg L-cysteine (Sigma-Aldrich) and filtering through a 0.22 μm filter (Sarstedt). After enzyme digestion, the enzyme solution was removed and the retinas were rinsed thoroughly in DMEM. Digested retinas were then placed into 2 mL of final culture medium. Final culture medium was

prepared by mixing 21.34 mL of DMEM, 440 μL of B27 supplement (Sigma-Aldrich), and 220 μL L-glutamine-penicillin-streptomycin (Sigma-Aldrich). The final culture medium plus digested retinas were then mechanically agitated through a rounded Pasteur pipette to break the whole retinas into single cells or cell clusters. This process also removed most of the neurites and axons from the somas. Next, 48 mL of DMEM was added to the 2 mL dissociated retina solution and centrifuged at 900 g for 5 min. After centrifugation, the supernatant was removed and the remaining 20 mL of final culture medium was added to the cell pellet. The cells were again mechanically agitated to resuspend cells throughout the solution. The cell suspension was then passed through a 40 μm cell strainer filter (Fisher Scientific) to remove large cell clumps. The live cell density as measured by a hemocytometer was (6.9 $\pm$ 1.3) x 10^5 cells/mL. Finally, 500 μL of cell suspension was plated into each 4-well culture plate (Sarstedt, each well 1.9 cm^2) containing a VACNT sample. Neurons were only cultured on VACNT forest samples; they were not cultured on the VACNT pillars. Cell plating was randomized between the sample groups (Fe and Al/Fe). Cells were incubated for 3 days in vitro (DIV) at 37 °C and 5% CO_2.

Immunohistochemistry

Fluorescent labeling of neurons and glia was achieved through dual staining immunohistochemistry. After the culture was stopped, cells were fixed with 4% paraformaldehyde (PFA) for 30 minutes. After fixation, the PFA was rinsed off with 1x phosphate buffered solution pH 7.3 (PBS), and then cells were pre-incubated in PBScomp solution containing 2% donkey normal serum (DNS) and 2% goat normal serum (GNS) (Jackson ImmunoResearch) for 1 h at room temperature. PBScomp was prepared from 1x PBS, 0.25% Triton-X (Sigma-Aldrich), and 1% bovine serum

albumin (Sigma-Aldrich). The pre-incubation solution was then removed and the samples were incubated in the primary antibody solution overnight at 4 C. The primary incubation solution contained PBScomp, 2% DNS, 2% GNS, 1:1500 rabbit anti--tubulin III (neuronal marker antibody) (Sigma-Aldrich), and 1:1500 goat anti-GFAP (glia marker antibody) (Dako). Next, the primary incubation solution was removed and samples were rinsed again in PBS. They were then incubated in a secondary antibody solution containing PBScomp, 1:400 Alexa Fluor 488 donkey anti-rabbit IgG, and 1:200 Cy3 goat anti-mouse IgG (Jackson ImmunoResearch) for 45 min at room temperature. Afterwards, the secondary antibody solution was removed and samples were rinsed again. Finally, the samples were mounted with Vectashield containing DAPI (DAPI attaches to DNA in the cell nucleus) (Vector Labs).

Epifluorescence microscopy

VACNT samples were imaged using a Nikon Eclipse Ti-U epifluorescence optical microscope at 20x magnification (Nikon CFI S Plan Fluor objective, NA 0.45). We imaged a total of 20 randomly chosen positions on each VACNT sample to statistically assess cell response on that sample. The field of view (FOV) of each image was 0.45 mm x 0.45 mm.

Stastical analysis

We examined neurite length, number of glia cells, and total nuclei area as the response variables dependent on VACNT preparations. To quantify the neurite length, we developed an automated image analysis algorithm based off one previously reported by Wu et al. (2010) [217]. The developed algorithm allowed us to calculate the total neurite length in each FOV, but not the neurite length per neuron. Glia cells

were counted manually with the microscope. The total nuclei area was determined by thresholding the DAPI images and calculating the total fluorescent area of single nuclei and clusters (2 or more nuclei in contact with each other). We tested via ANOVA against the null hypotheses that mean neurite length per sample (average length in the 20 randomly chosen fields of view) and mean nuclei area per sample were not dependent on CNT preparation. In total, 8 samples at 3 DIV in each of the 2 groups (Fe and Al/Fe) were tested across 3 independent culture experiments.

Results

We grew densely packed VACNTs with a height of 20-50 μm as inferred from SEM (Fig. 53a-b). The height varied between growths, but there was no significant difference in CNT height between Fe and Al/Fe groups. However, CNTs grown without the Al adhesive layer delaminated easily from the substrate. Addition of the Al adhesive layer stabilized the film and prevented CNTs from flaking off the surface. The CNTs tested were superhydrophobic with wetting contact angles (WCAs) for group Fe of 158.7 $\pm$ 5.1° and group Al/Fe of 158.3 $\pm$ 2.6° (Fig. 54). No major differences in CNT topography could be confirmed by visual inspection with SEM between the 2 groups. As a proof-of-concept for future subretinal implants, we grew high-aspect ratio VACNT pillars ranging from 2-50 μm in diameter and 25-60 μm in height (Fig. 53c-d).

We used XPS to ascertain the elemental composition of the VACNT samples. XPS survey spectra from both groups verified the absence of unexpected elements, and that the Fe, O, and Al content of the outermost 10 nm was either below detection limits or extremely low (Fig. 55a). The Fe content for both groups was 0.1 % atomic. No oxygen was detected on the Fe group samples; 0.3 % oxygen was present at the

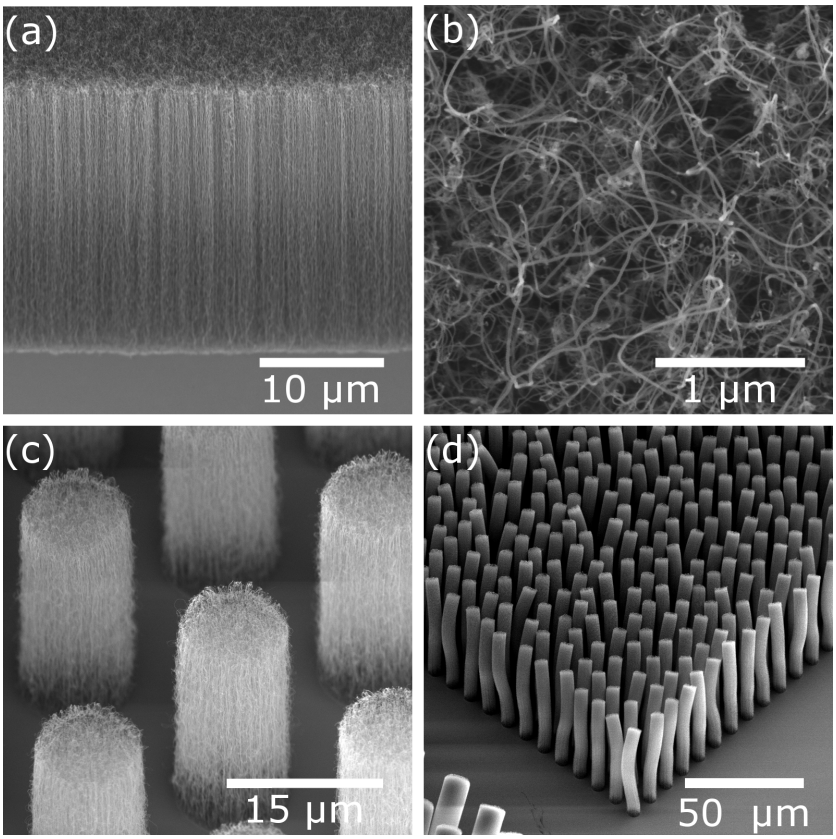

FIGURE 53. VACNT forests and pillars.
VACNT forests grown from Fe catalyst shown (a) from the side and (b) top-down. VACNT pillars (c) 25 μm tall and 10 μm (d) 60 μm tall and 5 μm in diameter prepared from group Al/Fe. The images in (a), (c), and (d) are tilted 40°.

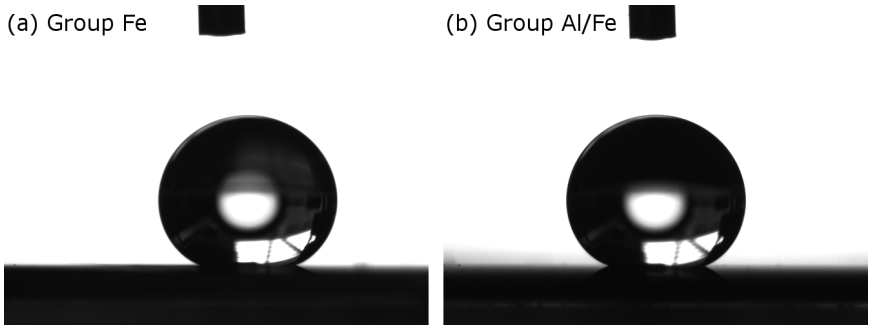

FIGURE 54. Wetting contact angles of VACNT forests.
Wetting contact angle measurements for 10 μL water drops on (a) group Fe and (b) Al/Fe prepared CNT surfaces.

surface of the Al/Fe group VACNTs. No Al was detected in the spectra from either group. Two peaks were used to fit the C 1s peak envelopes: an asymmetric main peak arising from the graphitic sp^2 C=C bonds and a second peak to fit the characteristic π-π^* shakeup feature near 291 eV, consistent with the bond chemistry of high-purity carbon nanotubes (99.6-99.9%.) The high-resolution spectra of the Fe $2p_{3/2}$ region are shown in Fig. 55b. The 10 nm information depth provided by XPS indicates that the Fe detected is either trapped within CNT tips or exposed at the CNT surface. Thus, the CNT growth is, at least in part, due to tip-growth. The low binding energy feature in the Fe $2p_{3/2}$ spectra appears at a binding energy characteristic of metallic Fe (706.7 eV); the feature near 710 eV in the spectrum from the Al/Fe group may indicate the presence of an oxide, although the atomic percentage is too low to be definitively resolved. For reference, the expected binding energy for Fe_2O_3 is 710.8 eV.

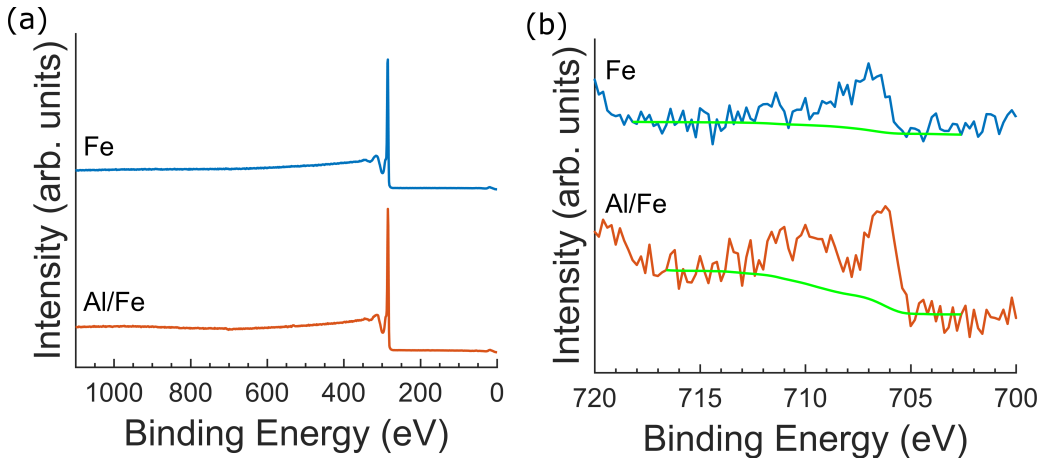

FIGURE 55. XPS VACNT forests.
(a) XPS survey scans for groups Fe (blue) and Al/Fe (red). Both groups clearly feature the C 1s peak at 284.8 eV. (b) XPS Fe $2p_{3/2}$ scans for groups Fe and Al/Fe. Background signal is shown for each scan in green. For reference, the binding energy of metallic Fe is 706.7 eV and Fe_2O_3 is 710.8 eV.

Fe and Al/Fe groups were found to support neuron and glia process outgrowth up to 3 DIV (Fig. 56a-b). The cell density between the two groups was approximately equivalent. No statistical difference in DAPI positive area existed between group Fe and group Al/Fe. For each group, neurites of several hundred microns were observed. In order to quantify neurite outgrowth, we compared mean neurite length between samples. Neurites were successfully extracted using our automated image analysis (Fig. 3c). We found an error of <5% in the neurite length extracted by the automated algorithm compared to neurite lengths extracted using the semi-automated ImageJ plugin Simple Neurite Tracer on 5 different images. ANOVA testing revealed that Al/Fe group gave a significantly larger mean neurite length as compared to group Fe ($p < 0.0005$) (Fig. 57). An evaluation of the number of glial cells at 3 DIV showed no difference between the Fe and Al/Fe groups. The morphological shape of the glial cells was also similar in both groups. Therefore, both VACNT preparations support similar glia growth up to at least 3 DIV.

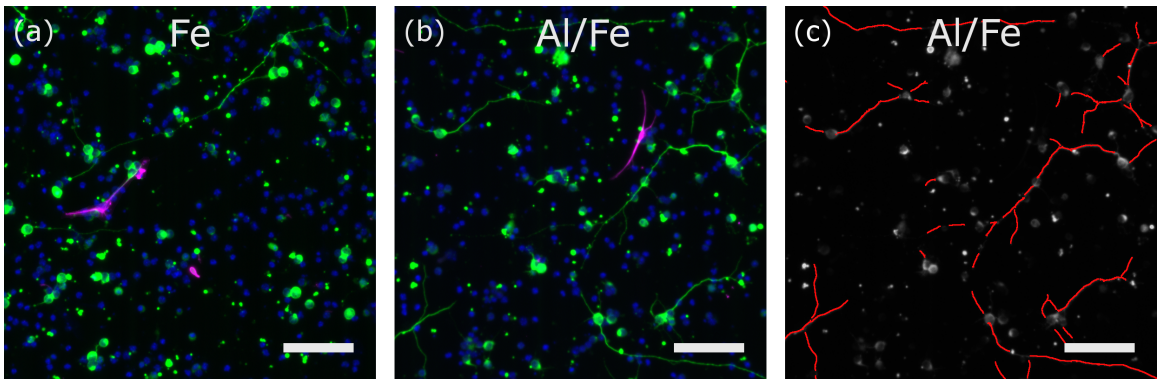

FIGURE 56. Neurons and glia on VACNT forests.
Fluorescently labelled neurons (false colored green), glia (false colored magenta), and cell nuclei (blue) on CNT groups (a) Fe and (b) Al/Fe. (c) Automatically extracted neurites (red) on the Al/Fe image shown in (b). Scale bar is 100 μm in each image.

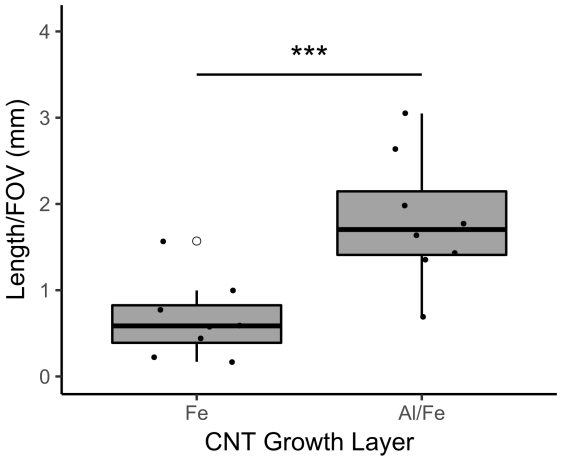

FIGURE 57. Neurite lengths on two different VACNT preparations. ANOVA testing revealed the average neurite length per field of view (FOV, 0.45 mm x 0.45 mm) after 3 DIV is greatest for neurons grown on group Al/Fe ($p < 0.0005$). Each black dot represents the mean length for all 20 FOVs on each of the 8 samples.

Discussion

We cultured dissociated retinal cells on two different VACNT preparations to investigate the biocompatibility of such electrode interfaces for future applications in vivo. Neurons survived in culture and extended neurites despite the presence of a small atomic percentage of Fe (0.1%) and possible Fe_2O_3 at the CNT top surface as measured by XPS. Previous research has shown Fe2O3 nanoparticles reduce neural cell viability after 3 days post-exposure by 25% for Fe2O3 nanoparticle concentrations of 1.5 mM and by 90% for concentrations of 15 mM [218]. Because of the observed neurite outgrowth, it is therefore likely that the Fe or Fe_2O_3 nanoparticles required for the catalysis of CNTs are trapped within the multiwall CNT tips and do not come into contact with the cells.

One requirement for in vivo applications is the electrodes must be physically stable. In the case of CNTs grown without the Al adhesive layer (Group Fe), CNTs easily flaked off the substrate during preparation and handling of the samples, thus

indicating that group Fe does not possess the mechanical stability necessary for in vivo applications. Addition of the Al adhesive layer (group Al/Fe) stabilized the CNT film and yielded favorable neurite outgrowth for up to 3 DIV.

Neurite outgrowth on group Al/Fe was significantly larger than group Fe, even though the two groups had similar nanotube heights, nanotopographies, hydrophobicities, and atomic compositions. In fact, the only major difference we detected was that group Fe delaminated easily from substrate, while group Al/Fe did not. The reduction in neurite outgrowth in group Fe may be due to exposure to CNTs dispersed in the cell culture medium. In a previous study investigating the effect of dispersed multi-walled CNTs on axonal regeneration of mouse dorsal root ganglia [219], incubation with MWCNTs (10 - 20 μm in length prepared from Fe catalyst) at concentrations increasing from 1 μg/mL to 10 μg/mL caused a reduction in regenerated axon length by 40% to 70%, respectively, as compared to control. However, these concentrations did not cause cell death. We hypothesize that CNTs on group Fe samples detach either before and/or during the culture, leading to a similar reduction in neurite length without cell death. In particular, our calculation shows that for CNTs of height 30 μm on a 1 cm^2 chip in 500 μL of cell suspension, as prepared here, along with a graphitic density of 2.1 g/cm^3, CNT dislodgement at the level of 0.1% by weight (i.e. 10 μg/mL) could cause the 70% reduction in mean neurite length seen in group Fe. Additionally, although we did not directly measure cell death in our present study, the nuclei density after 3 DIV between groups Fe and Al/Fe was similar. Therefore, the reduction in neurite length is not due to a lower cell density, but rather the data indicates the neurite outgrowth in group Al/Fe occurs because of a favorable growth environment.

Surface functionalization of the VACNTs was not required to support retinal neurite outgrowth, despite the hydrophobicity of the VACNTs. Neural adhesion and outgrowth are expected to be reduced on hydrophobic surfaces. In part, this occurs because large blocking proteins, such as albumin, absorb more strongly to hydrophobic surfaces and displace hydrophilic extracellular matrix glycoproteins, such as fibronectin or laminin, which neurons bind to through transmembrane integrin receptors and use to extend neurites [81]. Therefore, our VACNT preparation presents an easy fabrication scheme for electrode implants. However, we expect tailoring the surface functionalization of the VACNTs could provide additional adhesive and electrical benefits. For instance, hippocampal neurite outgrowth on plasma functionalized short ($\sim$2 μm) sparse VACNTs prepared from a Ni catalyst was greater than compared to unfunctionalized, adsorptive, and covalently modified surfaces [145]. Similarly, carboxylic and hydroxide group modification of CNTs leads to dorsal root ganglia extending long neurites which strongly interconnect with the underlying CNT surface [135]. Electrically, plasma functionalizing 2500 μm^2 VACNT electrodes increased the capacitance from 0.54 mF/cm^2 on unfunctionalized VACNTs to 2.25 mF/cm^2 on plasma functionalized CNTs [158].

We also fabricated VACNT pillars with an aspect ratio up to 12 as a proof-of-principle for high-density subretinal electrodes designed to penetrate from the subretinal space to the inner nuclear layer. These high-aspect ratio VACNT electrodes could (1) potentially reduce glia scar formation, as has been observed in other high-aspect ratio devices [40] [58] devices, and (2) reduce the electrode thresholds for inducing membrane potentials in bipolar neurons [212] [36]. Due to the relatively low temperature, 650 °C, used here to prepare the VACNTs, we expect the fabrication

procedure outlined would be compatible with semiconductor processing used to fabricate current generation subretinal implants [32] [37].

Conclusions

Mechanically stable, unfunctionalized, high aspect ratio vertically aligned carbon nanotubes prepared from an Fe catalyst with Al adhesive layer support retinal neurite growth up to at least 3 days in vitro. High-aspect ratio electrodes have enormous potential in future subretinal implants to improve visual acuity by reducing glia scar formation and decreasing the separation between electrodes and bipolar neurons. Taken together, these results suggest high-aspect ratio VACNTs are a promising material for future developments in retinal implant electrodes.

Retinal Cell Cultures on Functionalized Vertically Aligned Carbon Nanotubes

In order to further improve the retinal neuron-VACNT interface, we explored a set of experiments aimed at chemically functionalizing the VACNTs. The previously investigated groups, Group Fe and Group Al/Fe, were plasma functionalized to create two additional groups, Group Fe+Pl and Group Al/Fe+Pl. All methods and sample characterization, with the exception of the plasma treatment, were as previously described in the Methods section 3.1. Plasma functionalization was carried out in a South Bay Technology PC-2000 Plasma Cleaner at 300 mTorr O_2 (60 mTorr base pressure) for 5 min at 50 W forward power.

Plasma treated VACNTs, groups Fe+Pl and Al/Fe+Pl, were characterized by SEM, contact angle goniometry, and XPS. No major differences in VACNT height or topography could be confirmed by visual inspection with SEM between any of

the 4 groups (Fe, Al/Fe, Fe+Pl, or Al/Fe+Pl). VACNTs from Group Fe+Pl easily delaminated from the substrate during sample preparation and handling, similar to Group Fe. The WCA of the plasma functionalized groups Fe+Pl and Al/Fe+Pl could not be directly measured but was approximately 0°. XPS survey spectra for the plasma functionalized groups featured several new characteristics that were absent for the unfunctionalized VACNTs. First, in addition to the C 1s peak, there was an O 1s peak occurring near 533 eV (Fig. 58), which is standard for plasma functionalized VACNTs [220] [221]. Deconvolution of the C 1s and O 1s peaks revealed graphitic sp^2 C=C bonds and the π-π^* shakeup feature for each group as well as sp^3 C-C bonds, C-O alcohols and ether functionalities, and O-C=O carboxylic and ester functionalities for Fe+Pl and Al/Fe+Pl groups (Fig. 59). The atomic percentage of Fe was similar between all groups, 0.1% for groups Fe, Al/Fe, and Fe+Pl and 0.2% for group Al/Fe+Pl. Additionally, as with the unfunctionalized groups, no unexpected elements and no Al were detected by XPS for groups Fe+Pl or Al/Fe+Pl.

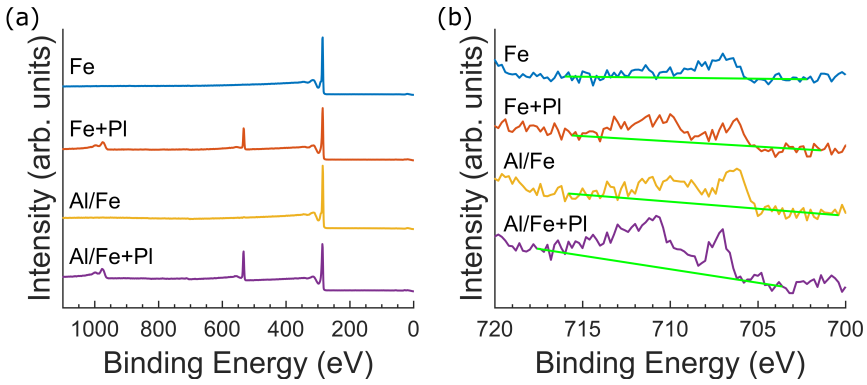

FIGURE 58. XPS plasma functionalized VACNT forests.
(a) XPS survey scans for groups Fe (blue), Fe+Pl (red), Al/Fe (yellow), and Al/Fe+Pl (purple). Each group clearly features the C 1s peak at 284.8 eV. Additionally, the oxygen plasma functionalized groups, Fe+Pl and Al/Fe+Pl, show O 1s peaks occurring near 533 eV. (b) XPS Fe $2p_{3/2}$ scans for groups Fe, Fe+Pl, Al/Fe, and Al/Fe+Pl. Background signal is shown for each scan in green. For reference, the binding energy of metallic Fe is 706.7 eV and Fe_2O_3 is 710.8 eV.

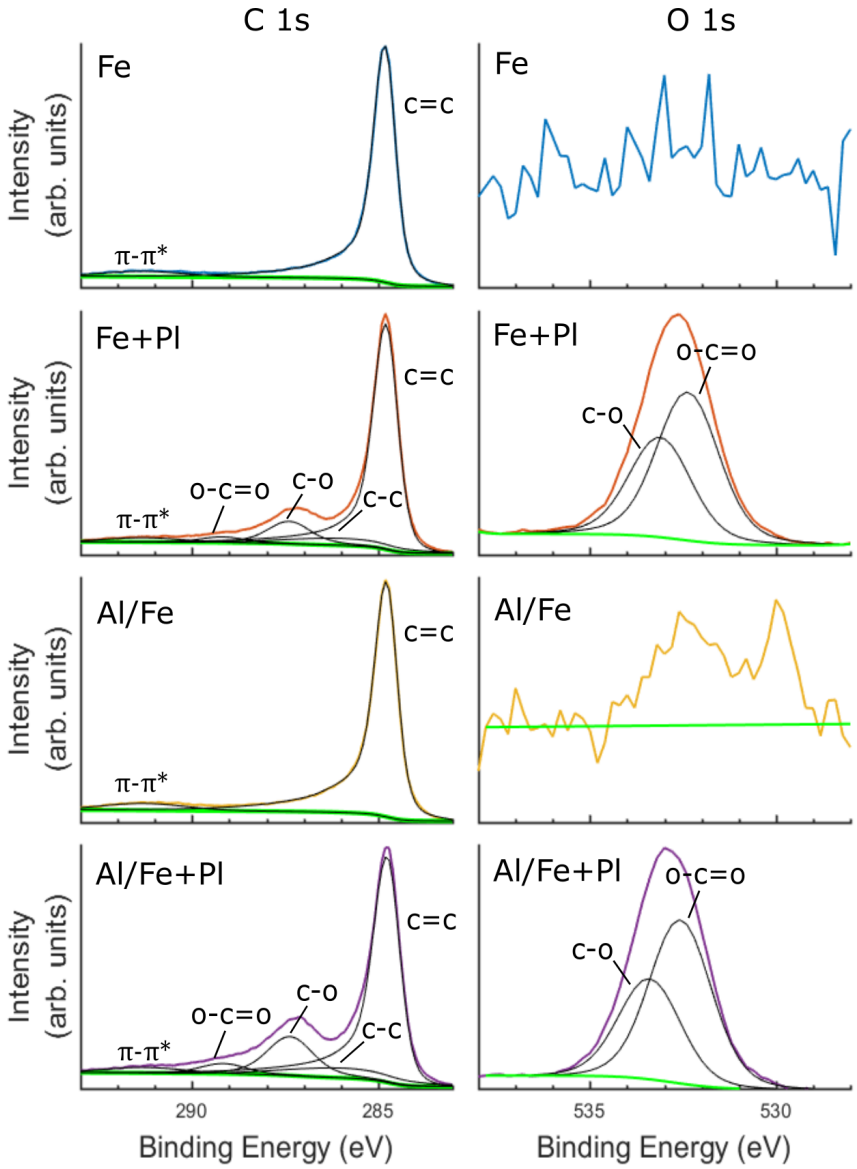

FIGURE 59. XPS peak deconvolution of VACNT forests.
XPS spectra at the C 1s peaks (left columns) and O 1s peaks (right columns). Each spectrum is associated with the CNT surface indicated by the group name in the top left. Background signal is shown in green. C 1s peak deconvolution showed graphitic sp^2 C=C and π-π^* bonds for all surfaces. The functionalized groups, Fe+Pl and Al/Fe+Pl, also featured sp^3 C-C bonds, C-O functionalities, and O-C=O functionalities. No oxygen was detected for group Fe and only a minimal amount (0.3%) for group Al/Fe. The atomic percentage of oxygen was 12.9%for group Fe+Pl and 16.5% for group Al/Fe+Pl. The feature in the Al/Fe O 1s spectrum near 530 eV is consistent with oxygen in an iron oxide while the 532.5 eV feature is consistent with oxygen bound to carbon.

Neurite length, number of glia, and DAPI area were also investigated for the plasma functionalized groups (Fig. 60). Similar to groups Fe and Al/Fe, group Fe+Pl featured neurites of several hundred microns and the DAPI area between the three groups was not statistically different. The glia number of and morphology was similar for group Fe+Pl and the groups Fe and Al/Fe. For the Fe+Pl group, during the deposition of the cell suspension onto the surface, large scale cracks formed throughout the entire CNT film (Fig. 2c). Interestingly, Al/Fe+Pl group did not support neurite or glia outgrowth. Additionally, we also found a strong reduction in DAPI intensity at the nuclei between unfunctionalized CNT groups (Fe and Al/Fe) and the plasma functionalized groups (Fe+Pl and Al/Fe+Pl) with increasing days post-fixation. In particular, 2 days after secondary immuno, nuclei in all 4 groups could be resolved with equivalent fluorescent intensities and image gain. However, by 12 days after secondary immuno, Fe+Pl and Al/Fe+Pl groups required a 5 fold increase in gain relative to unfunctionalized groups in order to resolve the nuclei. ANOVA testing

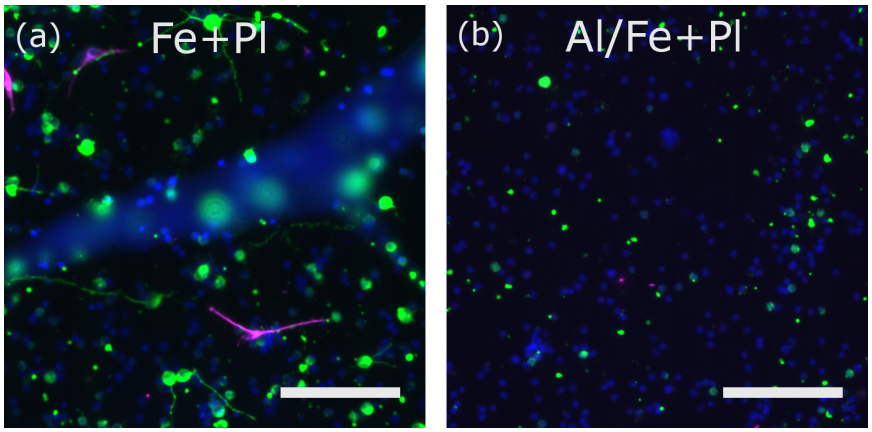

FIGURE 60. Neurons and glia on functionalized VACNT forests. Fluorescently labelled neurons (false colored green), glia (false colored magenta), and cell nuclei (blue) on CNT groups (a) Fe+Pl and (b) Al/Fe+Pl. Cracks in the CNT film for Fe+Pl group (c) cause part of the image to be out of focus. Scale bar is 100 μm in each image.

with Tukey's HSD revealed that Al/Fe group significantly gives the largest mean neurite length as compared to the other 3 groups ($p < 0.0005$) (Fig. 61). There was not a statistical difference in outgrowth between groups Fe+Pl and Al/Fe+Pl.

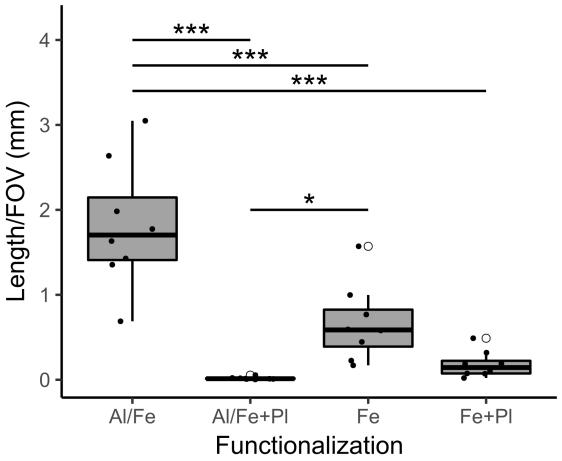

FIGURE 61. Neurite length box plot between four different VACNT preparations. ANOVA testing revealed the average neurite length per field of view (FOV, 0.45 mm x 0.45 mm) after 3 DIV is greatest for neurons grown on group Al/Fe ($p < 0.0005$). Additionally, neurite length/FOV was greater than on group Al/Fe+Pl ($p < 0.05$). Each black dot represents the mean length for all 20 FOVs on each of the 8 samples.

We performed retinal cell cultures on plasma functionalized VACNTs to investigate the hypothesis that neurite outgrowth on the functionalized surfaces could be further increased relative to the outgrowth observed on group Al/Fe. A surprising result from our research is that hydrophilic modification of VACNTs by plasma functionalization reduced neurite outgrowth. As discussed in section 3.1, neurite outgrowth on hydrophilic surfaces is superior to hydrophobic surfaces [81]. A hypothesis for the lack of neurite outgrowth seen in Fe+Pl and Al/Fe+Pl groups in the present study is toxic Fe_2O_3 nanoparticles [218] trapped in the CNT tips, as indicated by the XPS analysis, are freed during plasma etching. Previous research has found that oxygen plasma functionalization of CNTs grown from Fe catalyst

with an Al adhesive layer does indeed open the tips [220]. Thus, we hypothesize the plasma functionalization procedure used was incompatible with VACNT surfaces for cell culture studies. In particular, we later realized that plasma functionalization of VACNT surfaces is typically carried out for much short time periods, i.e. tens of seconds versus minutes [145] [146]. In order create biocompatible VACNT interfaces prepared from Fe catalysts for neural implants, we suggest either (1) decreasing the Fe catalyst layer thickness so that no Fe exists in the CNT tips and/or (2) reducing the time of plasma functionalization.

Retinal Cultures on Carbon Nanotube Rows and Fractals

Both nano and micron sized topographies lead to VACNTs being an ideal electrode material for neural implants. At the nanoscale, the mesh-like amalgamation of CNTs leads to an increased double-layer capacitance [70] and a local geometry which neurons can bind and attach to, thus creating a strong interface [147]. At the micron scale, patterning of VACNTs can direct neurite outgrowth [143], a very desirable property for implants designed to regrow peripheral nervous system neurons after traumatic injury. Additionally, previous research using non-conductive materials has shown glia scars can be 'herded' into the inter-site spaces [40] [58]. VACNTs may therefore be capable herding glia between the active electrode sites, leading to a stronger stimulation and recording quality and increased device longevity.

This section outlines preliminary work on micron-sized geometrical patterning of VACNTs. Both fractal and Euclidean row geometries are investigated. We find preliminary evidence that: (1) neurons preferentially adhere to and extend neurites on VACNTs over the SiO_2 substrate, (2) neurites prefer to extend along the edges

of the VACNT patterns, and (3) glia can be herded into the non-conductive regions between the VACNTs.

We grew VACNTs with a geometries of either H-tree fractals or Euclidean rows. H-tree VACNT electrodes spanned an 8 mm x 8 mm region with line widths down to 50 μm and an electrode height of 15 μm (Fig. 62). Euclidean rows had line widths This relatively large size was chosen due to an easy optical lithography fabrication of the CNT catalyst layer. The VACNT growth is described in Section 3.1, with the exception that the growth time was reduced from 5 min to 3 min.

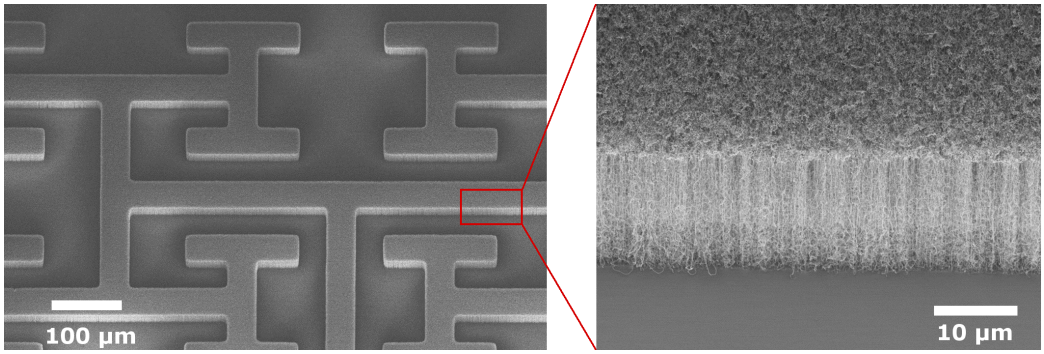

FIGURE 62. Fractal VACNT electrode.
(Left) Fractal VACNT H-tree electrode. (Right) Zoom-in shows the well aligned carbon nanotubes and the textured top and sidewall areas.

Retinal cell cultures on the row geometries illustrate the three major preliminary findings of this section (Fig. 63). The fluorescent images shown in Figure 63 were taken after 17 DIV. (1) Neurons preferentially adhere to and extend neurites on the VACNTs. In fact, there is nearly zero fluorescence from the fluorescently tagged neurons seen on the SiO_2 surface. Whereas the top surface exhibits extensive neurite branching. (2) Neurites prefer to extend along the edges of the VACNT rows. Nearly every row has a long neurite branch extending along the edge for distances over a few hundred microns. (3) Glia are 'herded' between the VACNT rows. Extensive glia

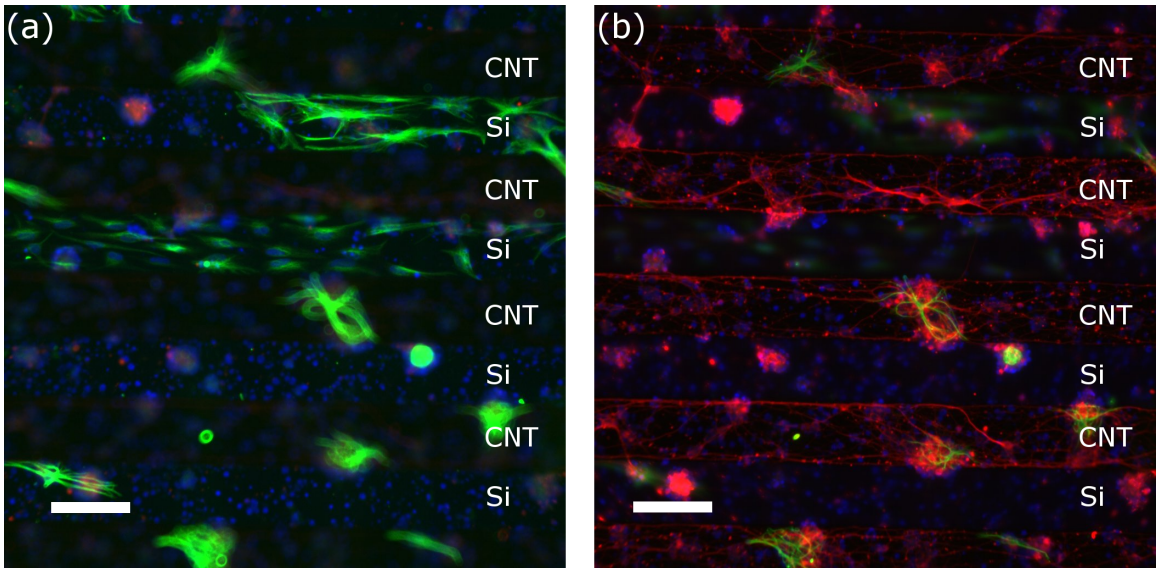

FIGURE 63. Neurons and glia on VACNT row geometries. Fluorescent images taken at 20x magnification after 17 DIV of neurons (red), glia (green), and cell nuclei (blue) with the microscope focused (a) on the substrate surface and (b) on the top of the VACNTs. (The top of the VACNTs and the substrate surface cannot both be in focus at 20x magnification due to the vertical height separation between the top and bottom.) Scale bars are 100 μm.

proliferation (i.e. cell division) is seen on the SiO_2 surface between the VACNT rows. This proliferation does not grow upwards onto the VACNT top surface, but rather extends along the row's gap. Glia which are present on the VACNT top surface, do not proliferate.

These preliminary findings on the row geometries motivate the development of fractal VACNT electrodes for three reasons. (1) Extensive neurite adhesion and outgrowth up to 17 DIV on the VACNTs indicates it is a biocompatible material for long term use retinal implants. (2) Fractal geometries inherently maximize perimeter to area ratios. The fractal electrode will thus feature a large number of internal edges which neurites can extend along, leading to an improved neuron-electrode coupling. (3) Maintaining a biocompatible interface requires a careful balance in the number of

glia at the interface. Glia are needed to support neuron health and neurotransmission. However, too many glia creates a glia scar which pushes the neurons away from the interface. The fractal electrode features the perfect compromise between these two factors. Due to the multi-scaled gaps in the fractal electrode, the glia can be herded into the internal electrode area without sacrificing the neuron-electrode coupling.

Neurons also preferentially attached to and grew along the VACNT fractal electrodes after 3 DIV (Fig. 64). This close attachment to the electrode should ensure high stimulation rates for neural implants. Interestingly, SEM analysis of the neurons on the H-tree after 3 DIV showed some neurites forming 'bridges' between the silicon bottom surface and the VACNT top surface (Fig. 65). Because growing neurites use traction forces to extend, it is likely impossible the neurite grew along the final path depicted in Figure 65. Rather, one hypothesis is that the neurite may have extended down the H-tree sidewall then along the SiO_2 substrate, and finally 'ratcheted' itself tight to the final position shown.

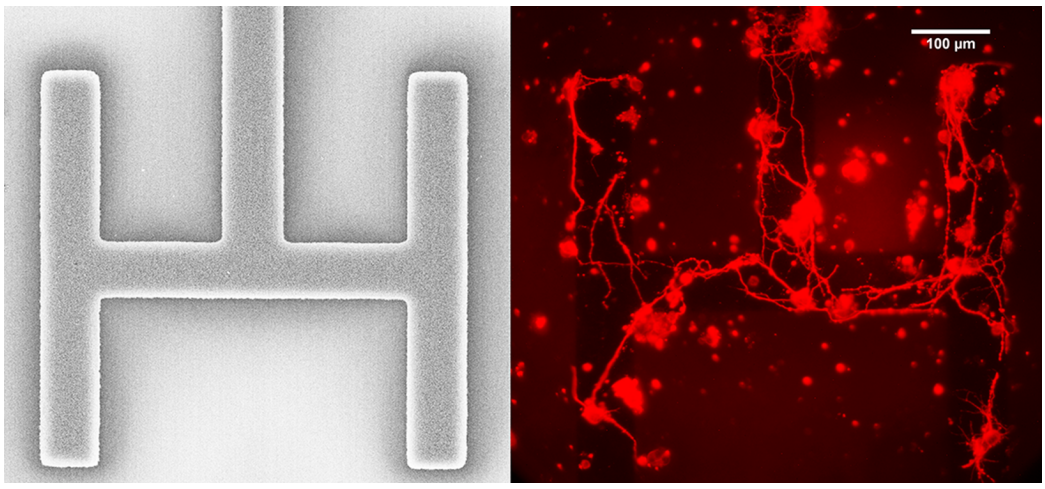

FIGURE 64. Neurons on fractal VACNT electrode.
(Left) Lowest iteration of the H-tree. (Right) Retinal neurons (red) preferentially attach to and grow neurites along the H-tree VACNT over the SiO_2 substrate.

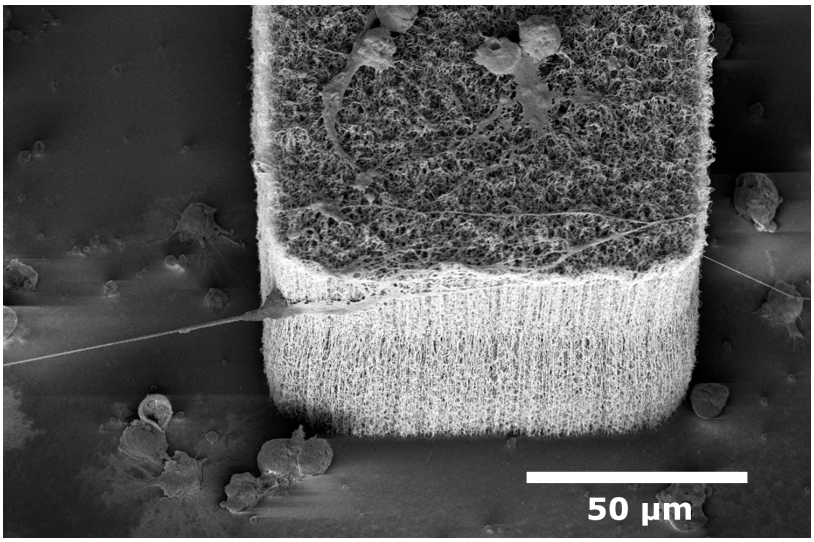

FIGURE 65. Neurites can extend from VACNT top surface to silicon oxide substrate. Two neurite 'bridges' can be seen on each side of the H-tree. The neuron soma which forms the neurite bridge on the left is attached to the H-tree sidewall.

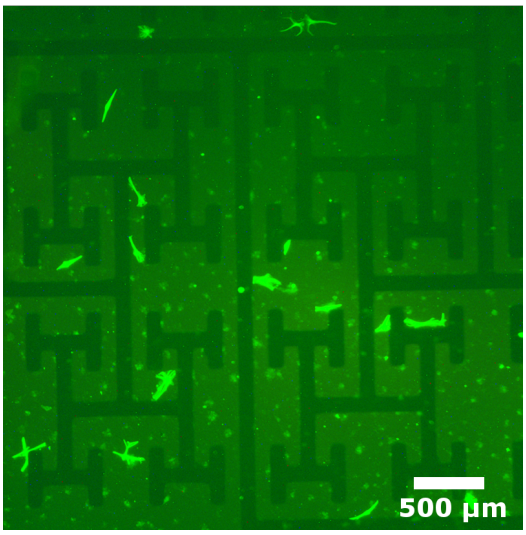

FIGURE 66. Glia on VACNT fractal H-tree
Glia (green) extend on SiO_2 between an H-tree VACNT after 3 DIV.

Preliminary evidence suggests glia can also be herded onto the SiO_2 substrate between the VACNT areas on the fractal electrode (Fig. 66). However, the culture length in this experiment was only 3 DIV, which is too short of a time to see the

large scale glia division which is associated with glia scarring on in vivo implants. Future experiments are planned to investigate the glia herding on fractal electrodes over longer days in vitro.

These preliminary investigations on micron-sized geometries have shown: (1) retinal neurons preferentially attach to and extend neurites along the VACNTs, (2) the neurites also prefer to extend along the edges of the VACNT patterns, and (3) glia can be successfully herded between the VACNTs. These three findings can be implemented into neural implants to create a close neuron-electrode coupling which herds glia into the inter-electrode space without creating a glia scar. Such a device has tremendous potential for long term implant stability.

CHAPTER IV

BIOPHILIC FRACTAL SENSORS FOR THE SIMULTANEOUS MEASUREMENT OF MULTIPLE NEURONAL SIGNALS

A high priority in systems neuroscience is the ability to record from large numbers of neurons simultaneously in the intact brain. We propose a potentially significant advancement in extracellular recording probes in which each sensing pad on the probe is capable of uniquely isolating multiple neuronal signals from the background. Currently, detecting many individual neural signals among a large population involves recording the field potential with devices such as multielectrode arrays (MEAs) and multitransistor arrays (MTAs) and then isolating individual signals using various sorting algorithms. However, these algorithms are limited by identifying waveform signatures of each neuron which are not necessarily unique among different neurons or constant in time. Thus, a subjective component in waveform sorting must be used to apply these algorithms. This prevents a large number of signals from being recorded. To overcome this barrier, we aim to demonstrate a novel transistor technology which locates and measures multiple somatic spikes per site without any a priori identification of spike signatures. Additionally, we briefly propose a sensor technology which utilizes semiconducting carbon nanotube as the active area for the transistor.

Multi-Terminal In Vivo Transistor Sensors

Understanding neural processing from a bottom-up approach involves simultaneous recording of large neural populations. An ideal device would precisely locate and record membrane potentials of thousands of individual neurons. However, the

complex distribution of neurons along with multiple action potentials occurring simultaneously makes isolating and recording the signal from any one neuron an extremely difficult task. This problem is analogous to the 'cocktail party problem' where the listener tries to locate and listen in on a specific conversation among all the background chatter.

In the case of neural networks, the background 'chatter' can be overwhelming. All active neurons in a given volume contribute to the extracellular electric potential. Isolation of a neuron's action potential, or spike, requires measuring the extracellular potential and then decoding the spike from the background signals. Presently, large scale in vivo electrical recordings of the extracellular potential measure cellular signals with a sub-cellular resolution of $\sim 30\,\mu$m at a temporal rate of $\sim$ 2 kHz. Sorting algorithms then attempt to identify which neuron the spike originated from.

Today's sensors are based on 2 distinct technologies the multielectrode array (MEA) and the multitransistor array (MTA). MEAs have low noise and allow for recordings of the field potential as low as $40\,\mu$V at a resolution of $28\,\mu$m [153]. Although lithography would allow for a higher resolution of recordings, the surface area of an electrode cannot be decreased too much as the impedance increases, thus reducing the signal-to-noise ratio [222]. On the other hand, MTAs offer a high spatial resolution of $7.8\,\mu$m but suffer from a larger noise in recording of $\sim 250\,\mu$V [223]. A variation on MTAs use vertical nanowires to provide both a high spatial resolution and high signal-to-noise ratio but presents difficulties for implantation for in vivo experiments [224].

Post-processing of field potential recordings to sort individual neuronal signals typically falls within one of two categories waveform analysis or triangulation. Waveform analysis performs a clustering analysis on spike features of processed data

to identify the unique signature of an individual neuron. For in vivo experiments, waveform analysis is limited by (1) isolating thousands of signals many of which have too small an amplitude to be sorted, (2) waveform variability among a single neuron, and (3) electrode drift with time [225]. The second method triangulates each signal by measuring the waveform variation among different electrodes. This method assumes recorded signals originate from a point source, i.e. the soma. Dendritic signals and errors in uniquely identifying the locations of thousands of somatic locations presents problems for triangulation algorithms [226].

The need to develop a non-subjective measure of neuronal spike isolation with definite errors has been expressed by Buzski in 2004 and again by Einevoll et al. in 2012. Despite the progress in algorithms to uniquely identify neuronal spikes, researchers in different laboratories cannot objectively compare data. To overcome these critical barriers, the next generation of in vivo probes need to: (1) uniquely identify signals from individual neurons despite variations of their waveform, (2) record from hundreds of neurons simultaneously (3) record with sub-cellular resolution at greater than 1 kHz, (4) be robust against electrode drift, and (5) be biocompatible.

We aim to fabricate and test a novel in vivo penetrating MTA which encompasses all of these crucial requirements. Each recording site uses an interconnecting carbon nanotube (CNT) transistor along with multiple current readings to identify up to 5 simultaneous action potentials. Each probe shaft is capable of identifying 80 signals from an 800 μm x 50 μm x30 μm volume of neural tissue in vivo . Recordings from this sensor will greatly enhance the understanding of deficits in neural network function that underlie disorders such as Alzheimers and depression, and could eventually lead to neural prosthetic devices for treating retinal diseases or spinal cord injury.

Algorithm Development to Uniquely Isolate Neuronal Spiking

In field effect transistor (FET) arrays, the field potential created by the neuronal population acts as the equivalent of a gate voltage on the transistor through which current changes are recorded (Fig. 67a) [227]. This gate voltage causes an electrostatic depletion region in the semiconductor in which the charge carriers experience a resistance due to the electric field with the size of the depletion region being determined by the strength of the signal (Fig. 67b). The location of the depletion region will affect the current throughout the entire circuit, which can then be exploited to spatially locate the firing neuron.

We aim to demonstrate that our probe can identify the location and magnitude of up to 5 independent action potentials in the vicinity of each transistor. To isolate one signal and determine the neuron from which it originated could be performed using triangulation. In this case, three independent measurements allow us to determine three variables: position (x and y coordinates) and amplitude of the signal at the soma. Our algorithm merges the ideas behind triangulation and previously existing FET devices. An FET with 16 terminals (Fig. 67c) provides 15 independent current measurements. Current conservation implies the last terminal is a dependent variable. The FET would detect the field potential from nearby neurons and we hypothesize that complex current paths through each terminal will allow localization of 5 spikes per transistor. A second modification uses interconnecting CNTs to increase sensitivity to weak signals (Fig. 67d). The entire probe will use 16 transistors to identify up to 80 signals from an 800 μm x 50 μm x30 μm volume of neural tissue in vivo (Fig. 67e).

Simulations of the current readings from our sensor were performed using modified nodal analysis. Modified nodal analysis is an ideal method for calculation

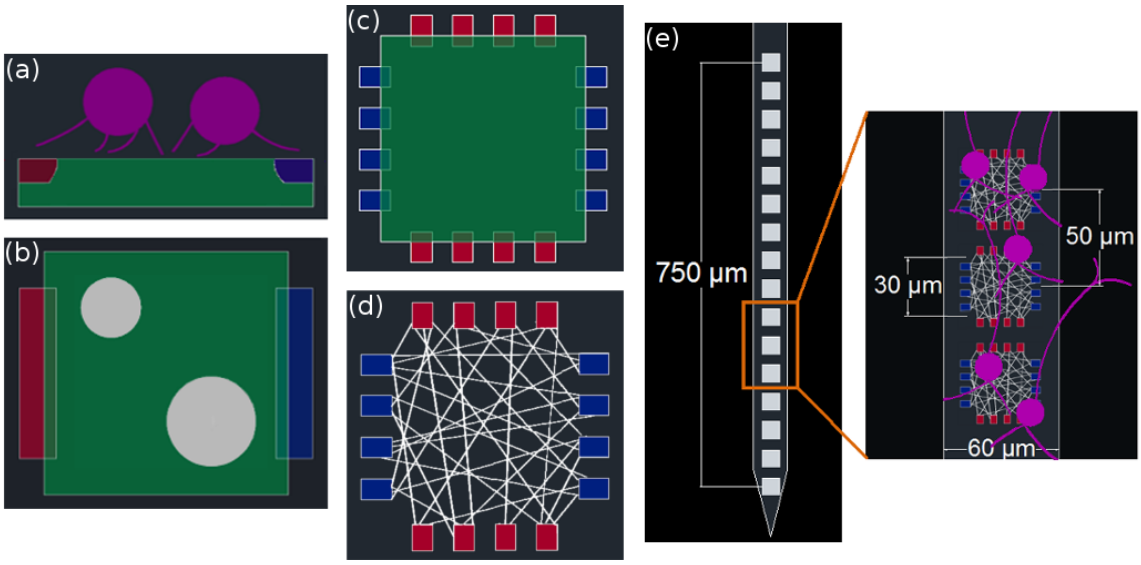

FIGURE 67. Novel transistor probes for in vivo neural recordings. (a) Neurons (purple) acting as equivalent gate voltages on an FET (green) with a source (red) and drain (blue) (b) Idealized depletions (gray) in an FET for two simultaneous action potentials. (c) Modified FET device which uses multiple source and drains. (d) Multi-terminal FET device which replaces standard silicon semiconductor with interconnecting CNTs (white). (e) Our proposed penetrating in vivo MTA sensor (white squares). For each recording site along the probe in (e), 5 spikes can be sorted by adapting the multiple terminal architecture of (d).

of currents through complex resistive networks (see Section 2.1). The simulations assume the potential is due solely to point charges, i.e. somatic field potentials. The magnitudes and positions of up to 2 depletion regions were independently varied and the current values recorded. These current versus depletion region graphs provide a calibration system of 15 equations which can be used to determine the position of a somatic spike, x, y, z, and it's magnitude, m, by recording 15 independent currents.

Five scenarios in Figure 68 illustrate how a multiple terminal FET distinguishes spiking patterns. Six randomly chosen currents have been measured. A single spike in direct contact with the surface (Fig. 68a) creates a smaller depletion region than two spikes in direct contact (Fig. 68b). However, if one spike occurs 15 μm above

the surface (Fig. 68c) the depletion pattern is still identifiable even though the signal is weaker. Action potentials between two recording sites can even be recorded (Fig. 2d) as the potential still causes a depletion at the transistor. Finally, weak signals near the surface (small light purple signal Fig. 68e) can be distinguished from strong signals above the surface (Fig. 68c) due to how the potential spreads out across the

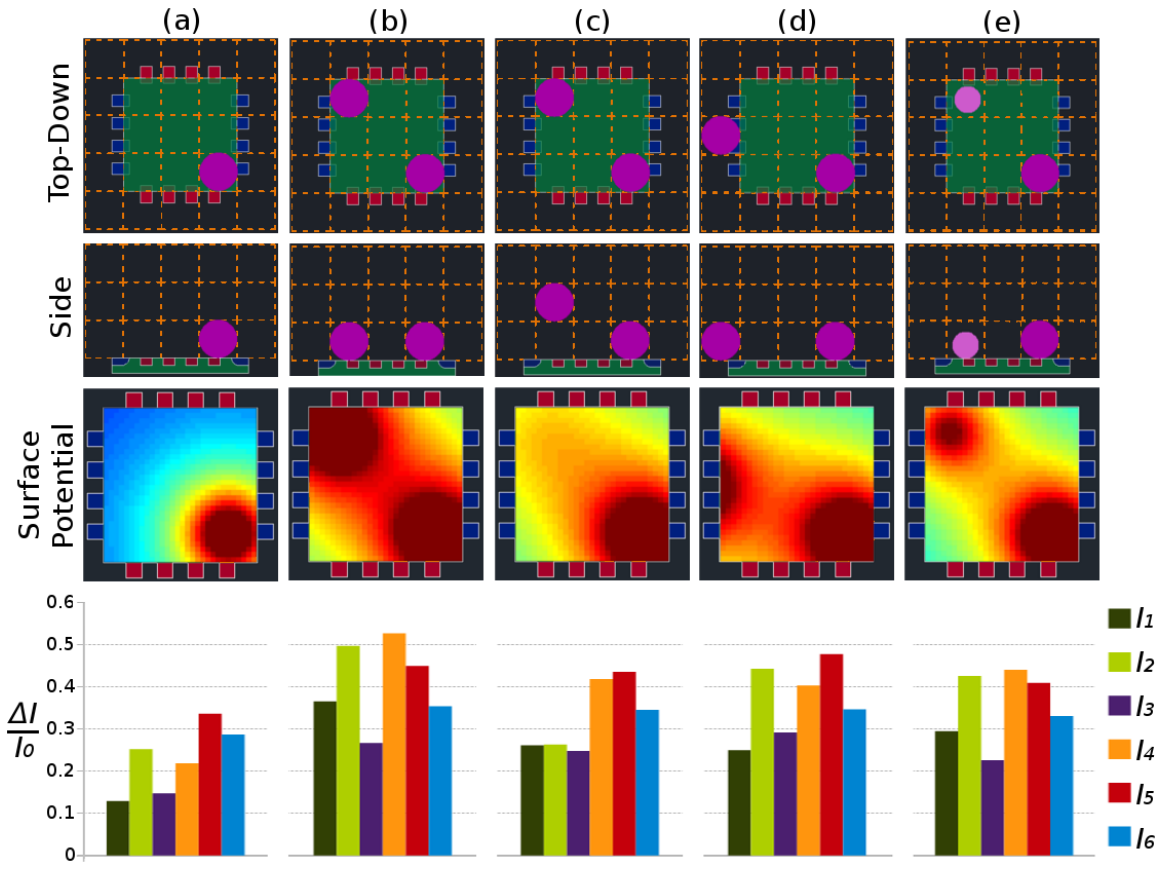

FIGURE 68. Multi-terminal transistor example neuron localization. Illustrative examples show how spiking events with different spatial positionsx, y, z, and magnitudes, m, lead to unique sets of current measurements. The top-down and side projections show spikes within a 10 μm resolution orange grid. The (x, y, z) coordinates of spike locations as well as spike strengths lead to unique surface potentials. In turn, this causes a unique rerouting of currents through the transistor. $\Delta I/I_0 = (I - I_0)/I_0$ is the normalized current change through a terminal with I_0 the terminal's current for a non-depleted transistor.

transistor. The set of six current recordings (last row Fig. 68) is unique throughout all cases allowing us to bin a set of signals into their respective locations set by the resolution of the sensor. Because we record what set of signals come from which boxes, irrespective of initial waveform, our recording method would be robust against electrode drift and signal variation.

The measured set of current recordings forms a *calibration library* which can be used to determine the neuron's position and magnitude (x, y, z, m). (Fig. 69). For each set of (x, y, z, m), there is a corresponding point in the sensor current space. Figure 69 shows the calibration library for 3 of the 15 currents, I_1, I_2, and I_3.

Degeneracies occur if two points in the current space overlap within the noise limits of the signal recording. For instance, for 2 separate events *1* and *2* with a set of currents $\vec{I}_1$ and $\vec{I}_2$, and with a current noise, I_n, then if $\vec{I}_{1,j} \leq \vec{I}_{2,j} \pm I_n$ for every recording j=1 to 15, then the signal is degenerate.

The absolute maximum number of signals which can be uniquely identified occurs when no two points overlap within the noise limits. If we consider a typical noise

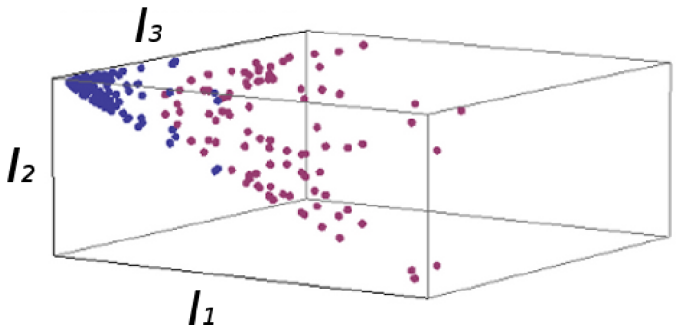

FIGURE 69. Sensor calibration library.
Each point in the current space corresponds to different neuron positions and firing magnitudes, (x, y, z, m). Shown in 3 of the 15 current recordings, I_1, I_2, and I_3. The blue points correspond to each neuron position shown in Fig. 68 all with magnitude m_1, while the purple points are for each position all with magnitude m_2, where $m_1 < m_2$.

value of 1:5, then for each current axis can be broken into 20 uniquely identifiable measurements. For the three currents illustrated in Fig. 69, there are $20^3 = 8000$ unique signals. For the 15 independent currents, there would be a total of 20^15 uniquely identifiable (x, y, z, m), well exceeding the number of somas in the region above the transistor.

However, as illustrated in Figure 69, the points in the calibration library do not span throughout the entire current space. Rather, the recordings (I_1, I_2, I_3), fall along a cone, leaving much of the current space empty. Therefore, for the square transistor, the number of signals which can uniquely be identified is significantly less than the 8000 maximum for 3 current recordings. Although the multi-terminal architecture with a square FET achieves some degree of separation of current measurements in the calibration library, it is desirable to have points which spread throughout a larger region of the current space in order to increase the number of signals that can be uniquely recorded.

Carbon Nanotube Multi-Terminal Transistor

We propose the fractal CNT transistor (Fig. 67d) will cause the measured currents to spread throughout the current space due to the complex network of resistance pathways causing exponential sensitivity to varying neuron positions. Previous research has shown exponential sensitivity exists for silicon transistors with chaotic channel resistances [228]. Additionally, CNTs have a very high channel conductance [229], which will further improve the sensitivity.

CNT transistors have a remarkable track record as reliable biosensors. Rosenblatt et al. (2002) first demonstrated electrolyte gated CNTs exhibit current-voltage responses similar to standard FETs [230]. Interconnected CNT transistors are

extremely sensitive to variations in electrolyte protein concentration through conductance changes [231]. CNTs encapsulated onto conventional MEAs for neural recordings decrease impedance and reduce electrical noise [154]. Intracellular recordings with CNT FETs can obtain sensitive low-noise recordings of the membrane potential [232].

Previous research has shown single CNT transistors measure a conductance of 30 nS $\pm$ 3 nS from an extracellular cardiomyocyte 18 μm away causing a gate voltage of 1 mV [229]. Using this, an estimate for the farthest distance we can record a 500 μV signal with a signal-to-noise ratio of 3 and assuming a $\sim 1/r$ potential fall off is 30 μm.

The proposed sensor would consist of a 16 x 1 array of horizontally aligned interconnected CNT transistors 30 μm x 30 μm spaced 50 μm apart and with each transistor having 16 terminals (Fig. 67e). The whole array would be capable of recording from an 800 μm x 50 μm x 30 μm volume of tissue at a rate of 2.5 kHz. The recording system would include high-pass filters at 3 kHz, amplifiers to give a signal gain of 100, and analog-to-digital conversion for recording on the computer.

The interconnected CNT transistor would provide another crucial improvement - a biophilic interface. When a typical probe is implanted into neural tissue, a glial scar is formed around the implant as the neurons recede from the probe surface [51]. The CNT array introduces nano-texture onto the implant surface which should slow glial scar formation and provide a biophilic interface for dendritic growth.

To verify the performance of our device we would carry out optical recordings in tandem with the electrical recordings from the CNT sensor [233] (Fig. 70). Cortical slices would be $\sim$400 μm thick from a transgenic mouse which expresses a fluorescent calcium indicator which 'lights up' when a neuron fires [234]. Neural firing activity would be induced across the cortical slice by changing concentrations in artificial

cerebrospinal fluid (ACSF). 2-photon imaging would record the locations of firing neurons and we would correlate it to the electrical recordings made on our CNT sensor.

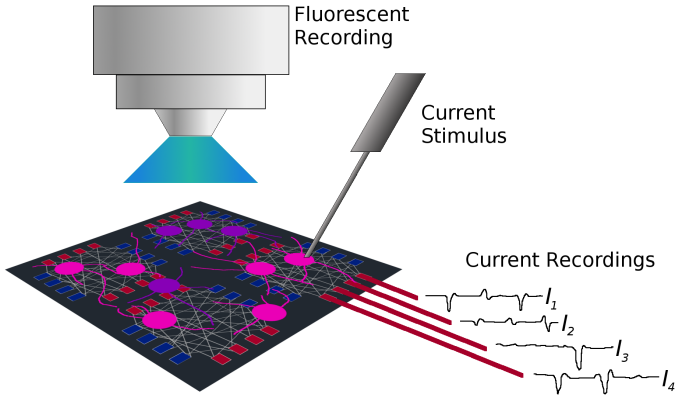

FIGURE 70. Validation testing of CNT transistor sensor.
Verification of the CNT sensor would be achieved through dual optical (2-photon) and electrical recordings (our CNT sensor).

In conclusion, we expect a multi-terminal sensor featuring a fractal network of semiconducting CNTs will greatly enhance the number of individual neuron firing events that can be recorded simutaneously both in vitro and in vivo. Development of this device has the potential to greatly increase the recording capabilities of extracellular electrodes and assist in the advancement of understanding neurological disorders such as Alzheimer's and depression.

CHAPTER V

CONCLUSIONS

This chapter briefly highlights the main conclusions from this thesis.

In Chapter 2, we showed how subretinal implants which use fractal electrodes give a remarkable restoration in visual acuity up to 20/80, whereas current devices return an acuity of 20/546 at best. We began by applying equivalent voltages to square, grid, and fractal electrodes on a 20 μm photodiode. Each design blocked the same amount of light from entering the photodiode. From our simulations, we showed that a single photodiode featuring a fractal electrode can stimulate all neighboring neurons within the open-circuit voltage of a typical silicon photodiode. In contrast, the square design uses 3 photodiodes to stimulate all neighboring neurons which leads to a reduction in the restored acuity. Next, we added into our simulations the photodiode response to incoming radiation in order to more accurately model the voltages applied to the square and fractal electrodes. We showed that by optimizing the fractal electrode, 74% less irradiation was required to stimulate all neighboring neurons. At the threshold irradiation in which the fractal stimulated all nearby neurons, the square only stimulated $\sim$10%, leading to a reduction in the perceived image quality. The square thus required more radiation to stimulate all nearby neurons, with the complication that it was very near the maximum permissible safety limit of light which can enter the eye. In contrast, the radiation requirements for the fractal guaranteed long-term, safe operation of the implant. Finally, we showed that tissue heating due to Joule heating from ionic currents in the extracellular space induced by applied voltages on the electrodes was well within the safety limits for the fractal electrode.

In Chapter 3, we tested if dissociated retinal neurons are biocompatible with vertically aligned carbon nanotubes (VACNTs) prepared from Fe catalyst. Aluminum adhesive layer was used to improve the adhesion of VACNTs to the substrate. We then compared these two preparations to VACNTs functionalized through plasma functionalization. We found that unfunctionalized VACNTs prepared from Fe catalyst with the Al adhesive layer led to significantly increased neurite outgrowth compared to the other 3 categories. Thus providing a stable interface material for use in neural implants. Additionally, we conducted preliminary experiments investigating the response of retinal neurons on rows of VACNTs and VACNT fractals. We found: (1) neurons preferentially adhere to and grow neurites on the VACNTs over the SiO_2 substrate, (2) neurites prefer to extend along the edges of the VACNT geometries, and (3) glia can be herded in between the VACNTs. Thus, fractal VACNT electrodes are an excellent interface because neurons will adhere strongly to the top of the electrode, the large number of internal edges from fractals will lead to extensive neurite outgrowth, and glia scars will not form due to the inter-electrode gaps existing in the fractal design.

In Chapter 4, we proposed a novel field effect transistor (FET) to uniquely isolate the location and voltage magnitude of a firing neuron. A standard FET for neural recording features a drain terminal and a source terminal. The firing neuron acts as the gate. Our design uses multiple drain and source terminals to build up a calibration library of current 'fingerprints' which uniquely indentify the location and voltage magnitude of a firing neuron. This could allow for detecting the location and voltage magnitude of thousands of neurons simutaneously, whereas a single standard FET used in today's recording devices can only detect the voltage magnitude of a single neuron. In order to improve the sensitivity of our device, we proposed replacing

the silicon channel with a fractal network of semiconducting carbon nanotubes. This fractal network features a complex network of resistance pathways which would lead to exponential sensitivity in detecting the neuron's location. Demonstration of the proposed device could revolutionize our understanding of the brain; current devices can only record up to 100 neurons simutaneously, wheras this device would allow for recording from thousands or more neurons.

Limitations in the performance of current generation stimulating and recording neural implants are mainly due to a non-ideal neuron-electrode interface. The research conducted within this thesis outlined critical improvements in neural stimulation, neuron adhesion to the interface, and neuron recording which can be achieved by adopting fractal geometries for these implants. Our lab is currently building off these ideas to create a functioning retinal implant which can deliver a voltage to the fractal electrodes both in vitro and in vivo. In the near future, we expect to demonstrate an improvement in restored acuity in animal trials. However, many of the improvements discussed here are not only limited to retinal implants. Full integration of the fractal electrode, the carbon nanotubes, and the novel sensor presented in this thesis could, in fact, lead to a dramatic improvement in our understanding of the brain and our in our ability to restore function to patients of neural diseases.

REFERENCES CITED

[1] Mark A. Wood and Kenneth A. Ellenbogen. Cardiac Pacemakers From the Patients Perspective. *Circulation*, 105(18):2136–2138, May 2002.

[2] Cochlear Implants. Retrieved from: https://www.nidcd.nih.gov/health/cochlear-implants. Date accessed: May 21, 2017, August 2015.

[3] Medtronic Innovation in Deep Brain Stimulation. Retrieved from: https://www.medtronicdbs.com/why-dbs/innovation-leader/index.htm. Date accessed: May 21, 2017, 2016.

[4] Helen S. Mayberg, Andres M. Lozano, Valerie Voon, Heather E. McNeely, David Seminowicz, Clement Hamani, Jason M. Schwalb, and Sidney H. Kennedy. Deep Brain Stimulation for Treatment-Resistant Depression. *Neuron*, 45(5):651–660, March 2005.

[5] Press Announcements - FDA allows marketing of first prosthetic arm that translates signals from person's muscles to perform complex tasks. Retreived from: www.fda.gov/NewsEvents/Newsroom/PressAnnouncements/ucm396688.htm Date accessed: November 21, 2016, May 2014.

[6] Eberhart Zrenner. Will Retinal Implants Restore Vision? *Science*, 295(5557):1022–1025, February 2002.

[7] W. J. Watterson, R. D. Montgomery, and R. P. Taylor. Fractal Electrodes as a Generic Interface for Stimulating Neurons. *Scientific Reports*, 7, July 2017.

[8] William Watterson, Rick Montgomery, and Richard Taylor. Improved visual acuity using subretinal implants featuring fractal electrodes. *IEEE Transactions on Biomedical Engineering*, (In publication.).

[9] William Watterson, Saba Moslehi, Kara Zappitelli, Julian Smith, David Miller, Julie Chouinard, Stephen Golledge, Richard Taylor, Maria-Thereza Perez, and Benjamin Aleman. Biocompatibility of vertically aligned carbon nanotubes with retinal neurons. *IOP Nanotechnology*, (In publication.).

[10] Arturo Santos, Mark S. Humayun, Eugene de Juan, Robert J. Greenburg, Marta J. Marsh, Ingrid B. Klock, and Ann H. Milam. Preservation of the Inner Retina in Retinitis Pigmentosa: A Morphometric Analysis. *Archives of Ophthalmology*, 115(4):511–515, April 1997.

[11] Sy Kim, S Sadda, J Pearlman, MS Humayun, E de Juan, and Wr Green. Morphometric analysis of the macular retina from eyes with disciform age-related macular degeneration. *LWW*, 2002.

[12] Dyonne T. Hartong, Eliot L. Berson, and Thaddeus P. Dryja. Retinitis pigmentosa. *The Lancet*, 368(9549):1795–1809, 2006.

[13] Sandee Grover, Gerald A. Fishman, Kenneth R. Alexander, Robert J. Anderson, and Deborah J. Derlacki. Visual Acuity Impairment in Patients with Retinitis Pigmentosa. *Ophthalmology*, 103(10):1593–1600, October 1996.

[14] Age-Related Macular Degeneration: Facts & Figures. Retreived from: http://www.brightfocus.org/macular/article/age-related-macular-facts-figures Date accessed: May 20, 2017, July 2015.

[15] The Eye Diseases Prevalence Research Group. Causes and Prevalence of Visual Impairment Among Adults in the United States. *Archives of Ophthalmology*, 122(4):477–485, April 2004.

[16] Facts About Age-Related Macular Degeneration | National Eye Institute. Retrieved from: `https://nei.nih.gov/health/maculardegen/armd_facts` Date accessed: May 20, 2017.

[17] Mark S. Humayun, Eugene de Juan Jr, James D. Weiland, Gislin Dagnelie, Steve Katona, Robert Greenberg, and Satoshi Suzuki. Pattern electrical stimulation of the human retina. *Vision research*, 39(15):2569–2576, 1999.

[18] Alison Harman, Brett Abrahams, Stephen Moore, and Robert Hoskins. Neuronal density in the human retinal ganglion cell layer from 1677 years. *The Anatomical Record*, 260(2):124–131, October 2000.

[19] Mark S. Humayun, James D. Weiland, Gildo Y. Fujii, Robert Greenberg, Richard Williamson, Jim Little, Brian Mech, Valerie Cimmarusti, Gretchen Van Boemel, Gislin Dagnelie, and Eugene de Juan Jr. Visual perception in a blind subject with a chronic microelectronic retinal prosthesis. *Vision Research*, 43(24):2573–2581, November 2003.

[20] Avi Caspi, Jessy D. Dorn, Kelly H. McClure, Mark S. Humayun, Robert J. Greenberg, and Matthew J. McMahon. Feasibility study of a retinal prosthesis: spatial vision with a 16-electrode implant. *Archives of Ophthalmology*, 127(4):398–401, 2009.

[21] Mark S. Humayun, Jessy D. Dorn, Lyndon da Cruz, Gislin Dagnelie, Jos-Alain Sahel, Paulo E. Stanga, Artur V. Cideciyan, Jacque L. Duncan, Dean Eliott, Eugene Filley, Allen C. Ho, Arturo Santos, Avinoam B. Safran, Aries Arditi, Lucian V. Del Priore, and Robert J. Greenberg. Interim Results from the International Trial of Second Sight's Visual Prosthesis. *Ophthalmology*, 119(4):779–788, April 2012.

[22] Douglas Yanai, James D. Weiland, Manjunatha Mahadevappa, Robert J. Greenberg, Ione Fine, and Mark S. Humayun. Visual Performance Using a Retinal Prosthesis in Three Subjects With Retinitis Pigmentosa. *American Journal of Ophthalmology*, 143(5):820–827.e2, May 2007.

[23] Lyndon da Cruz, Brian F. Coley, Jessy Dorn, Francesco Merlini, Eugene Filley, Punita Christopher, Fred K. Chen, Varalakshmi Wuyyuru, Jose Sahel, Paulo Stanga, and others. The Argus II epiretinal prosthesis system allows letter and word reading and long-term function in patients with profound vision loss. *British Journal of Ophthalmology*, pages bjophthalmol–2012, 2013.

[24] Ralf Hornig, Marcus Dapper, Eric Le Joliff, Robert Hill, Khalid Ishaque, Christoph Posch, Ryad Benosman, Yannick LeMer, Jos-Alain Sahel, and Serge Picaud. Pixium Vision: First Clinical Results and Innovative Developments. In Veit Peter Gabel, editor, *Artificial Vision*, pages 99–113. Springer International Publishing, Cham, 2017. DOI: 10.1007/978-3-319-41876-6_8.

[25] Alan Y Chow and Vincent Y Chow. Subretinal electrical stimulation of the rabbit retina. *Neuroscience Letters*, 225(1):13–16, March 1997.

[26] Alan Y. Chow, Vincent Y. Chow, Kirk H. Packo, John S. Pollack, Gholam A. Peyman, and Ronald Schuchard. The Artificial Silicon Retina Microchip for the Treatment of VisionLoss From Retinitis Pigmentosa. *Archives of Ophthalmology*, 122(4):460–469, April 2004.

[27] A. Y. Chow, M. T. Pardue, V. Y. Chow, G. A. Peyman, Chanping Liang, J. I. Perlman, and N. S. Peachey. Implantation of silicon chip microphotodiode arrays into the cat subretinal space. *IEEE Transactions on Neural Systems and Rehabilitation Engineering*, 9(1):86–95, March 2001.

[28] Harsha Kasi, Willyan Hasenkamp, Gregoire Cosendai, Arnaud Bertsch, and Philippe Renaud. Simulation of epiretinal prostheses - Evaluation of geometrical factors affecting stimulation thresholds. *Journal of NeuroEngineering and Rehabilitation*, 8:44, August 2011.

[29] E. Zrenner, A. Stett, S. Weiss, R. B. Aramant, E. Guenther, K. Kohler, K. D. Miliczek, M. J. Seiler, and H. Haemmerle. Can subretinal microphotodiodes successfully replace degenerated photoreceptors? *Vision Research*, 39(15):2555–2567, July 1999.

[30] Florian Gekeler, Karin Kobuch, Hartmut Normann Schwahn, Alfred Stett, Kei Shinoda, and Eberhart Zrenner. Subretinal electrical stimulation of the rabbit retina with acutely implanted electrode arrays. *Graefe's Archive for Clinical and Experimental Ophthalmology = Albrecht Von Graefes Archiv Fur Klinische Und Experimentelle Ophthalmologie*, 242(7):587–596, July 2004.

[31] D. Besch, H. Sachs, P. Szurman, D. Glicher, R. Wilke, S. Reinert, E. Zrenner, K. U. Bartz-Schmidt, and F. Gekeler. Extraocular surgery for implantation of an active subretinal visual prosthesis with external connections: feasibility and outcome in seven patients. *British Journal of Ophthalmology*, 92(10):1361–1368, October 2008.

[32] E. Zrenner, K. U. Bartz-Schmidt, H. Benav, D. Besch, A. Bruckmann, V.-P. Gabel, F. Gekeler, U. Greppmaier, A. Harscher, S. Kibbel, J. Koch, A. Kusnyerik, T. Peters, K. Stingl, H. Sachs, A. Stett, P. Szurman, B. Wilhelm, and R. Wilke. Subretinal electronic chips allow blind patients to read letters and combine them to words. *Proceedings of the Royal Society B: Biological Sciences*, 278(1711):1489–1497, May 2011.

[33] Katarina Stingl, Karl Ulrich Bartz-Schmidt, Dorothea Besch, Angelika Braun, Anna Bruckmann, Florian Gekeler, Udo Greppmaier, Stephanie Hipp, Gernot Hrtdrfer, Christoph Kernstock, Assen Koitschev, Akos Kusnyerik, Helmut Sachs, Andreas Schatz, Krunoslav T. Stingl, Tobias Peters, Barbara Wilhelm, and Eberhart Zrenner. Artificial vision with wirelessly powered subretinal electronic implant alpha-IMS. *Proc. R. Soc. B*, 280(1757):20130077, April 2013.

[34] Katarina Stingl, Karl Ulrich Bartz-Schmidt, Dorothea Besch, Caroline K. Chee, Charles L. Cottriall, Florian Gekeler, Markus Groppe, Timothy L. Jackson, Robert E. MacLaren, Assen Koitschev, Akos Kusnyerik, James Neffendorf, Janos Nemeth, Mohamed Adheem Naser Naeem, Tobias Peters, James D. Ramsden, Helmut Sachs, Andrew Simpson, Mandeep S. Singh, Barbara Wilhelm, David Wong, and Eberhart Zrenner. Subretinal Visual Implant Alpha IMS Clinical trial interim report. *Vision Research*, 111, Part B:149–160, June 2015.

[35] Daniel Palanker, Alexander Vankov, Phil Huie, and Stephen Baccus. Design of a high-resolution optoelectronic retinal prosthesis. *Journal of Neural Engineering*, 2(1):S105–S120, March 2005.

[36] Keith Mathieson, James Loudin, Georges Goetz, Philip Huie, Lele Wang, Theodore I. Kamins, Ludwig Galambos, Richard Smith, James S. Harris, Alexander Sher, and Daniel Palanker. Photovoltaic retinal prosthesis with high pixel density. *Nature Photonics*, 6(6):391–397, May 2012.

[37] Lele Wang, K. Mathieson, T. I. Kamins, J. D. Loudin, L. Galambos, G. Goetz, A. Sher, Y. Mandel, P. Huie, D. Lavinsky, J. S. Harris, and D. V. Palanker. Photovoltaic retinal prosthesis: implant fabrication and performance. *Journal of Neural Engineering*, 9(4):046014, 2012.

[38] J. D. Loudin, D. M. Simanovskii, K. Vijayraghavan, C. K. Sramek, A. F. Butterwick, P. Huie, G. Y. McLean, and D. V. Palanker. Optoelectronic retinal prosthesis: system design and performance. *Journal of Neural Engineering*, 4(1):S72, 2007.

[39] J. D. Loudin, S. F. Cogan, K. Mathieson, A. Sher, and D. V. Palanker. Photodiode Circuits for Retinal Prostheses. *IEEE Transactions on Biomedical Circuits and Systems*, 5(5):468–480, October 2011.

[40] A. Butterwick, P. Huie, B. W. Jones, R. E. Marc, M. Marmor, and D. Palanker. Effect of shape and coating of a subretinal prosthesis on its integration with the retina. *Experimental Eye Research*, 88(1):22–29, January 2009.

[41] Henri Lorach, Georges Goetz, Richard Smith, Xin Lei, Yossi Mandel, Theodore Kamins, Keith Mathieson, Philip Huie, James Harris, Alexander Sher, and Daniel Palanker. Photovoltaic restoration of sight with high visual acuity. *Nature Medicine*, 21(5):476–482, May 2015.

[42] D Johnston and S. M. S. Wu. *Foundations of Cellular Neurophysiology*. MIT press, Cambridge, 1995.

[43] P. Werginz, H. Benav, E. Zrenner, and F. Rattay. Modeling the response of ON and OFF retinal bipolar cells during electric stimulation. *Vision Research*, 111:170–181, June 2015.

[44] R Heidelberger and G Matthews. Calcium influx and calcium current in single synaptic terminals of goldfish retinal bipolar neurons. *The Journal of Physiology*, 447(1):235–256, February 1992.

[45] A. L. Hodgkin and B. Katz. The effect of sodium ions on the electrical activity of the giant axon of the squid. *The Journal of Physiology*, 108(1):37–77, March 1949.

[46] F. Rattay. Analysis of Models for External Stimulation of Axons. *IEEE Transactions on Biomedical Engineering*, BME-33(10):974–977, October 1986.

[47] F. Rattay and S. Resatz. Effective electrode configuration for selective stimulation with inner eye prostheses. *IEEE Transactions on Biomedical Engineering*, 51(9):1659–1664, September 2004.

[48] Max Eickenscheidt and Gnther Zeck. Action potentials in retinal ganglion cells are initiated at the site of maximal curvature of the extracellular potential. *Journal of Neural Engineering*, 11(3):036006, 2014.

[49] Nicola J. Allen and Ben A. Barres. Neuroscience: gliamore than just brain glue. *Nature*, 457(7230):675–677, 2009.

[50] Elena Vecino, F. David Rodriguez, Noelia Ruzafa, Xandra Pereiro, and Sansar C. Sharma. Glianeuron interactions in the mammalian retina. *Progress in Retinal and Eye Research*, 51:1–40, March 2016.

[51] Vadim S. Polikov, Patrick A. Tresco, and William M. Reichert. Response of brain tissue to chronically implanted neural electrodes. *Journal of Neuroscience Methods*, 148(1):1–18, October 2005.

[52] J. N. Turner, W. Shain, D. H. Szarowski, M. Andersen, S. Martins, M. Isaacson, and H. Craighead. Cerebral Astrocyte Response to Micromachined Silicon Implants. *Experimental Neurology*, 156(1):33–49, March 1999.

[53] J. E. Sanders, C. E. Stiles, and C. L. Hayes. Tissue response to single-polymer fibers of varying diameters: evaluation of fibrous encapsulation and macrophage density. *Journal of biomedical materials research*, 52(1):231–237, 2000.

[54] Takashi D. Yoshida Kozai, Nicholas B. Langhals, Paras R. Patel, Xiaopei Deng, Huanan Zhang, Karen L. Smith, Joerg Lahann, Nicholas A. Kotov, and Daryl R. Kipke. Ultrasmall implantable composite microelectrodes with bioactive surfaces for chronic neural interfaces. *Nature materials*, 11(12):1065–1073, December 2012.

[55] Jonas Thelin, Henrik Jrntell, Elia Psouni, Martin Garwicz, Jens Schouenborg, Nils Danielsen, and Cecilia Eriksson Linsmeier. Implant Size and Fixation Mode Strongly Influence Tissue Reactions in the CNS. *PLOS ONE*, 6(1):e16267, January 2011.

[56] Huanan Zhang, Paras R. Patel, Zhixing Xie, Scott D. Swanson, Xueding Wang, and Nicholas A. Kotov. Tissue-Compliant Neural Implants from Microfabricated Carbon Nanotube Multilayer Composite. *ACS Nano*, 7(9):7619–7629, September 2013.

[57] Yinghui Zhong and Ravi V. Bellamkonda. Dexamethasone-coated neural probes elicit attenuated inflammatory response and neuronal loss compared to uncoated neural probes. *Brain Research*, 1148:15–27, May 2007.

[58] Galle Piret, Maria-Thereza Perez, and Christelle N. Prinz. Support of Neuronal Growth Over Glial Growth and Guidance of Optic Nerve Axons by Vertical Nanowire Arrays. *ACS Applied Materials & Interfaces*, 7(34):18944–18948, September 2015.

[59] RichardH. Masland. The Neuronal Organization of the Retina. *Neuron*, 76(2):266–280, October 2012.

[60] Heinz Wassle, Christian Puller, Frank Mller, and Silke Haverkamp. Cone Contacts, Mosaics, and Territories of Bipolar Cells in the Mouse Retina. *Journal of Neuroscience*, 29(1):106–117, January 2009.

[61] Tim Gollisch and Markus Meister. Eye Smarter than Scientists Believed: Neural Computations in Circuits of the Retina. *Neuron*, 65(2):150–164, January 2010.

[62] Stuart F. Cogan. Neural Stimulation and Recording Electrodes. *Annual Review of Biomedical Engineering*, 10(1):275–309, 2008.

[63] Daniel R. Merrill, Marom Bikson, and John G. R. Jefferys. Electrical stimulation of excitable tissue: design of efficacious and safe protocols. *Journal of Neuroscience Methods*, 141(2):171–198, February 2005.

[64] T. L. Rose and L. S. Robblee. Electrical stimulation with Pt electrodes. VIII. Electrochemically safe charge injection limits with 0.2 ms pulses. *IEEE transactions on bio-medical engineering*, 37(11):1118–1120, November 1990.

[65] X. Beebe and T. L. Rose. Charge injection limits of activated iridium oxide electrodes with 0.2 ms pulses in bicarbonate buffered saline (neurological stimulation application). *IEEE Transactions on Biomedical Engineering*, 35(6):494–495, June 1988.

[66] J.D. Weiland, D.J. Anderson, and M.S. Humayun. In vitro electrical properties for iridium oxide versus titanium nitride stimulating electrodes. *IEEE Transactions on Biomedical Engineering*, 49(12):1574–1579, December 2002.

[67] Sandeep Negi, Rajmohan Bhandari, Loren Rieth, Rick Van Wagenen, and Florian Solzbacher. Neural electrode degradation from continuous electrical stimulation: Comparison of sputtered and activated iridium oxide. *Journal of Neuroscience Methods*, 186(1):8–17, January 2010.

[68] Stuart F. Cogan, Andrew A. Guzelian, William F. Agnew, Ted G. H. Yuen, and Douglas B. McCreery. Over-pulsing degrades activated iridium oxide films used for intracortical neural stimulation. *Journal of Neuroscience Methods*, 137(2):141–150, August 2004.

[69] J. D. Weiland and D. J. Anderson. Chronic neural stimulation with thin-film, iridium oxide electrodes. *IEEE Transactions on Biomedical Engineering*, 47(7):911–918, July 2000.

[70] Tamir Gabay, Moti Ben-David, Itshak Kalifa, Raya Sorkin, Zeev R Abrams, Eshel Ben-Jacob, and Yael Hanein. Electro-chemical and biological properties of carbon nanotube based multi-electrode arrays. *Nanotechnology*, 18(3):035201, January 2007.

[71] Tobias Nyberg, Akiyoshi Shimada, and Keiichi Torimitsu. Ion conducting polymer microelectrodes for interfacing with neural networks. *Journal of Neuroscience Methods*, 160(1):16–25, February 2007.

[72] X.T. Cui and D.D. Zhou. Poly (3,4-Ethylenedioxythiophene) for Chronic Neural Stimulation. *IEEE Transactions on Neural Systems and Rehabilitation Engineering*, 15(4):502–508, December 2007.

[73] Xiliang Luo, Cassandra L. Weaver, David D. Zhou, Robert Greenberg, and Xinyan T. Cui. Highly stable carbon nanotube doped poly(3,4-ethylenedioxythiophene) for chronic neural stimulation. *Biomaterials*, 32(24):5551–5557, August 2011.

[74] Moshe David-Pur, Lilach Bareket-Keren, Giora Beit-Yaakov, Dorit Raz-Prag, and Yael Hanein. All-carbon-nanotube flexible multi-electrode array for neuronal recording and stimulation. *Biomedical Microdevices*, 16(1):43–53, February 2014.

[75] Shyh-Chyang Luo, Emril Mohamed Ali, Natalia C. Tansil, Hsiao-hua Yu, Shujun Gao, Eric A. B. Kantchev, and Jackie Y. Ying. Poly (3,4-ethylenedioxythiophene) (PEDOT) Nanobiointerfaces: Thin, Ultrasmooth, and Functionalized PEDOT Films with in Vitro and in Vivo Biocompatibility. *Langmuir*, 24(15):8071–8077, August 2008.

[76] Jonathon Myers, Miguel Santiago-Medina, and Timothy M. Gomez. Regulation of axonal outgrowth and pathfinding by integrinecm interactions. *Developmental Neurobiology*, 71(11):901–923, November 2011.

[77] Stephan Huveneers, Hoa Truong, and Erik H. J. Danen. Integrins: Signaling, disease, and therapy. *International Journal of Radiation Biology*, 83(11-12):743–751, January 2007.

[78] R. Zaidel-Bar, M. Cohen, L. Addadi, and B. Geiger. Hierarchical assembly of cellmatrix adhesion complexes. *Biochemical Society Transactions*, 32(3):416–420, June 2004.

[79] Erik W Dent and Frank B Gertler. Cytoskeletal Dynamics and Transport in Growth Cone Motility and Axon Guidance. *Neuron*, 40(2):209–227, October 2003.

[80] Michael Rabe, Dorinel Verdes, and Stefan Seeger. Understanding protein adsorption phenomena at solid surfaces. *Advances in Colloid and Interface Science*, 162(1-2):87–106, February 2011.

[81] P. Roach, T. Parker, N. Gadegaard, and M.R. Alexander. Surface strategies for control of neuronal cell adhesion: A review. *Surface Science Reports*, 65(6):145–173, June 2010.

[82] Rebecca Akers, Deane Mosher, Deane, and Jack Lilien. Promotion of Retinal Neurite Outgrowth by Substratum-Bound Fibronectin. *Developmental Biology*, 86:179–188, 1981.

[83] Frederick Grinnell and M. K. Feld. Fibronectin adsorption on hydrophilic and hydrophobic surfaces detected by antibody binding and analyzed during cell adhesion in serum-containing medium. *J biol chem*, 257(9):4888–4893, 1982.

[84] Neil Smalheiser, Stanley Crain, and Lola Reid, Lola. Laminin as a substrate for retinal axons in vitro. *Developmental Brain Research*, 12(1984):136–140, 1984.

[85] J Cohen, J.F. Burne, J. Winter, and P. Bartlett. Retinal ganglion cells lose response to laminin with maturation. *Nature*, 322:465–467, July 1986.

[86] Ivar Kljavin and Thomas Reh. Mller Cells Are a Preferred Substrate for in vitro Neurite Extension by Rod Photoreceptor Cells. *The Journal of Neuroscience*, 11(10):2985–2994, October 1991.

[87] E. Freire. Structure of laminin substrate modulates cellular signaling for neuritogenesis. *Journal of Cell Science*, 115(24):4867–4876, December 2002.

[88] Roy Biran, Ken Webb, Mark D. Noble, and Patrick A. Tresco. Surfactant-immobilized fibronectin enhances bioactivity and regulates sensory neurite outgrowth. *Journal of biomedical materials research*, 55(1):1–12, 2001.

[89] Shreyas Kuddannaya, Jingnan Bao, and Yilei Zhang. Enhanced In Vitro Biocompatibility of Chemically Modified Poly(dimethylsiloxane) Surfaces for Stable Adhesion and Long-term Investigation of Brain Cerebral Cortex Cells. *ACS Applied Materials & Interfaces*, 7(45):25529–25538, November 2015.

[90] Yue Zhang, Chou Chai, Xue Song Jiang, Swee Hin Teoh, and Kam W. Leong. Fibronectin immobilized by covalent conjugation or physical adsorption shows different bioactivity on aminated-PET. *Materials Science and Engineering: C*, 27(2):213–219, March 2007.

[91] Karine Vallires, Pascale Chevallier, Christian Sarra-Bournet, Stphane Turgeon, and Gatan Laroche. AFM Imaging of Immobilized Fibronectin: Does the Surface Conjugation Scheme Affect the Protein Orientation/Conformation? *Langmuir*, 23(19):9745–9751, September 2007.

[92] Joannie Roy, Timothy E. Kennedy, and Santiago Costantino. Engineered cell culture substrates for axon guidance studies: moving beyond proof of concept. *Lab on a Chip*, 13(4):498–508, January 2013.

[93] M. Scholl, C. Sprssler, M. Denyer, M. Krause, K. Nakajima, A. Maelicke, Wolfgang Knoll, and Andreas Offenhusser. Ordered networks of rat hippocampal neurons attached to silicon oxide surfaces. *Journal of neuroscience methods*, 104(1):65–75, 2000.

[94] Conrad D. James, Robert Davis, M. Meyer, AATA Turner, SATS Turner, GAWG Withers, LAKL Kam, GABG Banker, HACH Craighead, MAIM Issacson, and others. Aligned microcontact printing of micrometer-scale poly-L-lysine structures for controlled growth of cultured neurons on planar microelectrode arrays. *Biomedical Engineering, IEEE Transactions on*, 47(1):17–21, 2000.

[95] L. Kam, W. Shain, J. N. Turner, and R. Bizios. Axonal outgrowth of hippocampal neurons on micro-scale networks of polylysine-conjugated laminin. *Biomaterials*, 22(10):1049–1054, May 2001.

[96] Min Jee Jang and Yoonkey Nam. Geometric effect of cell adhesive polygonal micropatterns on neuritogenesis and axon guidance. *Journal of Neural Engineering*, 9(4):046019, 2012.

[97] Stephan KW Dertinger, Xingyu Jiang, Zhiying Li, Venkatesh N. Murthy, and George M. Whitesides. Gradients of substrate-bound laminin orient axonal specification of neurons. *Proceedings of the National Academy of Sciences*, 99(20):12542–12547, 2002.

[98] Ryosuke Ogaki, Morgan Alexander, and Peter Kingshott. Chemical patterning in biointerface science. *Materials Today*, 13(4):22–35, April 2010.

[99] Megan S. Lord, Morten Foss, and Flemming Besenbacher. Influence of nanoscale surface topography on protein adsorption and cellular response. *Nano Today*, 5(1):66–78, February 2010.

[100] A. Rajnicek, Stephen Britland, and C. McCaig. Contact guidance of CNS neurites on grooved quartz: influence of groove dimensions, neuronal age and cell type. *Journal of cell science*, 110(23):2905–2913, 1997.

[101] Melissa J. Mahoney, Ruth R. Chen, Jian Tan, and W. Mark Saltzman. The influence of microchannels on neurite growth and architecture. *Biomaterials*, 26(7):771–778, March 2005.

[102] N M Dowell-Mesfin, M-A Abdul-Karim, A M P Turner, S Schanz, H G Craighead, B Roysam, J N Turner, and W Shain. Topographically modified surfaces affect orientation and growth of hippocampal neurons. *Journal of Neural Engineering*, 1(2):78–90, June 2004.

[103] Roy M. Smeal, Richard Rabbitt, Roy Biran, and Patrick A. Tresco. Substrate Curvature Influences the Direction of Nerve Outgrowth. *Annals of Biomedical Engineering*, 33(3):376–382, January 2005.

[104] Y. W. Fan, F. Z. Cui, S. P. Hou, Q. Y. Xu, L. N. Chen, and I.-S. Lee. Culture of neural cells on silicon wafers with nano-scale surface topograph. *Journal of neuroscience methods*, 120(1):17–23, 2002.

[105] Saida P. Khan, Gregory G. Auner, and Golam M. Newaz. Influence of nanoscale surface roughness on neural cell attachment on silicon. *Nanomedicine: Nanotechnology, Biology and Medicine*, 1(2):125–129, June 2005.

[106] V. Brunetti, G. Maiorano, L. Rizzello, B. Sorce, S. Sabella, R. Cingolani, and P. P. Pompa. Neurons sense nanoscale roughness with nanometer sensitivity. *Proceedings of the National Academy of Sciences*, 107(14):6264–6269, April 2010.

[107] K. Rechendorff, M. B. Hovgaard, M. Foss, V. P. Zhdanov, and F. Besenbacher. Enhancement of protein adsorption induced by surface roughness. *Langmuir: the ACS journal of surfaces and colloids*, 22(26):10885–10888, December 2006.

[108] Kaiyong Cai, Jrg Bossert, and Klaus D. Jandt. Does the nanometre scale topography of titanium influence protein adsorption and cell proliferation? *Colloids and Surfaces. B, Biointerfaces*, 49(2):136–144, May 2006.

[109] Francesco Gentile, Rebecca Medda, Ling Cheng, Edmondo Battista, Pasquale E. Scopelliti, Paolo Milani, Elisabetta A. Cavalcanti-Adam, and Paolo Decuzzi. Selective modulation of cell response on engineered fractal silicon substrates. *Scientific Reports*, 3, March 2013.

[110] F. Yang, R. Murugan, S. Wang, and S. Ramakrishna. Electrospinning of nano/micro scale poly(l-lactic acid) aligned fibers and their potential in neural tissue engineering. *Biomaterials*, 26(15):2603–2610, May 2005.

[111] Jae Y. Lee, Chris A. Bashur, Aaron S. Goldstein, and Christine E. Schmidt. Polypyrrole-coated electrospun PLGA nanofibers for neural tissue applications. *Biomaterials*, 30(26):4325–4335, September 2009.

[112] Tzahi Cohen-Karni, Quan Qing, Qiang Li, Ying Fang, and Charles M. Lieber. Graphene and Nanowire Transistors for Cellular Interfaces and Electrical Recording. *Nano Letters*, 10(3):1098–1102, March 2010.

[113] Amel Bendali, Lucas H. Hess, Max Seifert, Valerie Forster, Anne-Fleur Stephan, Jose A. Garrido, and Serge Picaud. Purified Neurons can Survive on Peptide-Free Graphene Layers. *Advanced Healthcare Materials*, 2(7):929–933, July 2013.

[114] Chong Xie, Lindsey Hanson, Wenjun Xie, Ziliang Lin, Bianxiao Cui, and Yi Cui. Noninvasive Neuron Pinning with Nanopillar Arrays. *Nano Letters*, 10(10):4020–4024, October 2010.

[115] Jacob T. Robinson, Marsela Jorgolli, Alex K. Shalek, Myung-Han Yoon, Rona S. Gertner, and Hongkun Park. Vertical nanowire electrode arrays as a scalable platform for intracellular interfacing to neuronal circuits. *Nature Nanotechnology*, 7(3):180–184, January 2012.

[116] Christelle N Prinz. Interactions between semiconductor nanowires and living cells. *Journal of Physics: Condensed Matter*, 27(23):233103, June 2015.

[117] Pouria Fattahi, Guang Yang, Gloria Kim, and Mohammad Reza Abidian. A Review of Organic and Inorganic Biomaterials for Neural Interfaces. *Advanced Materials*, 26(12):1846–1885, March 2014.

[118] Natalia Gomez, Shaochen Chen, and Christine E. Schmidt. Polarization of hippocampal neurons with competitive surface stimuli: contact guidance cues are preferred over chemical ligands. *Journal of The Royal Society Interface*, 4(13):223–233, April 2007.

[119] A. P. Balgude, X. Yu, A. Szymanski, and R. V. Bellamkonda. Agarose gel stiffness determines rate of DRG neurite extension in 3d cultures. *Biomaterials*, 22(10):1077–1084, May 2001.

[120] Lisa A. Flanagan, Yo-El Ju, Beatrice Marg, Miriam Osterfield, and Paul A. Janmey. Neurite branching on deformable substrates. *Neuroreport*, 13(18):2411–2415, December 2002.

[121] Harini G. Sundararaghavan, Gary A. Monteiro, Bonnie L. Firestein, and David I. Shreiber. Neurite growth in 3d collagen gels with gradients of mechanical properties. *Biotechnology and Bioengineering*, 102(2):632–643, February 2009.

[122] Christine E. Schmidt, Venkatram R. Shastri, Joseph P. Vacanti, and Robert Langer. Stimulation of neurite outgrowth using an electrically conducting polymer. *Proceedings of the National Academy of Sciences*, 94(17):8948–8953, 1997.

[123] Ann M. Rajnicek, Kenneth R. Robinson, and Colin D. McCaig. The Direction of Neurite Growth in a Weak DC Electric Field Depends on the Substratum: Contributions of Adhesivity and Net Surface Charge. *Developmental Biology*, 203(2):412–423, November 1998.

[124] T. M. Barnes, J. van de Lagemaat, D. Levi, G. Rumbles, T. J. Coutts, C. L. Weeks, D. A. Britz, I. Levitsky, J. Peltola, and P. Glatkowski. Optical characterization of highly conductive single-wall carbon-nanotube transparent electrodes. *Physical Review B*, 75(23):235410, June 2007.

[125] S. V. Mahajan, S. A. Hasan, J. Cho, M. S. P. Shaffer, A. R. Boccaccini, and J. H. Dickerson. Carbon nanotubenanocrystal heterostructures fabricated by electrophoretic deposition. *Nanotechnology*, 19(19):195301, 2008.

[126] Ronald J. Warzoha, Di Zhang, Gang Feng, and Amy S. Fleischer. Engineering interfaces in carbon nanostructured mats for the creation of energy efficient thermal interface materials. *Carbon*, 61:441–457, September 2013.

[127] L. Berhan, Y. B. Yi, A. M. Sastry, E. Munoz, M. Selvidge, and R. Baughman. Mechanical properties of nanotube sheets: Alterations in joint morphology and achievable moduli in manufacturable materials. *Journal of Applied Physics*, 95(8):4335–4345, March 2004.

[128] Daniela Suppiger, Stephan Busato, and Paolo Ermanni. Characterization of single-walled carbon nanotube mats and their performance as electromechanical actuators. *Carbon*, 46(7):1085–1090, June 2008.

[129] Z. Wu. Transparent, Conductive Carbon Nanotube Films. *Science*, 305(5688):1273–1276, August 2004.

[130] G. Gruner. Carbon nanotube films for transparent and plastic electronics. *Journal of Materials Chemistry*, 16(35):3533, 2006.

[131] Mark P. Mattson, Robert C. Haddon, and Apparao M. Rao. Molecular functionalization of carbon nanotubes and use as substrates for neuronal growth. *Journal of Molecular Neuroscience*, 14(3):175–182, 2000.

[132] Hui Hu, Yingchun Ni, Vedrana Montana, Robert C. Haddon, and Vladimir Parpura. Chemically Functionalized Carbon Nanotubes as Substrates for Neuronal Growth. *Nano Letters*, 4(3):507–511, March 2004.

[133] Hui Hu, Yingchun Ni, Swadhin K. Mandal, Vedrana Montana, Bin Zhao, Robert C. Haddon, and Vladimir Parpura. Polyethyleneimine Functionalized Single-Walled Carbon Nanotubes as a Substrate for Neuronal Growth. *The Journal of Physical Chemistry B*, 109(10):4285–4289, March 2005.

[134] Yingchun Ni, Hui Hu, Erik B. Malarkey, Bin Zhao, Vedrana Montana, Robert C. Haddon, and Vladimir Parpura. Chemically Functionalized Water Soluble Single-Walled Carbon Nanotubes Modulate Neurite Outgrowth. *Journal of Nanoscience and Nanotechnology*, 5(10):1707–1712, October 2005.

[135] Jining Xie, Linfeng Chen, Kiran R Aatre, M Srivatsan, and V K Varadan. Somatosensory neurons grown on functionalized carbon nanotube mats. *Smart Materials and Structures*, 15(4):N85–N88, August 2006.

[136] Kotaro Matsumoto, Chie Sato, Yukie Naka, Ayako Kitazawa, Raymond L.D. Whitby, and Norio Shimizu. Neurite outgrowths of neurons with neurotrophin-coated carbon nanotubes. *Journal of Bioscience and Bioengineering*, 103(3):216–220, March 2007.

[137] Viviana Lovat, Davide Pantarotto, Laura Lagostena, Barbara Cacciari, Micaela Grandolfo, Massimo Righi, Giampiero Spalluto, Maurizio Prato, and Laura Ballerini. Carbon Nanotube Substrates Boost Neuronal Electrical Signaling. *Nano Letters*, 5(6):1107–1110, June 2005.

[138] Andrea Mazzatenta, Michele Giugliano, Stephane Campidelli, Luca Gambazzi, Luca Businaro, Henry Markram, Maurizio Prato, and Laura Ballerini. Interfacing Neurons with Carbon Nanotubes: Electrical Signal Transfer and Synaptic Stimulation in Cultured Brain Circuits. *The Journal of Neuroscience*, 27(26):6931–6936, June 2007.

[139] Giada Cellot, Emanuele Cilia, Sara Cipollone, Vladimir Rancic, Antonella Sucapane, Silvia Giordani, Luca Gambazzi, Henry Markram, Micaela Grandolfo, Denis Scaini, Fabrizio Gelain, Loredana Casalis, Maurizio Prato, Michele Giugliano, and Laura Ballerini. Carbon nanotubes might improve neuronal performance by favouring electrical shortcuts. *Nature Nanotechnology*, 4(2):126–133, February 2009.

[140] Erik B. Malarkey, Kirk A. Fisher, Elena Bekyarova, Wei Liu, Robert C. Haddon, and Vladimir Parpura. Conductive Single-Walled Carbon Nanotube Substrates Modulate Neuronal Growth. *Nano Letters*, 9(1):264–268, January 2009.

[141] Min Jee Jang, Seon Namgung, Seunghun Hong, and Yoonkey Nam. Directional neurite growth using carbon nanotube patterned substrates as a biomimetic cue. *Nanotechnology*, 21(23):235102, June 2010.

[142] Amlie Bduer, Florent Seichepine, Emmanuel Flahaut, Isabelle Loubinoux, Laurence Vaysse, and Christophe Vieu. Elucidation of the Role of Carbon Nanotube Patterns on the Development of Cultured Neuronal Cells. *Langmuir*, 28(50):17363–17371, December 2012.

[143] X Zhang, S Prasad, S Niyogi, A Morgan, M Ozkan, and C Ozkan. Guided neurite growth on patterned carbon nanotubes. *Sensors and Actuators B: Chemical*, 106(2):843–850, May 2005.

[144] Philip Lamoureux, Robert E. Buxbaum, and Steven R. Heidemann. Direct evidence that growth cones pull. *Nature*, 340(6229):159–162, July 1989.

[145] Jie Liu, Florence Appaix, Olivier Bibari, Gilles Marchand, Alim-Louis Benabid, Fabien Sauter-Starace, and Michel De Waard. Control of neuronal network organization by chemical surface functionalization of multi-walled carbon nanotube arrays. *Nanotechnology*, 22(19):195101, May 2011.

[146] M.M. Machado, A.O. Lobo, F.R. Marciano, E.J. Corat, and M.A.F. Corat. Analysis of cellular adhesion on superhydrophobic and superhydrophilic vertically aligned carbon nanotube scaffolds. *Materials Science and Engineering: C*, 48:365–371, March 2015.

[147] Raya Sorkin, Alon Greenbaum, Moshe David-Pur, Sarit Anava, Amir Ayali, Eshel Ben-Jacob, and Yael Hanein. Process entanglement as a neuronal anchorage mechanism to rough surfaces. *Nanotechnology*, 20(1):015101, January 2009.

[148] T. D. Barbara Nguyen-Vu, Hua Chen, Alan M. Cassell, Russell J. Andrews, M. Meyyappan, and Jun Li. Vertically Aligned Carbon Nanofiber Architecture as a Multifunctional 3-D Neural Electrical Interface. *IEEE Transactions on Biomedical Engineering*, 54(6):1121–1128, June 2007.

[149] Tamir Gabay, Eyal Jakobs, Eshel Ben-Jacob, and Yael Hanein. Engineered self-organization of neural networks using carbon nanotube clusters. *Physica A: Statistical Mechanics and its Applications*, 350(2-4):611–621, May 2005.

[150] R Sorkin, T Gabay, P Blinder, D Baranes, E Ben-Jacob, and Y Hanein. Compact self-wiring in cultured neural networks. *Journal of Neural Engineering*, 3(2):95–101, June 2006.

[151] Christoph Nick, Sandeep Yadav, Ravi Joshi, Christiane Thielemann, and Jrg J Schneider. Growth and structural discrimination of cortical neurons on randomly oriented and vertically aligned dense carbon nanotube networks. *Beilstein Journal of Nanotechnology*, 5:1575–1579, September 2014.

[152] Ke Wang, Harvey A. Fishman, Hongjie Dai, and James S. Harris. Neural Stimulation with a Carbon Nanotube Microelectrode Array. *Nano Letters*, 6(9):2043–2048, September 2006.

[153] Jiangang Du, Timothy J. Blanche, Reid R. Harrison, Henry A. Lester, and Sotiris C. Masmanidis. Multiplexed, High Density Electrophysiology with Nanofabricated Neural Probes. *PLOS ONE*, 6(10):e26204, October 2011.

[154] Gemma Gabriel, Rodrigo Gmez, Markus Bongard, Nuria Benito, Eduardo Fernndez, and Rosa Villa. Easily made single-walled carbon nanotube surface microelectrodes for neuronal applications. *Biosensors and Bioelectronics*, 24(7):1942–1948, March 2009.

[155] Chia-Min Lin, Yu-Tao Lee, Shih-Rung Yeh, and Weileun Fang. Flexible carbon nanotubes electrode for neural recording. *Biosensors and Bioelectronics*, 24(9):2791–2797, May 2009.

[156] Yung-Chan Chen, Hui-Lin Hsu, Yu-Tao Lee, Huan-Chieh Su, Shiang-Jie Yen, Chang-Hsiao Chen, Wei-Lun Hsu, Tri-Rung Yew, Shih-Rung Yeh, Da-Jeng Yao, Yen-Chung Chang, and Hsin Chen. An active, flexible carbon nanotube microelectrode array for recording electrocorticograms. *Journal of Neural Engineering*, 8(3):034001, June 2011.

[157] Wenwen Yi, Chaoyang Chen, Zhaoying Feng, Yong Xu, Chengpeng Zhou, Nirul Masurkar, John Cavanaugh, and Mark Ming-Cheng Cheng. A flexible and implantable microelectrode arrays using high-temperature grown vertical carbon nanotubes and a biocompatible polymer substrate. *Nanotechnology*, 26(12):125301, 2015.

[158] Chang-Hsiao Chen, Huan-Chieh Su, Shih-Chang Chuang, Shiang-Jie Yen, Yung-Chan Chen, Yu-Tao Lee, Hsin Chen, Tri-Rung Yew, Yen-Chung Chang, Shih-Rung Yeh, and Da-Jeng Yao. Hydrophilic modification of neural microelectrode arrays based on multi-walled carbon nanotubes. *Nanotechnology*, 21(48):485501, December 2010.

[159] Benoit Mandelbrot and Roberto Pignoni. *The fractal geometry of nature*, volume 173. WH freeman, New York, 1983.

[160] William Watterson, Saba Moslehi, Julian Smith, Rick Montgomery, and Richard Taylor. Fractal Electronics as a Generic Interface to Neurons. In *The Fractal Geometry of the Brain*, pages 553–565. Springer, 2016.

[161] Farzaneh Afshinmanesh, Alberto G. Curto, Kaveh M. Milaninia, Niek F. van Hulst, and Mark L. Brongersma. Transparent Metallic Fractal Electrodes for Semiconductor Devices. *Nano Letters*, 14(9):5068–5074, September 2014.

[162] Guanhai Li, Xiaoshuang Chen, Bo Ni, Oupeng Li, Lujun Huang, Yuan Jiang, Weida Hu, and Wei Lu. Fractal H-shaped plasmonic nanocavity. *Nanotechnology*, 24(20):205702, May 2013.

[163] Yong-Jun Bao, Hong-Min Li, Xiao-Chun Chen, Ru-Wen Peng, Mu Wang, Xiang Lu, Jun Shao, and Nai-Ben Ming. Tailoring the resonances of surface plasmas on fractal-featured metal film by adjusting aperture configuration. *Applied Physics Letters*, 92(15):151902, 2008.

[164] Samuel Gottheim, Hui Zhang, Alexander O. Govorov, and Naomi J. Halas. Fractal Nanoparticle Plasmonics: The Cayley Tree. *ACS Nano*, 9(3):3284–3292, March 2015.

[165] Jonathan A. Fan, Woon-Hong Yeo, Yewang Su, Yoshiaki Hattori, Woosik Lee, Sung-Young Jung, Yihui Zhang, Zhuangjian Liu, Huanyu Cheng, Leo Falgout, Mike Bajema, Todd Coleman, Dan Gregoire, Ryan J. Larsen, Yonggang Huang, and John A. Rogers. Fractal design concepts for stretchable electronics. *Nature Communications*, 5:ncomms4266, February 2014.

[166] D. B. Shire, S. K. Kelly, J. Chen, P. Doyle, M. D. Gingerich, S. F. Cogan, W. A. Drohan, O. Mendoza, L. Theogarajan, J. L. Wyatt, and J. F. Rizzo. Development and Implantation of a Minimally Invasive Wireless Subretinal Neurostimulator. *IEEE Transactions on Biomedical Engineering*, 56(10):2502–2511, October 2009.

[167] Lauren N. Ayton, Peter J. Blamey, Robyn H. Guymer, Chi D. Luu, David A. X. Nayagam, Nicholas C. Sinclair, Mohit N. Shivdasani, Jonathan Yeoh, Mark F. McCombe, Robert J. Briggs, Nicholas L. Opie, Joel Villalobos, Peter N. Dimitrov, Mary Varsamidis, Matthew A. Petoe, Chris D. McCarthy, Janine G. Walker, Nick Barnes, Anthony N. Burkitt, Chris E. Williams, Robert K. Shepherd, Penelope J. Allen, and for the Bionic Vision Australia Research Consortium. First-in-Human Trial of a Novel Suprachoroidal Retinal Prosthesis. *PLOS ONE*, 9(12):e115239, December 2014.

[168] Alfred Stett, Wolfgang Barth, Stefan Weiss, Hugo Haemmerle, and Eberhart Zrenner. Electrical multisite stimulation of the isolated chicken retina. *Vision Research*, 40(13):1785–1795, June 2000.

[169] T. G. Smith, G. D. Lange, and W. B. Marks. Fractal methods and results in cellular morphology dimensions, lacunarity and multifractals. *Journal of Neuroscience Methods*, 69(2):123–136, November 1996.

[170] F. Caserta, W. D. Eldred, E. Fernandez, R. E. Hausman, L. R. Stanford, S. V. Bulderev, S. Schwarzer, and H. E. Stanley. Determination of fractal dimension of physiologically characterized neurons in two and three dimensions. *Journal of Neuroscience Methods*, 56(2):133–144, February 1995.

[171] Tams Pajkossy. Electrochemistry at fractal surfaces. *Journal of Electroanalytical Chemistry and Interfacial Electrochemistry*, 300(1):1–11, February 1991.

[172] Chung-Wen Ho, A. Ruehli, and P. Brennan. The modified nodal approach to network analysis. *IEEE Transactions on Circuits and Systems*, 22(6):504–509, June 1975.

[173] J. W. Demmel. SuperLU Users' guide. *Lawrence Berkeley National Laboratory*, March 2011.

[174] Xiaoye S. Li and James W. Demmel. SuperLU DIST: A scalable distributed-memory sparse direct solver for unsymmetric linear systems. *ACM Transactions on Mathematical Software (TOMS)*, 29(2):110–140, 2003.

[175] W. Franks, I. Schenker, P. Schmutz, and A. Hierlemann. Impedance characterization and modeling of electrodes for biomedical applications. *IEEE Transactions on Biomedical Engineering*, 52(7):1295–1302, July 2005.

[176] M. Gerhardt, J. Alderman, and A. Stett. Electric Field Stimulation of Bipolar Cells in a Degenerated Retina #x2014;A Theoretical Study. *IEEE Transactions on Neural Systems and Rehabilitation Engineering*, 18(1):1–10, February 2010.

[177] Miganoosh Abramian, Nigel H. Lovell, John W. Morley, Gregg J. Suaning, and Socrates Dokos. Activation of retinal ganglion cells following epiretinal electrical stimulation with hexagonally arranged bipolar electrodes. *Journal of Neural Engineering*, 8(3):035004, 2011.

[178] Xiong-Li Yang and Samuel M. Wu. Response Sensitivity and Voltage Gain of the Rod- and Cone-Bipolar Cell Synapses in Dark-Adapted Tiger Salamander Retina. *Journal of Neurophysiology*, 78(5):2662–2673, November 1997.

[179] Leif Oltedal, Margaret Lin Veruki, and Espen Hartveit. Passive membrane properties and electrotonic signal processing in retinal rod bipolar cells. *The Journal of Physiology*, 587(4):829–849, February 2009.

[180] David Tsai, John W. Morley, Gregg J. Suaning, and Nigel H. Lovell. Direct Activation and Temporal Response Properties of Rabbit Retinal Ganglion Cells Following Subretinal Stimulation. *Journal of Neurophysiology*, 102(5):2982–2993, November 2009.

[181] R. de Levie. On porous electrodes in electrolyte solutions. *Electrochimica Acta*, 8(10):751–780, October 1963.

[182] Vadim F. Lvovich. *Impedance Spectroscopy: Applications to Electrochemical and Dielectric Phenomena*. John Wiley & Sons, July 2012. Google-Books-ID: CgGqMeQJArkC.

[183] R. G. H. Wilke, G. Khalili Moghadam, N. H. Lovell, G. J. Suaning, and S. Dokos. Electric crosstalk impairs spatial resolution of multi-electrode arrays in retinal implants. *Journal of Neural Engineering*, 8(4):046016, 2011.

[184] Thomas Flores, Georges Goetz, Xin Lei, and Daniel Palanker. Optimization of return electrodes in neurostimulating arrays. *Journal of Neural Engineering*, 13(3):036010, 2016.

[185] Sbastien Roux, Frdric Matonti, Florent Dupont, Louis Hoffart, Sylvain Takerkart, Serge Picaud, Pascale Pham, and Frdric Chavane. Probing the functional impact of sub-retinal prosthesis. *Elife*, 5:e12687, 2016.

[186] Tim Stout. Interview with Dr. Tim Stout. Baylor College of Medicine., August 2016.

[187] Luc Mallet, Valrie Mesnage, Jean-Luc Houeto, Antoine Pelissolo, Jrme Yelnik, Ccile Behar, Marcella Gargiulo, Marie-Laure Welter, Anne-Marie Bonnet, Bernard Pillon, Philippe Cornu, Didier Dormont, Bernard Pidoux, Jean-Franois Allilaire, and Yves Agid. Compulsions, Parkinson's disease, and stimulation. *The Lancet*, 360(9342):1302–1304, October 2002.

[188] Laleh Golestanirad, Behzad Elahi, Alberto Molina, Juan R. Mosig, Claudio Pollo, Robert Chen, and Simon J. Graham. Analysis of fractal electrodes for efficient neural stimulation. *Frontiers in Neuroengineering*, 6, 2013.

[189] N Congdon, O'Colmain B, Klaver Cc, Klein R, Muoz B, Friedman Ds, Kempen J, Taylor Hr, and Mitchell P. Causes and prevalence of visual impairment among adults in the United States. *Archives of ophthalmology (Chicago, Ill. : 1960)*, 122(4):477–485, April 2004.

[190] Joseph Matteo and L. Hesselink. Fractal extensions of near-field aperture shapes for enhanced transmission and resolution. *Optics Express*, 13(2):636–647, January 2005.

[191] Barbara Fazio, Pietro Artoni, Maria Antonia Iat, Cristiano D'Andrea, Maria Jos Lo Faro, Salvatore Del Sorbo, Stefano Pirotta, Pietro Giuseppe Gucciardi, Paolo Musumeci, Cirino Salvatore Vasi, Rosalba Saija, Matteo Galli, Francesco Priolo, and Alessia Irrera. Strongly enhanced light trapping in a two-dimensional silicon nanowire random fractal array. *Light: Science & Applications*, 5(4):e16062, January 2016.

[192] H. Samavati, A. Hajimiri, A. R. Shahani, G. N. Nasserbakht, and T. H. Lee. Fractal capacitors. *IEEE Journal of Solid-State Circuits*, 33(12):2035–2041, December 1998.

[193] Hugh O. Pierson. *Handbook of Refractory Carbides and Nitrides: Properties, Characteristics, Processing and Applications*. William Andrew, December 1996. Google-Books-ID: K_K7q3jaqXEC.

[194] Jenny Nelson. *The Physics of Solar Cells*. World Scientific Publishing Company, May 2003. Google-Books-ID: 4Ok7DQAAQBAJ.

[195] A. Sherman. Growth and Properties of LPCVD Titanium Nitride as a Diffusion Barrier for Silicon Device Technology. *Journal of The Electrochemical Society*, 137(6):1892–1897, June 1990.

[196] R. E. Bank and D. J. Rose. Global approximate Newton methods. *Numerische Mathematik*, 37(2):279–295, June 1981.

[197] H. Ceric. *Newton Methods: Numerical Methods in Modern TCAD*. PhD thesis, Vienna University of Technology, 2005.

[198] Franois C. Delori, Robert H. Webb, and David H. Sliney. Maximum permissible exposures for ocular safety (ANSI 2000), with emphasis on ophthalmic devices. *JOSA A*, 24(5):1250–1265, May 2007.

[199] Robert L. Myers. *Display Interfaces: Fundamentals and Standards*. John Wiley & Sons, July 2003. Google-Books-ID: LN3OJvIEmTQC.

[200] H. A. Bethe. Theory of Diffraction by Small Holes. *Physical Review*, 66(7-8):163–182, October 1944.

[201] Duke Piyathaisere, Eyal Margality, Shih-Jen Chen, Jeng-Shyong Shyu, Salvatore D'Anna, James Weiland, Rhonda Grebe, Lynnea Grebe, Gildo Fujii, Sahng Kim, Robert Greenberg, Eugene De Juan, and Mark Humayun. Heat effects on the retina. *Ophthalmic Surgery, Lasers and Imaging Retina*, 34(2):114–120, 2003.

[202] K. Gosalia, J. Weiland, M. Humayun, and G. Lazzi. Thermal Elevation in the Human Eye and Head Due to the Operation of a Retinal Prosthesis. *IEEE Transactions on Biomedical Engineering*, 51(8):1469–1477, August 2004.

[203] Nicholas L. Opie, Anthony N. Burkitt, Hamish Meffin, and David B. Grayden. Heating of the eye by a retinal prosthesis: modeling, cadaver and in vivo study. *IEEE transactions on bio-medical engineering*, 59(2):339–345, February 2012.

[204] G. Lazzi. Thermal effects of bioimplants. *IEEE Engineering in Medicine and Biology Magazine*, 24(5):75–81, September 2005.

[205] G Dagnelie. Retinal implants: emergence of a multidisciplinary field., Retinal Implants: Emergence of a multidisciplinary field. *Current opinion in neurology, Current Opinion in Neurology*, 25, 25(1, 1):67, 67–75, February 2012.

[206] Diego Ghezzi. Retinal prostheses: progress toward the next generation implants. *Frontiers in Neuroscience*, 9, August 2015.

[207] P. J. Rousche, D. S. Pellinen, D. P. Pivin, J. C. Williams, R. J. Vetter, and D. R. Kipke. Flexible polyimide-based intracortical electrode arrays with bioactive capability. *IEEE Transactions on Biomedical Engineering*, 48(3):361–371, March 2001.

[208] B. J. Kim, J. T. W. Kuo, S. A. Hara, C. D. Lee, L. Yu, C. A. Gutierrez, T. Q. Hoang, V. Pikov, and E. Meng. 3d Parylene sheath neural probe for chronic recordings. *Journal of Neural Engineering*, 10(4):045002, 2013.

[209] Y. W Fan, F. Z Cui, L. N Chen, Y Zhai, Q. Y Xu, and I-S Lee. Adhesion of neural cells on silicon wafer with nano-topographic surface. *Applied Surface Science*, 187(3):313–318, February 2002.

[210] Aldo Ferrari, Marco Cecchini, Akshay Dhawan, Silvestro Micera, Ilaria Tonazzini, Ripalta Stabile, Dario Pisignano, and Fabio Beltram. Nanotopographic Control of Neuronal Polarity. *Nano Letters*, 11(2):505–511, February 2011.

[211] Galle Piret, Maria-Thereza Perez, and Christelle N. Prinz. Neurite outgrowth and synaptophysin expression of postnatal CNS neurons on GaP nanowire arrays in long-term retinal cell culture. *Biomaterials*, 34(4):875–887, January 2013.

[212] Yossi Gross and Shai Vaingast. Retinal prosthesis, April 2012. U.S. Classification 607/54, 607/53; International Classification A61N1/36; Cooperative Classification H01L31/145, A61N1/3787, A61N1/37217, A61N1/36046, A61N1/0543, H01L27/14627, H01L27/14621; European Classification H01L27/146A10M, H01L27/146A8C, H01L31/14C, A61N1/36V, A61N1/378C, A61N1/372D2.

[213] Ying Liu, Yuliang Zhao, Baoyun Sun, and Chunying Chen. Understanding the Toxicity of Carbon Nanotubes. *Accounts of Chemical Research*, 46(3):702–713, March 2013.

[214] Asaf Shoval, Christopher Adams, Moshe David-Pur, MArk Shein, Yael Hanein, and Evelyne Sernagor. Carbon nanotube electrodes for effective interfacing with retinal tissue. *Frontiers in Neuroengineering*, 2, 2009.

[215] Cyril G. Eleftheriou, Jonas B. Zimmermann, Henrik D. Kjeldsen, Moshe David-Pur, Yael Hanein, and Evelyne Sernagor. Carbon nanotube electrodes for retinal implants: A study of structural and functional integration over time. *Biomaterials*, 112:108–121, January 2017.

[216] Anne-Claire Dupuis. The catalyst in the CCVD of carbon nanotubesa review. *Progress in Materials Science*, 50(8):929–961, November 2005.

[217] Chaohong Wu, Joost Schulte, Katharine J. Sepp, J. Troy Littleton, and Pengyu Hong. Automatic Robust Neurite Detection and Morphological Analysis of Neuronal Cell Cultures in High-content Screening. *Neuroinformatics*, 8(2):83–100, June 2010.

[218] Thomas R. Pisanic, Jennifer D. Blackwell, Veronica I. Shubayev, Rita R. Fiones, and Sungho Jin. Nanotoxicity of iron oxide nanoparticle internalization in growing neurons. *Biomaterials*, 28(16):2572–2581, June 2007.

[219] Di Wu, Elena S. Pak, Christopher J. Wingard, and Alexander K. Murashov. Multi-walled carbon nanotubes inhibit regenerative axon growth of dorsal root ganglia neurons of mice. *Neuroscience Letters*, 507(1):72–77, January 2012.

[220] C. Bittencourt, C. Navio, A. Nicolay, B. Ruelle, T. Godfroid, R. Snyders, J.-F. Colomer, M. J. Lagos, X. Ke, G. Van Tendeloo, I. Suarez-Martinez, and C. P. Ewels. Atomic Oxygen Functionalization of Vertically Aligned Carbon Nanotubes. *The Journal of Physical Chemistry C*, 115(42):20412–20418, October 2011.

[221] Bin Zhao, Lei Zhang, Xianying Wang, and Junhe Yang. Surface functionalization of vertically-aligned carbon nanotube forests by radio-frequency Ar/O2 plasma. *Carbon*, 50(8):2710–2716, July 2012.

[222] Micha E. Spira and Aviad Hai. Multi-electrode array technologies for neuroscience and cardiology. *Nature Nanotechnology*, 8(2):83–94, February 2013.

[223] M. Hutzler, A. Lambacher, B. Eversmann, M. Jenkner, R. Thewes, and P. Fromherz. High-Resolution Multitransistor Array Recording of Electrical Field Potentials in Cultured Brain Slices. *Journal of Neurophysiology*, 96(3):1638–1645, September 2006.

[224] Jacob T. Robinson, Marsela Jorgolli, and Hongkun Park. Nanowire electrodes for high-density stimulation and measurement of neural circuits. *Frontiers in Neural Circuits*, 7, March 2013.

[225] Gaute T Einevoll, Felix Franke, Espen Hagen, Christophe Pouzat, and Kenneth D Harris. Towards reliable spike-train recordings from thousands of neurons with multielectrodes. *Current Opinion in Neurobiology*, 22(1):11–17, February 2012.

[226] Gyrgy Buzski. Large-scale recording of neuronal ensembles. *Nature Neuroscience*, 7(5):446–451, May 2004.

[227] Rolf Weis, Bernt Mller, and Peter Fromherz. Neuron Adhesion on a Silicon Chip Probed by an Array of Field-Effect Transistors. *Physical Review Letters*, 76(2):327–330, January 1996.

[228] M. S. Fairbanks, D. N. McCarthy, S. A. Scott, S. A. Brown, and R. P. Taylor. Fractal electronic devices: simulation and implementation. *Nanotechnology*, 22(36):365304, 2011.

[229] Tzahi Cohen-Karni, Brian P. Timko, Lucien E. Weiss, and Charles M. Lieber. Flexible electrical recording from cells using nanowire transistor arrays. *Proceedings of the National Academy of Sciences*, 106(18):7309–7313, May 2009.

[230] Sami Rosenblatt, Yuval Yaish, Jiwoong Park, Jeff Gore, Vera Sazonova, and Paul L. McEuen. High Performance Electrolyte Gated Carbon Nanotube Transistors. *Nano Letters*, 2(8):869–872, August 2002.

[231] Robert J. Chen, Sarunya Bangsaruntip, Katerina A. Drouvalakis, Nadine Wong Shi Kam, Moonsub Shim, Yiming Li, Woong Kim, Paul J. Utz, and Hongjie Dai. Noncovalent functionalization of carbon nanotubes for highly specific electronic biosensors. *Proceedings of the National Academy of Sciences*, 100(9):4984–4989, April 2003.

[232] Xiaojie Duan, Ruixuan Gao, Ping Xie, Tzahi Cohen-Karni, Quan Qing, Hwan Sung Choe, Bozhi Tian, Xiaocheng Jiang, and Charles M. Lieber. Intracellular recordings of action potentials by an extracellular nanoscale field-effect transistor. *Nature Nanotechnology*, 7(3):174–179, March 2012.

[233] Woodrow L. Shew, Timothy Bellay, and Dietmar Plenz. Simultaneous multi-electrode array recording and two-photon calcium imaging of neural activity. *Journal of Neuroscience Methods*, 192(1):75–82, September 2010.

[234] Tsai-Wen Chen, Trevor J. Wardill, Yi Sun, Stefan R. Pulver, Sabine L. Renninger, Amy Baohan, Eric R. Schreiter, Rex A. Kerr, Michael B. Orger, Vivek Jayaraman, Loren L. Looger, Karel Svoboda, and Douglas S. Kim. Ultra-sensitive fluorescent proteins for imaging neuronal activity. *Nature*, 499(7458):295–300, July 2013.